

**SYNTHESIS AND CHARACTERIZATION OF LEAD-FREE  
PEROVSKITE FILMS FOR PHOTOVOLTAIC APPLICATIONS**

**A THESIS SUBMITTED IN PARTIAL FULFILLMENT OF THE  
REQUIREMENTS FOR THE DEGREE OF DOCTOR OF  
PHILOSOPHY**

**KAMAL BHUJEL**

**MZU REGN NO. 1807390**

**PH.D REGN NO. MZU/PH.D./1246 OF 10.08.2018**



**DEPARTMENT OF PHYSICS**

**SCHOOL OF PHYSICAL SCIENCES**

**NOVEMBER, 2022**

**SYNTHESIS AND CHARACTERIZATION OF LEAD-FREE  
PEROVSKITE FILMS FOR PHOTOVOLTAIC APPLICATIONS**

**By**

**Kamal Bhujel**

**Department of Physics**

**Supervisor**

**Prof. Suman Rai**

**Joint Supervisor**

**Dr. N. Surajkumar Singh**

**Submitted**

**In partial fulfillment of the requirement of the Degree of Doctor of  
Philosophy in Physics of Mizoram University, Aizawl.**



**Mizoram University (A Central University)**

**Tanhriil-796 004, Aizawl, Mizoram**

**Department of Physics**

**Prof. Suman Rai**

Professor.

Ph: +91-8732853277

Post Box No. 190

Gram: MZU

Phone: 0389-2330435, 230522

Email: srai.raii677@gmail.com

---

No.

Dt.02/11/2022

## *Certificate*

*This is to certify that the thesis entitled ‘**Synthesis and characterization of lead-free perovskite films for photovoltaic applications**’ submitted by Kamal Bhujel for the degree of Doctor of Philosophy under the Mizoram University, Aizawl, embodies the record of original investigations carried out by him under my supervision. He has been duly registered and the thesis presented is worthy of being considered for the award of the Ph.D. degree. This work has not been submitted for any degree from any other university.*

**(Dr. N. Surajkumar Singh)**

**Joint Supervisor**

**(Prof. Suman Rai)**

**Supervisor**

**Declaration**  
**Mizoram University**  
**November 2022**

I Kamal Bhujel, hereby declare that the subject matter of this thesis is the record of work done by me, that the contents of this thesis did not form basis of the award of any previous degree to me or to do the best of my knowledge to anybody else, and that the thesis has not been submitted by me for any research degree in any other University/Institute.

This is being submitted to the Mizoram University for the degree of Doctor of Philosophy in Physics.

Dated: 02/11/2022

(KAMAL BHUJEL)

Candidate

(Prof. ZAITHANZAUVA PACHUAU)

Head

(Prof. SUMAN RAI)

Supervisor

(Dr. N. SURAJKUMAR SINGH)

Joint Supervisor

### **Acknowledgements**

*I would like to express my most sincere gratitude to my supervisor Prof. Suman Rai for his guidance, support and commitment throughout the duration of my research. Thanks, are also due to Dr N. Surajkumar Singh, my joint supervisor and PI for his guidance and encouragement. I would also like to thank Prof. D. Tiwari, Dean of the School of Physical Sciences and Prof. Z. Pachuau, Head of the Dept. of Physics, for allowing me to work as a registered scholar. I am thankful to the other faculty members, research scholars and the non-teaching staff of the Dept. of Physics at PUC and MZU both for their valuable suggestions and directions regarding my research work and for always being helpful. Special thanks to Dr. Divya Prakash Rai, Dr. Hriatzuala of PUC and Dr. Amit Shankar of Kurseong College for their continuous encouragement.*

*I am also thankful to DST-SERB for providing financial support through the project titled “Synthesis and characterisation of lead-free perovskite films for photovoltaic applications” (EEQ/2017/000435 dated 17 March 2018).*

*I am indebted to Prof. R. Thangavel, of IIT-Dhanbad, under whom I could complete my work and to the Director, Prof. R. Shekhar of IIT-Dhanbad for his kind support in my research work. I am very thankful to my high school Physics teacher, Mr. Eric Yonzon, who built a strong base of physics and Prof. Ramswarup Ganguly, the Principal and other Faculty members of the Physics Dept. of Vidyasagar Metropolitan (evening) College, Kolkata. I am also thankful to Prof. S. Mahapatra of IIT-Bombay, Prof. Arshad Hussain of Tripura University, Prof. Mrinmoy Mukhopadhyay of SINP-Kolkata and Prof. L. R. Singh of NEHU for allowing me to do experimental work and providing characterization facilities at their laboratories.*

*It was not possible to complete this work without the support of all the people who came across my course of studies from the primary to the research level. I am thankful to all those who helped me directly or indirectly in my academics.*

**(KAMAL BHUJEL)**

# CONTENTS

Certificate	i
Declaration	ii
Acknowledgements	iii
Contents	iv-vi
List of Figures	viii-ix
CHAPTER 1: Introduction	1-2
1.1 Perovskite	2-3
1.2 Perovskite Solar Cells (PSCs)	4-6
1.3 Perovskite Solar Cell Architecture	7-8
CHAPTER 2. Instrumentation and Characterization Techniques	9
2.1. Grazing Incident X-ray Diffraction (GIXRD)	9-13
2.2. UV-visible Spectrophotometer	13-14
2.3. Scanning Electron Microscope (SEM) with Energy Dispersive X-ray Spectroscopy.	14-18
2.4. Photoluminescence (PL) Spectroscopy	18-19
2.5. X-ray Photoelectron Spectroscopy (XPS)	20-21
2.6. Hall Measurement	21-23
CHAPTER 3. Synthesis and characterization of ZnO nanoparticles (np), ZnO thin film and ZnO nanorods (nr) as Electron Transport Layer (ETL)	24

3. Experimental	
3.1. Materials	25
3.2. Methods adopted for ZnO nr and ZnO np	25-26
3.3. Results and discussions	
3.3.1. Structural Properties (GIXRD)	27-28
3.3.2. Optical Properties	28-31
3.3.3. Morphological Properties (FESEM)	32-33
3.3.4. Electrical Properties	33
	34
3.4. Conclusion	
 CHAPTER 4. Synthesis and characterization of NiO and Cu:NiO thin films as Hole Transport Layer (HTL) for PSCs.	 35-37
4. Experimental	
4.1. Materials	37
4.2. Methodology (Solution preparation, thin film coating)	37
4.3. Results and discussions	
4.3.1. Structural Properties (GIXRD)	38-40
4.3.2. Morphological Properties (FESEM with EDX)	40-42
4.3.3. Optical Properties	42-46
4.3.4. Electrical Properties	46-47
4.3.5. XPS measurement	48-49
4.4. Conclusion	50

CHAPTER 5. Synthesis and characterization of Lead-free double Perovskites	
for complete device fabrication of PSCs.	51-52
5. Experimental	52
5.1. Materials	52
5.2. Methodology	52
5.3. Results and discussions	52
5.3.1. Structural Properties (GIXRD)	53-54
5.3.2. Optical Properties (Absorbance, PL)	54-55
5.3.3. Morphological Properties (FESEM with EDX)	55-56
5.4. Device fabrication	57-59
5.5. Electrical Properties and PCE Calculation	60-61
5.6. Conclusion	61
CHAPTER 6. Summary and conclusion	62-65
References	66-78
List of the Publications	79
Bio-Data	80
Particulars	81



## LIST OF FIGURES

<b>Fig. No.</b>	<b>Description</b>	<b>Page No.</b>
Fig. 1.1.	Schematic diagram of the general structure of a Perovskite solar cell a) p-i-n and b) n-i-p configuration	8
Fig. 2.1.	Diffraction of radiation by crystal planes	10
Fig. 2.2.	Schematic diagram of GIXRD setup for out-of-plane and in-plane measurements	11
Fig. 2.3.	Schematic diagram for the UV- Visible double beam spectrophotometer	14
Fig. 2.4.	Interaction of different electrons with the sample	15
Fig. 2.5.	Schematic diagram showing different components of SEM equipment	15
Fig. 2.6.	Diagram showing the generation of characteristic X-ray and their nomenclature	16
Fig. 2.7.	Different types of signals emitted by incident beam-specimen interaction	17
Fig. 2.8.	Schematic diagram for EDX System	18
Fig. 2.9.	Representation of components and working of PL spectrometer	19
Fig. 2.10.	X-ray Photoelectron Spectrometer used for this research work	21
Fig. 2.11.	Different types of contacts for samples in the Hall measurement	22
Fig. 2.12.	Four probe clips for holding the samples	23
Fig. 3.1.	Flowchart for preparing ZnO thin film and the ZnO nanorods	26
Fig. 3.2.	XRD graphs of ZnO np and ZnO nr	27
Fig. 3.3.	Absorbance of ZnO np and ZnO nr	28
Fig. 3.4.	Transmittance of ZnO np and ZnO nr	29
Fig. 3.5.	Band gap of ZnO np	30

Fig. 3.6.	Band gap of ZnO nr	30
Fig. 3.7.	PL graph of ZnO nr and ZnO np	31
Fig. 3.8.	a) FESEM image of ZnO np, b) FESEM image of ZnO nr c) Cross- section image of ZnO nr and d) Near view of ZnO nr	32
Fig. 3.9.	a) EDX of ZnO np and b) EDX of ZnO nr	33
Fig. 3.10.	J-V graph of ZnO nr and ZnO np	33
Fig. 4.1.	Different stages of NiO thin film preparation	38
Fig. 4.2.	XRD graph of NiO and Cu doped NiO thin film	39
Fig. 4.3.	FESEM and Cross section images of the a) & e) NiO, b) & f) 2Cu:NiO, c) & g) 4Cu:NiO and d) & h) 6Cu:NiO respectively	41
Fig. 4.4.	EDX of a) NiO, b) 2Cu:NiO, c) 4Cu:NiO and d) 6Cu:NiO	42
Fig. 4.5.	Absorbance of NiO and Cu doped NiO	42
Fig. 4.6.	Transmittance of NiO and Cu doped NiO	43
Fig. 4.7.	Band gap of NiO and Cu doped NiO from Tauc's plot	44
Fig. 4.8.	PL graph of NiO and Cu doped NiO thin films	46
Fig. 4.9.	J-V characteristics of a) NiO, b) 2Cu:NiO, c) 4Cu:NiO and d) 6Cu:NiO under the dark, light, UV and IR illumination	47
Fig. 4.10.	O 1s states of a) Undoped and b) Cu:NiO, Ni 2p Spectra of c) Undoped NiO and d) Cu doped NiO Ni 2p <sub>3/2</sub> XPS spectra e) Undoped NiO and f) Cu doped NiO	49
Fig. 5.1.	Cs <sub>2</sub> AgBiBr <sub>6</sub> Solution	53
Fig. 5.2.	XRD graph of Cs <sub>2</sub> AgBiBr <sub>6</sub>	54
Fig. 5.3.	Absorbance of Cs <sub>2</sub> AgBiBr <sub>6</sub>	54
Fig. 5.4.	Tauc's Plot showing the band gap of Cs <sub>2</sub> AgBiBr <sub>6</sub>	55
Fig. 5.5.	FESEM image of Cs <sub>2</sub> AgBiBr <sub>6</sub>	56
Fig. 5.6.	EDX graph of Cs <sub>2</sub> AgBiBr <sub>6</sub>	56
Fig. 5.7.	Synthesis of Perovskite layer	57

Fig. 5.8.	PSC p-i-n device architecture a) NiO/Cs <sub>2</sub> AgBiBr <sub>6</sub> /ZnO, b) 2Cu:NiO/Cs <sub>2</sub> AgBiBr <sub>6</sub> /ZnO, c) 4Cu:NiO/Cs <sub>2</sub> AgBiBr <sub>6</sub> /ZnO and d) 6Cu:NiO/Cs <sub>2</sub> AgBiBr <sub>6</sub> /ZnO	58
Fig. 5.9.	Patterned FTO glass	58
Fig. 5.10	Solar Simulator	59
Fig. 5.11.	Prepared PSCs	59
Fig. 5.12.	J-V characteristics of PSCs	60

## CHAPTER 1

### INTRODUCTION

Energy has a very vital role in the development of human civilization. The irrational use and unethical exploitation have led to the scarcity of energy resources. The demand for energy is everlasting but the resources are limited. The economy of the country also depends upon the availability of the energy supply. Thus, each country is looking for the development of a permanent solution to the energy crisis. Solar energy is one of the greatest sources of renewable energy for meeting the world's energy demand because of its enormous magnitude – approximately  $10^5$  terawatts. The current energy consumption of the world is about 12 terawatts; this represents only 0.01% of the total amount of the Sun's energy that reaches the Earth's surface (Nuraje *et al.*, 2012). Over the years, silicon-based cells have been used due to their efficient solar-to-power generation (~30%), particularly crystalline silicon (Green *et al.*, 2014). An alternative to silicon solar cells, perovskites (organic-inorganic) have reached the top position (~20.1%) within ~5 years, due to substantial improvement in power conversion efficiency and low processing costs (Chung *et al.*, 2012a; Grätzel, 2014; Hodes & Cahen, 2014; Y. Huang *et al.*, 2014; H. S. Kim *et al.*, 2014; Snaith, 2013).

There are many sources of energy available in the world. Among all, solar energy, a promising renewable energy source, is attracting all researchers globally. In 1839 the French Scientist Edmond Becquerel discovered the solar photovoltaic effect, which opened a new field (Fatet, 2005). W. G. Adams and R. E. Day found photovoltaic effects on solidified selenium in 1877 and reported the selenium cells. The first solar photovoltaics cell design based on selenium was reported by Charles Fritts in 1883 with 1% efficiency. James Moser reported the dye-sensitized photochemical cells in 1887. In 1888, Edward Weston, in 1894 Melvin Severy, and Harry Reagan in 1897 received patents for solar cells respectively. In 1905, Albert Einstein explained the photoelectric effect and in 1932, the photovoltaic effect on Cadmium solar cell (CdSe) was discovered by Audobert and Stora. Eventually, on April 25, 1954, David Chapin, Calvin Fuller, and Gerald Pearson of Bell Labs in the United States were credited with the world's first photovoltaic solar cell (Bellis, 2019). In 1955, Hoffman Electrics commercialized the solar cell with 10% efficiency. Zhore

Alferov developed the first ever highly effective Gallium Arsenide (GaAs) heterostructure solar cell in 1970. The first thin film solar cell was developed by the University of Delaware with more than 10% efficiency using Cu<sub>2</sub>S/CdS in 1980. In 1985 a Solar cell with more than 20% efficiency was developed by the University of New South Wales. In 1988 Michael Gratzel and Brian O'Regan created Dye-Sensitized Solar Cell (DSSC). National Renewable Energy Laboratory (NREL) was established in the year 1994 and came up with the GaInP/GaAs two terminal concentrator cell with more than 30% efficiency. Consequently, NREL developed a multijunction concentrator solar cell with 47% efficiency. The first perovskite-based DSSC was reported by Kojima *et al* (Kojima *et al.*, 2009). Kim *et al* reported the first perovskite solid-state solar cell (H. S. Kim *et al.*, 2012). Till now the efficiency of perovskite solar cells has reached more than 25% (NREL). Similarly, in comparison to the Si-solar cells, organo-lead-halide perovskite-based solar cells have achieved the highest efficiency. Most of the time Pb is substituted with Sn and observed comparable efficiency. The instability of tin oxides in a normal environment however hinders the preparation of perovskite solar cells (PSCs). The toxicity of Pb in Pb-based perovskite created serious issues in the commercialization of solar cell devices. So, more intense research was started for Pb-free perovskite materials (Bai *et al.*, 2018). Double and inorganic perovskites are also in the possible tracks. Pb-free perovskite with high-efficiency materials is a promising candidate for future energy resources.

### 1.1. Perovskite

The terms "perovskite" and "perovskite structure" are often interchangeable in use. Perovskite was first found in the Ural Mountains which was a type of mineral in technical terms. It was named after Lev Perovski (who was the founder of the Russian Geographical Society). If any compound resembles the structure of the perovskite mineral they are known as perovskite.

CaTiO<sub>3</sub> constituting the calcium, titanium and oxygen in the compound form is considered the True perovskite (the mineral). So, to represent the perovskite in general structure, the generic form ABX<sub>3</sub> is designated as a crystallographic structure for perovskite (the mineral). In ABX<sub>3</sub>, A is a 2+ metal cation, B is a 4+ metal cation, and X is a 2- oxygen anion or halogen (Hou *et al.*, 2016; S. Wang *et al.*, 2021). Other

examples are BaTiO<sub>3</sub>, CsSnI<sub>3</sub>, Cs<sub>2</sub>AgBiBr<sub>6</sub> (Double perovskite) etc. The perovskite lattice arrangement is just like many other structures in crystallography and there are various ways to represent it. A perovskite if explained in the simplest way is a large atomic or molecular cation (positively charged) of type A in the centre of a cube with atom B occupying the corners of the cube (also positively-charged cations) and the smaller atom X occupying the faces of the cube with a negative charge (anion).

Depending on the arrangement of atoms/molecules formed in the structure, an impressive array of interesting properties in perovskites can be observed, including spin-dependent transport (spintronics), superconductivity, giant magnetoresistance and catalytic properties. Therefore, Perovskites opens an exciting field for chemists, physicists and material scientists.

Perovskites were first successfully used in solid-state solar cells in 2012, and since then most cells have used various combinations of materials in the usual perovskite form ABX<sub>3</sub> (H. S. Kim *et al.*, 2012).

In the last decade, Perovskite materials have emerged as a new class of optoelectronic semiconductors which brought a drastic change in photovoltaic research. Perovskite materials present numerous advantages including unique electronic structure, bandgap tunability, superior charge transport properties, facile processing, and low cost (Y. T. Huang *et al.*, 2021; Ma *et al.*, 2018). Perovskite solar cells have demonstrated unprecedented progress in efficiency and their architecture evolved over the period of the last 9-10 years, achieving a high-power conversion efficiency of more than 25% in 2021 (J. Liu *et al.*, 2021), serving as a promising candidate with the potential to replace the existing commercial PV technologies. However, the toxicity of Pb-based materials in solar cells restricts their utilization and commercialization. To get rid of this issue, rigorous research on lead-free materials with high-efficiency output is the need of the hour. Fortunately, Pb is replaced by its alternative materials and Pb-free perovskite mainly double perovskites solar cells have been developed and reached an efficiency of approximately ~15% (Smith, n.d.). Although the efficiency of Pb-free perovskite devices is inferior to Pb-based ones, the reports pave the way for the bright hope for the commercialization of PSCs and provide better stability and eco-friendly paths.

## 1.2. Perovskite Solar Cells (PSCs)

Perovskite solar cells (PSCs), were first reported by Kojima *et al.* in 2009, who employed  $\text{CH}_3\text{NH}_3\text{PbI}_3$  ( $\text{MAPbI}_3$ ) and  $\text{CH}_3\text{NH}_3\text{PbBr}_3$  ( $\text{MAPbBr}_3$ ) as sensitizers in dye-sensitized solar cells based on liquid-electrolyte and achieved an efficiency of 3.81%. By less than 10 years of development, the efficiency has been raised to 25% according to the latest chart of record cell efficiencies from the National Renewable Energy Laboratory (Chung *et al.*, 2012b; Saliba *et al.*, 2016; W. S. Yang *et al.*, 2015a; Y. Zhou *et al.*, 2016). To push the rising star from academic studies into real-life applications, massive efforts have been made to the improvement of performance and stability of PSCs (Niu *et al.*, 2016).

However, the main hindrance to the commercialization of PSCs is (1) toxicity of Pb atoms, (2) degrading in a very short time and (3) high cost. The lead-based perovskites are the champion in producing the highest efficiency today. However, the application of Pb-based materials in PSCs is not desired. In order to eliminate this issue, the common trend of research is concentrated on lead-free materials along with commercialization. Fortunately, Sn-based materials have been developed and reached an efficiency of approximately ~7% (Hao *et al.*, 2014; Noel *et al.*, 2014). Although the efficiency of Sn-based lead-free perovskite devices has not exceeded the efficiency of the Pb-based devices, there is hope to overcome this in a very short period of time.

Subbiah *et al.*, reported power conversion efficiency (PCE) of 7.3% using an inorganic NiO as a hole conductor in planar, inverse  $\text{CH}_3\text{NH}_3\text{PbI}_{3-x}\text{Cl}_x$ -based cells instead of organic hole conductors which were usually coupled with hybrid organic-inorganic semiconducting perovskite photovoltaic cells (Subbiah *et al.*, 2014). Chatterjee and Pal (2016), introduced  $\text{Cu}_2\text{O}$  thin films as a hole-transport layer in planar perovskite solar cells (Chatterjee & Pal, 2016). With methylammonium lead triiodide ( $\text{MAPbI}_3$ ) they formed a direct structure (p-i-n), where the perovskite layer was sandwiched between a layer of p-type  $\text{Cu}_2\text{O}$  and another layer of n-type phenyl-C61-butyric acid methyl ester (PCBM), which acted as a hole- and electron-transport materials, respectively, yielding an energy conversion efficiency ( $\eta$ ) of 8.23% under 1 sun illumination. Kumar *et al.*, (2016) examined the structural stability, electronic structure, and optical properties of  $\text{CH}_3\text{NH}_3\text{BaI}_3$  hybrid perovskite and reported that

the solution-processed thin films of  $\text{CH}_3\text{NH}_3\text{BaI}_3$  exhibited high transparency in the wavelength range of 400–825 nm (1.5–3.1 eV for which the photon current density is highest in the solar spectrum) (Kumar *et al.*, 2016). Gollu *et al.*, (2015), reported a 13% increase in the PCE when  $\text{SiO}_2$  np were incorporated in P3HT:PCBM photoactive layer, whereas PCE was increased by 20% when  $\text{SiO}_2$  np were incorporated in ZnO-based ETL

The rise of the organic-inorganic hybrid halide perovskite (hybrid perovskite) has stunned the photovoltaic community with its remarkable performance and rapid progress in the past 5 years (Q. Chen *et al.*, 2015). This extraordinary material has exhibited unprecedented development, soaring to cross 20% PCE in photovoltaic (PV) devices within very few years (Burschka *et al.*, 2013; Jeon *et al.*, 2015; H. Zhou *et al.*, 2014).

Debut in photovoltaics by hybrid perovskite was made in 2006 when Miyasaka and colleagues by employing  $\text{CH}_3\text{NH}_3\text{PbBr}_3$  as a sensitizer on nanoporous  $\text{TiO}_2$  in a dye-sensitized solar cell (DSSC) based on liquid electrolyte, had obtained the efficiency of 2.2%. In 2009, a PCE of 3.8% was achieved by replacing Br with I (Kojima *et al.*, 2009). In 2011, Park and co-workers achieved an efficiency of 6.5% by employing perovskite nanoparticles (~2.5 nm in diameter) on  $\text{TiO}_2$  to serve as sensitizers for improved absorption over conventional dyes (Im *et al.*, 2011). Those devices were very susceptible to dissolution within the solutions of polar electrolytes. Consequentially, in 2012 Kim *et al.*, applied a solid electrolyte Spiro-MeOTAD (2,2',7,7'-tetrakis (N,N-pdimethoxyphenylamino)-9,9'spirobifluorene) as a hole transport layer (HTL), and reported an initial efficiency of 9.7% along with an improvement in its stability compared to the liquid-based design (H. S. Kim *et al.*, 2012). In the same year, an HTL-free device was also demonstrated with a PCE of 7.3% (Etgar *et al.*, 2012).

Later, Snaith reported the replacement of the n-type  $\text{TiO}_2$  electron transport material (ETM) with an inert  $\text{Al}_2\text{O}_3$  scaffold, demonstrating an efficiency of 10.9% (Snaith, 2013). In 2013, Grätzel's group used the two-step iodide and scaffold  $\text{TiO}_2$  for improving the morphology of perovskite. They got an exceeding 15% efficiency by a two-step solution processing (Grätzel, 2014). These reports revealed the



ambipolar nature of perovskites, which enlightened and encouraged the intensive employment of the planar hetero-junction architecture in these devices (Grätzel, 2014; M. Liu *et al.*, 2013). Meanwhile, Snaith and co-workers reported a mixed-halide perovskite by using chlorine-containing precursors, demonstrating improved carrier transport, diffusion lengths and stability over its tri-iodide counterpart (Snaith, 2013). Later, bromine inclusion was reported to feature an adjustable band gap for perovskites (Noh *et al.*, 2013). This sparked an enormous development in the hybrid lead halide perovskite  $\text{CH}_3\text{NH}_3\text{PbX}_3$  ( $\text{X} = \text{I}, \text{Cl}, \text{Br}$ ), obtaining a record PCE reaching up to 20.1% in just five years using low-cost production methods and 28.2% efficient Perovskite silicon-based tandem solar cell (J. Liu *et al.*, 2021). Docampo *et al.*, 2013, also reported the possible fabrication of a perovskite solar cell, an 'inverted' configuration with the hole transporter below and the electron collector above the perovskite planar film (Docampo *et al.*, 2013). W. S. Yang *et al.*, 2015, at UCLA, reported reverse-scan efficiency of 19.3% with the planar thin film of perovskite using a range of deposition (W. S. Yang *et al.*, 2015b). At the 6th World Conference (2014), on Photovoltaic Energy Conversion in Kyoto, Japan, a single-junction PSC was mentioned with a PCE of 24%.

Later Pb-free inorganic Double Perovskites (DPs) were employed in the PSCs. The DPs were easier to synthesize, and their stability was good in an ambient environment and durable for long periods (H. J. Feng *et al.*, 2017a; Lamba *et al.*, 2019; Y. Liu *et al.*, 2021). In our work also we have tried to prepare  $\text{Cs}_2\text{AgBiBr}_6$  of DPs for photovoltaic applications (H. J. Feng *et al.*, 2017b; Filip *et al.*, 2016a; McClure *et al.*, 2016; X. Yang *et al.*, 2020). Wang *et al.*, reported DP  $\text{Cs}_2\text{AgBiBr}_6$  with the highest PCE of 3.11% till now. They used Carboxy-Chlorophyll derivative (C-Chl)-sensitized  $\text{TiO}_2$  film as ETL (B. Wang *et al.*, 2021). Previously, they had reported the Zinc Chlorophyll (Zn-Chl) derivative-based HTL (Hole transport layer) in a  $\text{Cs}_2\text{AgBiBr}_6$  device with a PCE of 2.79% (M. Wang *et al.*, 2018). Ning *et al.*, (2018) developed the  $\text{TiO}_2$ -based  $\text{Cs}_2\text{AgBiBr}_6$  PSC with the highest PCE of 1.1% (Ning *et al.*, 2018). Igbari *et al.*, (2019) prepared the  $\text{Cs}_2\text{AgBiBr}_6$  PSC following the vacuum-assisted sublimation method and achieved a PCE of 2.48% on average (Igbari *et al.*, 2019).

### 1.3. Perovskite Solar Cell Architecture

The efficiency of Perovskite Solar Cells depends upon various parameters such as the material used for electron and hole transportations and the thickness of the layers, depositing methods, band gap tailoring, the condition of the lab environment and many more.

In general, the thin film-based PSCs' architecture has a structure of multilayer components as electrodes, ETL (electron transport layer), perovskite absorber, HTL (hole transport layer), and back contact (Arumugam *et al.*, 2021). Between the HTL and ETL, the perovskite absorbers are mainly sandwiched in the middle. Changing the materials used in the ETL and HTL has shown an improvement in the efficiency of the PSCs (Nair *et al.*, 2020). ETLs are the n-type semiconductors viz. PCBM, ZnO, SnO<sub>2</sub>, TiO<sub>2</sub>, etc., and HTLs are p-type semiconductors, namely, Spiro-OMeTAD, PEDOT:PSS {poly(3,4-ethylenedioxythiophene)/poly(styrene sulfonic acid)}, NiO<sub>x</sub>, CuSCN, etc (L.-C. Chen & Tseng, 2017; M. Feng *et al.*, 2020a; Tavakoli *et al.*, 2016). Previously, the organic HTL PEDOT:PSS was widespread in PSCs, but due to its hygroscopic and poor electron-blocking nature, a lot of degradation in PCE occurred (Akhtaruzzaman *et al.*, 2020; M.-H. Liu *et al.*, 2016). If the electrons are not blocked properly, then the recombination at the interface layer will be increased leading to low cell efficiency (Yin *et al.*, 2019). PEDOT:PSS has acidic nature as well. Transport materials need to be transparent, able to block the electron, and should possess ohmic contact with the electrodes and good stability (Yin *et al.*, 2016; Yoon & Kang, 2018). NiO thin film has been used as the HTL in this present work. It is found that inorganic materials provide good stability and carrier mobility (Guo *et al.*, 2018). ZnO np have been employed as an ETL in perovskite solar cells due to their influence on morphology, surface property, and thickness in overall power conversion efficiency. The properties of ZnO include high transparency, wide band gap semi-conductivity and sensing properties (L.-C. Chen & Tseng, 2017).

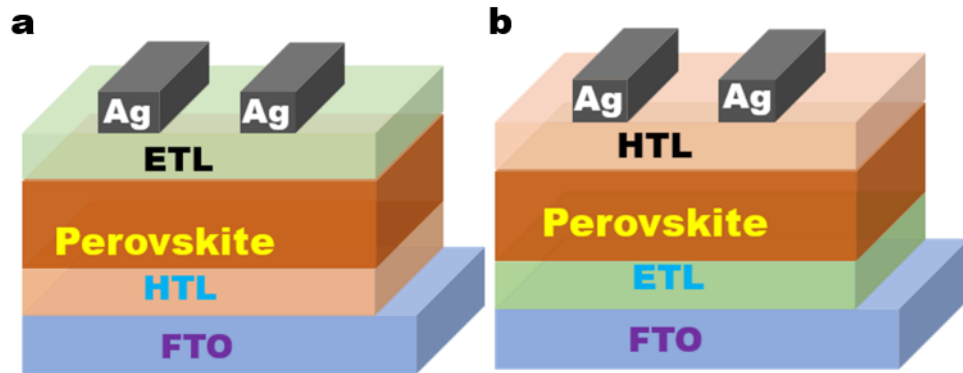


**Fig. 1.1. Schematic diagram of the general structure of a Perovskite solar cell a) p-i-n and b) n-i-p configuration**

At present, the main focus of researchers around the world is on the improvement of long-term stable PSCs for commercialization in the PV market. The toxicity is also another problem of Pb for the adoption of such PV products to consumers or the development of integrated applications. However, the diversity of PSCs such as flexibility and multi-junctions provides new hope for market introduction.

So, this research work proposes to develop Pb-free perovskite materials and characterize the same for utilization in perovskite solar cells. The work has tried to find a way to provide better eco-friendly paths.

## **CHAPTER 2**

### **INSTRUMENTATION AND CHARACTERIZATION TECHNIQUES**

#### **INTRODUCTION**

In experimental research, characterization techniques are very important for the confirmation of the correct results. The progress of the research also depends upon the improvements in the quality of the instruments used. Much and more characterizations provide the results from the different dimensions. In this chapter, we will discuss the use of instruments and the principle of characterization techniques applied to the prepared samples. Grazing Incident X-ray Diffractometer (GIXRD), Scanning Electron Microscope (SEM) with Energy Dispersive X-ray Spectroscopy (EDX), X-ray Photoelectron Spectroscopy (XPS), Ultraviolet-Visible Spectrophotometer (UV-Vis), Photoluminescence Spectrometer (PL), Current Voltage Source meter (IV), Hall Measurement and Solar simulator are the instruments which have been used for this work.

The Perovskite Solar Cell has mainly three components, ETL, HTL and the absorber layer. For confirming and understanding their polycrystalline structure we used GIXRD. It also provides data about the particle size and crystal phase. The working principle and the methods of characterization of the samples are discussed in short. The surface morphology is studied with the help of SEM. It also provides information about the shape and size of the crystal. The EDX attached to the SEM is used to confirm the elemental composition of the prepared samples. Absorption and Transmittance are studied by UV-Vis Spectrometer which is also used to calculate the optical band gap of the materials. The emissive property of the samples was studied with PL spectroscopy. The Current Voltage measurement was done by the Keithley source meter.

#### **2.1. Grazing Incident X-ray Diffraction (GIXRD)**

Grazing incidence X-ray diffraction (GIXRD) is a common characterization technique for thin film. W. C. Marra and A.Y. Cho in 1979 proposed this technique while studying GaAs and Al thin film grown on GaAs substrate (Cullity, 1978a). It is

a non-destructive analysis method. The signals produced from the thin film materials are very weak and there is huge interference from the substrate, the traditional powder XRD is not suitable for this purpose. A low angle of incidence close to a critical angle is used to achieve low penetration of X-rays in the matter in GIXRD (Thomas, 2010). Since the angle used is very small and seen as if grazing on the samples, the technique is often named GIXRD. It can also provide precise information about morphology like TEM or SEM. It is also known as Grazing Incidence Wide Angle Scattering (GIWAXS) or just GIXRD while using its wide angles which provide the crystallographic information of the surface structure. The detectors can be moved over the axes for collecting the information from in-plane and out-of-plane. Both planes give complete information about the thin film structure.

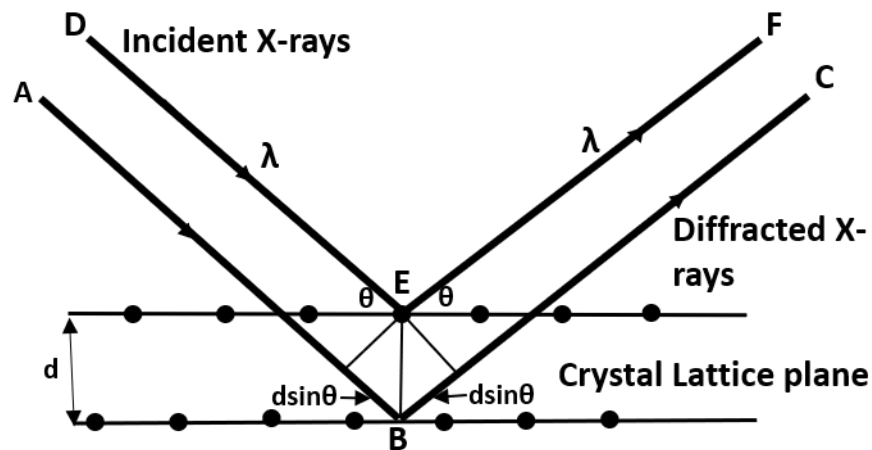


*Fig. 2.1. Diffraction of radiation by crystal planes*

The theory behind X-ray diffraction is Bragg's law (Renaud *et al.*, 2009). Bragg's law is given in equation no. 2.1.

$$n\lambda=2d\sin\theta \quad \dots 2.1.$$

where,

$n$  = integer

$\lambda$  = wavelength of the x-ray

$d$  = space between the reflective layers

$\theta$  = diffraction angle

The beam of x-rays is incident on the sample with an angle  $\theta$ . A diffraction pattern is obtained when the crystalline structure of the sample creates interference in

the incident X-rays. The detector records the diffraction pattern over the  $2\theta$  range. From the obtained data all the possible parameters can be calculated. Every element has unique d-spacing producing a particular diffraction pattern, which can be compared with the established XRD database (Renaud, 1998). The incidence angle is kept very small but little more than the critical angle of total reflection, usually  $< 3^\circ$ . This lower angle controls the penetration power of the x-ray in the thin film.

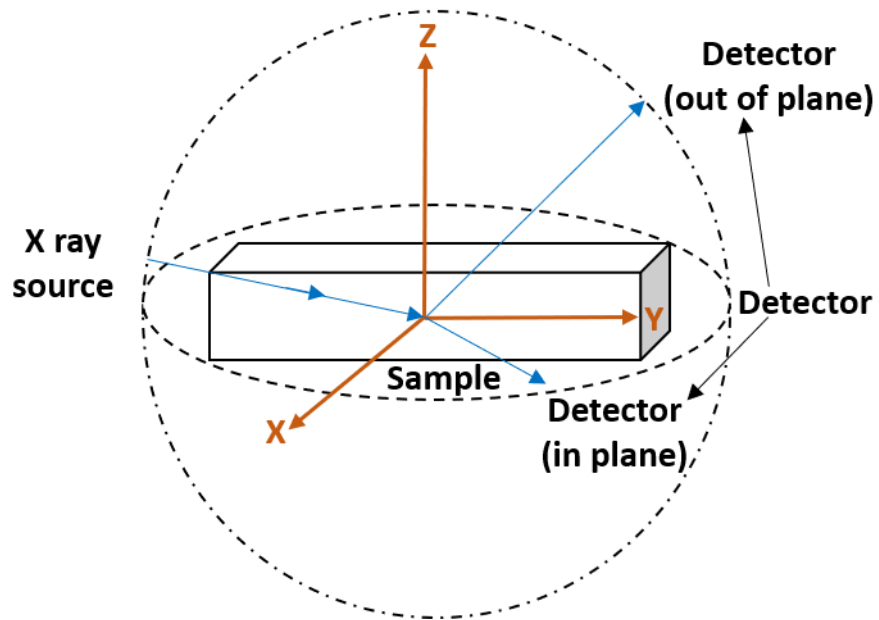


**Fig. 2.2. Schematic diagram of GIXRD setup for out-of-plane and in-plane measurements**

The Miller indices (h,k,l) help to find out the cell constants once they are fixed to the various diffraction patterns. The Miller indices and angle of diffraction are directly related and can be expressed by combining the d-spacing expression with Bragg's law (Pandey *et al.*, 2021). The expressions are given below.

Crystal System	Relationship for $d_{hkl}$	
Cubic	$\frac{1}{d^2} = \frac{h^2+k^2+l^2}{a^2}$	... 2.2.
Tetragonal	$\frac{1}{d^2} = \frac{h^2+k^2}{a^2} + \frac{l^2}{c^2}$	... 2.3.
Orthorhombic	$\frac{1}{d^2} = \frac{h^2}{a^2} + \frac{k^2}{c^2} + \frac{l^2}{d^2}$	... 2.4.

$$\text{Hexagonal} \quad \frac{1}{d^2} = \frac{3}{4} \left[ \frac{h^2 + k^2 + l^2}{a^2} \right] + \frac{l^2}{c^2} \quad \dots 2.5.$$

$$\text{Monoclinic} \quad \frac{1}{d^2} = \frac{1}{\sin^2 \beta} \left[ \frac{h^2}{a^2} + \frac{k^2 \sin^2 \beta}{b^2} + \frac{l^2}{c^2} - \frac{2hl \cos \beta}{ac} \right] \quad \dots 2.6.$$

The XRD has three main components, the sample holder in the middle and X-ray tube and X-ray detectors at the extreme sides. Cathode ray tube produces X-rays by heating the filament. Applied voltage accelerates the electrons and bombards the target dislodging the inner shell electrons of the sample with sufficient energy and producing the characteristic X-rays (Bunaciu *et al.*, 2015). The X-ray produced consists of many wavelengths mainly  $K_\alpha$  and  $K_\beta$ .  $K_\alpha$  also has  $K_{\alpha 1}$  and  $K_{\alpha 2}$  where  $K_{\alpha 1}$  is twice in intensity and a little shorter in wavelength in comparison with  $K_{\alpha 2}$ . Target materials produces the specific wavelength (Cr, Cu, Fe, Mo). For producing monochromatic X-rays, crystal monochromators or filtering foils are used. The most commonly used target is Cu, and the radiation Cu  $K_\alpha$  has the wavelength of 1.5418Å. The peaks obtained from the XRD plot provides many information about the samples tested. Each peak resembles the signature of some particular element when matched with the standard database like International Centre for Diffraction Data (ICDD) (T. C. Huang & Predecki, 1997). The particle size can be calculated using Debye-Scherrer equation given below (Marra *et al.*, 1979; Simeone *et al.*, 2013),

$$D = \frac{k\lambda}{\beta \cos \theta} \quad \dots 2.7.$$

where,

D = mean diameter

k = shape factor

$\lambda$  = wavelength used

$\beta$  = the full width at half maximum (FWHM)

$\theta$  = Bragg's angle.

For all the structural characterization, Smart Lab High-Resolution X-ray Diffractometer from Rigaku with 40kV power and 40mA current was used. The measurement was taken in Parallel Beam  $2\theta$  mode with a Grazing Incidence angle of

1° with 0.02 step size and a scan rate of 4° per minute. The source wavelength used was Cu  $k\alpha$  radiation ( $\lambda=1.54 \text{ \AA}$ ).

## 2.2. UV-Visible Spectrophotometer

The UV-Visible is used to analyse the absorption behaviour of the thin films. Absorption of light by different molecules varies with the wavelength and the wavelength absorbed by particular molecules is recorded by using UV-Vis Spectroscopy. The spectrometer is of two types based on single-beam and double-beam light sources. In a single beam, the reference and the samples are kept successively whereas, in a double beam, a prism or a diffraction grating separates the UV-Vis light source beam into its component wavelengths. The further half-mirrored device splits the monochromatic beams into two equal beams. There are two holders first one for a sample and the second for reference. One beam passes through the sample and another through the reference and the electronic detectors compare the light intensities of both beams. The reference sample must pass all the light and the intensity is denoted by  $I_0$  and since the sample might have absorbed some light, the intensity is denoted by  $I$ .

The result given by the spectrometer for absorbance is based on Lambert-Beer law (Mäntele & Deniz, 2017) given below,

$$A = -\log(T) = -\log(I/I_0) \dots 2.8.$$

where,  $T$  = transmittance ( $I/I_0$ ).

The wavelength  $\lambda$  is plotted on the x-axis and absorbance or transmittance is plotted on the y-axis. There will be  $I=I_0$  if the sample doesn't absorb any light. The difference in the intensity originates from the absorption graph and there is one unique value for  $\lambda_{\max}$  for each sample.  $\lambda_{\max}$  is different for different samples and becomes the signature peak for that particular sample (Joshi *et al.*, 2019).

The UV-Vis spectrometer contains a light source, monochromator, sample holder, detector and an amplifier with indicating device. Mostly two different light sources are used, a deuterium lamp for UV-region (190-400nm) and a tungsten-halogen (300-2500nm) lamp for the visible region. Among all these components the



monochromator usually the grating is the most crucial one. Charged-coupled devices (CCD), Photodiode arrays, photodiodes, and photomultipliers are the different types of detectors used in the UV-vis spectrometer (F. Zhou *et al.*, 2019).

In this work, Absorption and Transmission were recorded by Agilent Cary 5000 UV-VIS-NIR spectrophotometer.

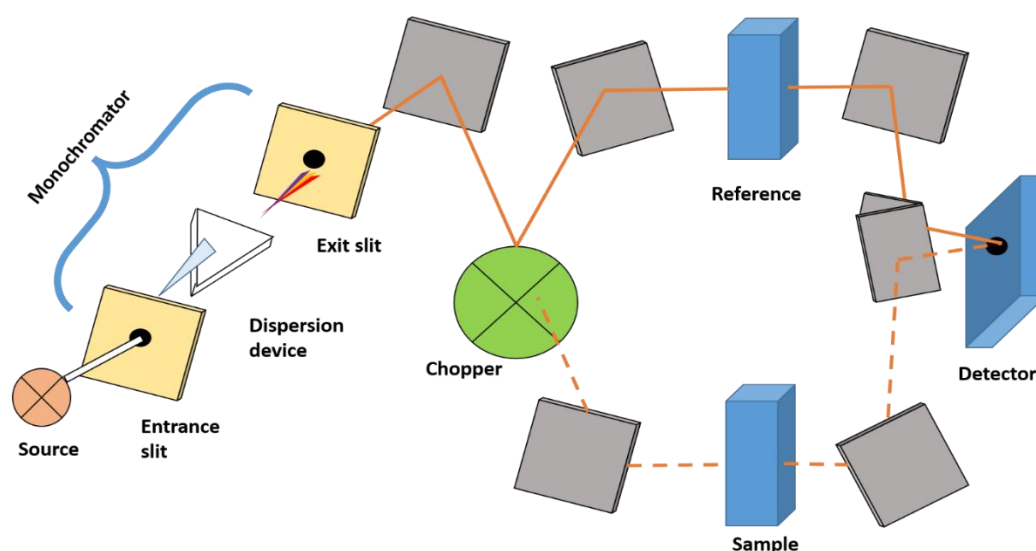


*Fig. 2.3. Schematic diagram of the UV-visible double beam spectrophotometer*

### 2.3. Scanning Electron Microscope (SEM) with Energy Dispersive X-ray Spectroscopy (EDX)

The morphological information is usually given by the SEM. The surface structure, shape and size of the samples can be known with the help of SEM. The high resolution or the high depth imaging is obtained by the generation and evaluation of secondary electrons (backscattered electrons in less amount) with a finely focused beam of the electrons. SEM micrographs are digitally produced images of the samples. The filament is of two types, i) field emission or ii) thermionic emitter. The filament generates the primary electrons when electrical potential and high voltage are applied to it. These electron beams are finely focused by the electromagnetic lenses and scan the surface of the sample systematically. The generation of particles and photons takes place on the surface of the samples with the interaction by the primary electrons.

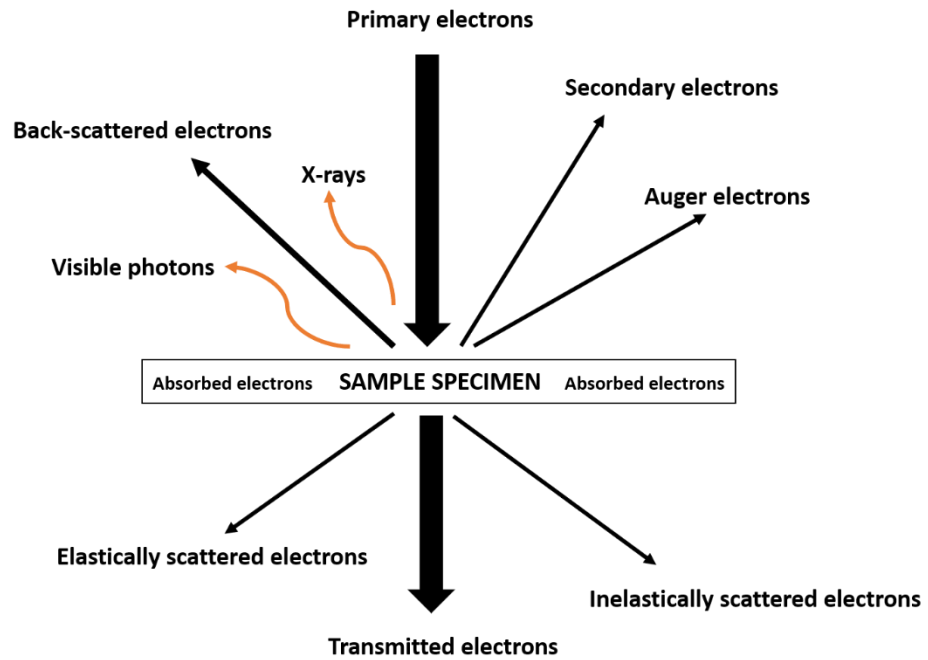


*Fig. 2.4. Interaction of different electrons with the sample*

The back-scattered electrons and the secondary electrons are the most important signals in SEM. Variations in signal intensity of the electron beam at each point of the sample within the scanned area led to the formation of the images (Koster *et al.*, 2000).

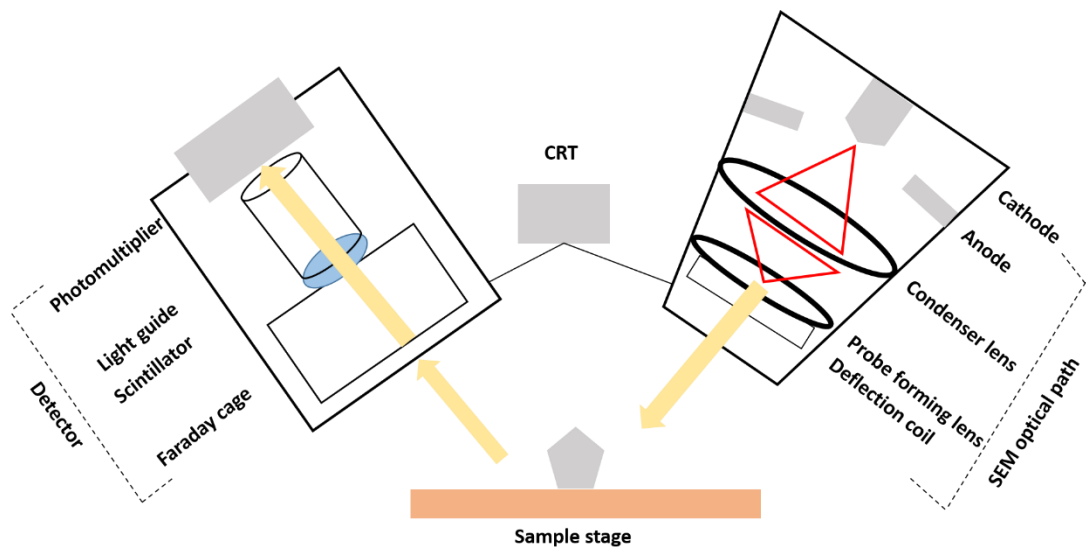


*Fig. 2.5. Schematic diagram showing different components of SEM equipment*

The acceleration of electrons from the field emission cathode is usually controlled by the difference in the voltage between the cathode and the anode. To form a desirable electron probe at the surface of the specimen, the smallest beam cross-section gets demagnified with the electron lens system. Aperture, probe diameter and electron probe current can be regulated to increase the depth of the focus and for changing other parameters as well. A deflection coil system present in front of the final lens is required to scan across the sample and to focus the electron probe. A separate cathode ray tube (CRT) synchronises the electron beam for adjusting the focus and other parameters of the probe. The intensity of the CRT can be modulated to produce the images. The magnification of the images can be varied by changing the current between the coil current and the final scanning beam by keeping the image size constant (Saadaldin *et al.*,2015).

### EDX

The main use of EDX is to determine the composition of the elements in the prepared thin films. This characterization was taken along with the SEM. The incident beam of electrons excites the atoms of the sample which produces the characteristic X-rays. These characteristic x-rays are unique for every element with a particular wavelength.

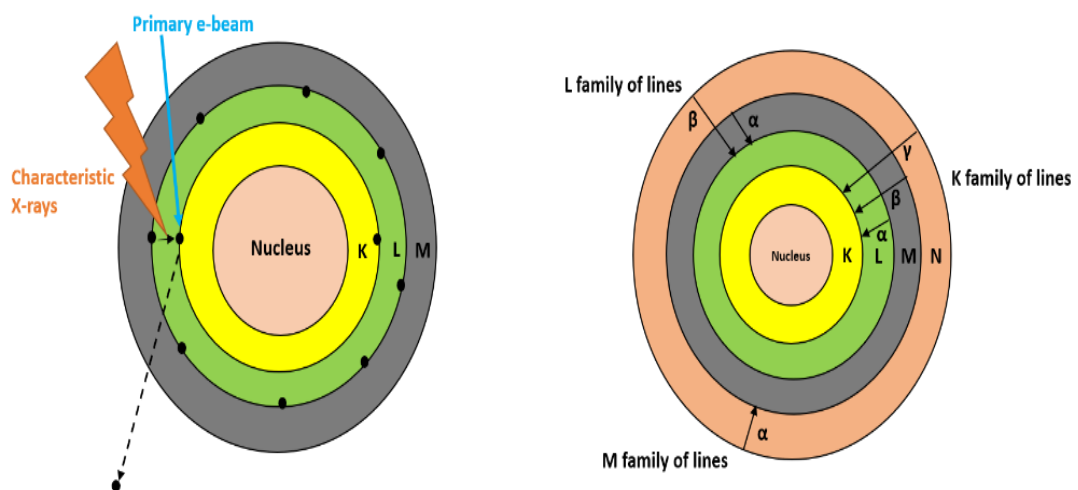


**Fig. 2.6. Diagram showing the generation of characteristic X-ray and their nomenclature**

The incident beam of the electrons irradiates the sample knocking off an electron from the inner shell of an atom and creates a vacancy. This excites the atoms and quickly the excited atom will come back to the normal state when an electron falls into the hole refilling it from the outer shell. Characteristic X-rays are produced as a result of this excessive energy produced during this transition. The differences in energies of the two shells are equal to the energy of characteristic X-rays. The holes in the K-Shell are filled by the electrons in the outer shell producing K-series X-rays. Similarly, the L-series X-rays are also produced. The relative intensities of the X-rays are denoted by the Greek letters  $\alpha$  and  $\beta$ .

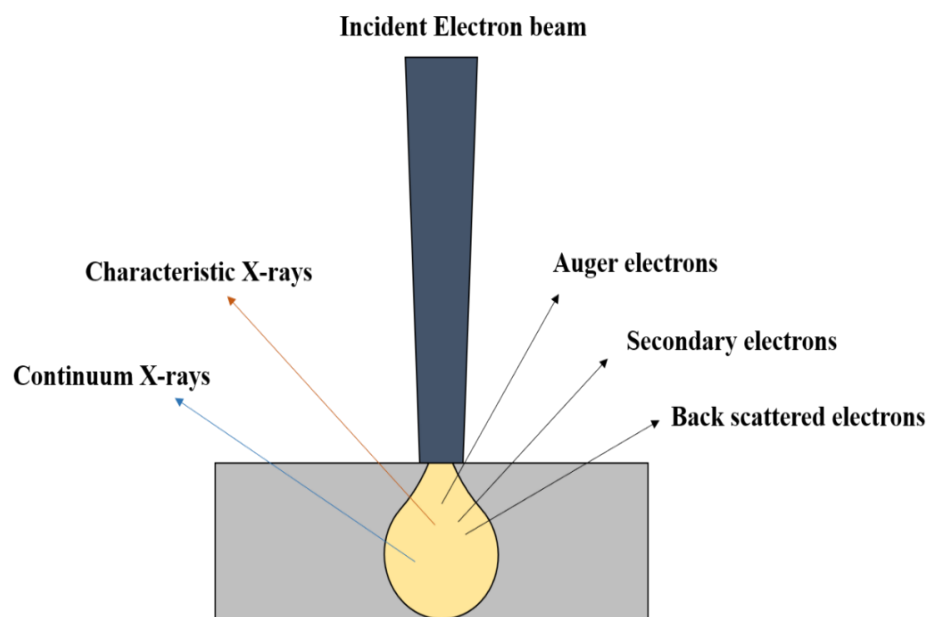


***Fig. 2.7. Different types of signals emitted by incident beam-specimen interaction***

The main components of EDX are the electron beam, detector (Si drift), pulse processor and analyser. The counts or the numbers of the X-ray against the energy level or the wavelength give the measure of the characteristic X-rays when plotted systematically. The semiconductor detector detects the electronic signals emitted by X-rays. The number of currents produced determines the energy of the X-ray photon. When the semiconductor detector is hit by the emitted X-ray photon, produces a very small current, the drift ring within the detector generates the field gradient and the electrons get directed towards the anode.

In this whole work, Field Emission Scanning Electron Microscope (FESEM) micrographs were taken by Supra 55, Gemini FESEM with EDX, Carl Zeiss, Germany.

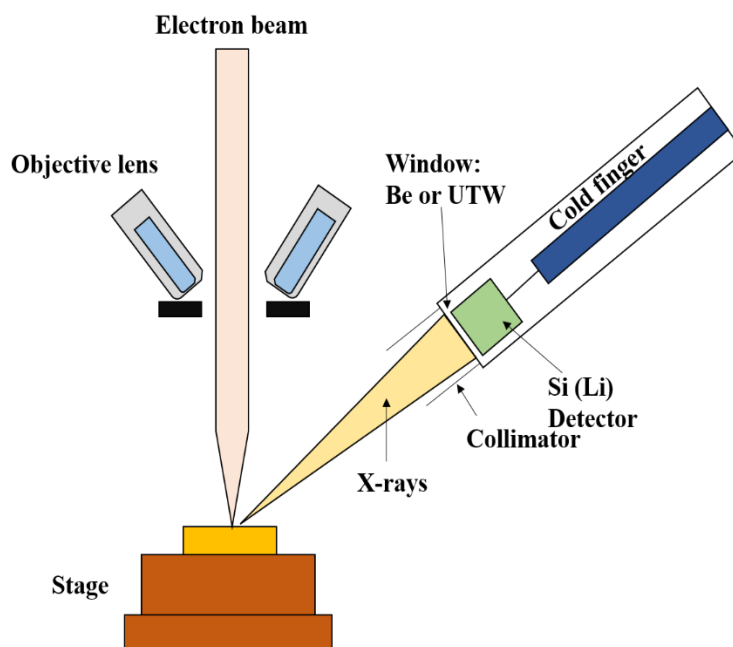


*Fig. 2.8. Schematic diagram for EDX System*

#### 2.4. Photoluminescence (PL) Spectroscopy

In photoluminescence, the light energy (photons) incident on the samples stimulates the emission of the photon. The photon on the sample absorbs the incident photon and relaxes after reaching the higher energy level giving the emission of light while returning to the lower energy level. The luminescence or the emission of light through this method is termed Photoluminescence. This characterization is a non-destructive and non-contact in nature. Emission measured with a single constant wavelength gives the wavelength distribution of the emission spectrum but the excitation is measured upon scanning the excitation wavelength with a single emission wavelength which depends upon the emission intensity.

PL spectroscopy is often used to investigate the optical properties of the material. The emission spectra are useful to investigate the identification of the surface,

and interface with roughness and impurity levels. The information about the interface and the quality of the surface is obtained from the intensity of the PL signal. The electric field on the surface of the sample can also be studied by applying a bias and varying the PL intensity.

The PL spectrometer may contain a Xenon lamp as a source of light for excitation while in some PL spectrometers, the light sources are the LASERs with required wavelengths. The monochromators are used to select the emission and excitation wavelengths. The wavelengths are automatically scanned by motorized monochromators. The monochromator contains gratings as well. The photomultiplier tubes detect the fluorescence and other electronic devices are used for quantification. The sample holder is surrounded by the optical module, the shutters are used for eliminating the exciting light and for closing the emission channel. In the path of excitation light, a beam splitter is also used, which provide a part of excited light to the reference cell. Both the emission and excitation light path contains polarizers. These polarizers are not fixed and can be taken out when not necessary. The unwanted wavelengths and the lights scattered from the emission channel are often reduced by the application of filters. The result is usually seen on the computer screen in graphical form which can be stored digitally.

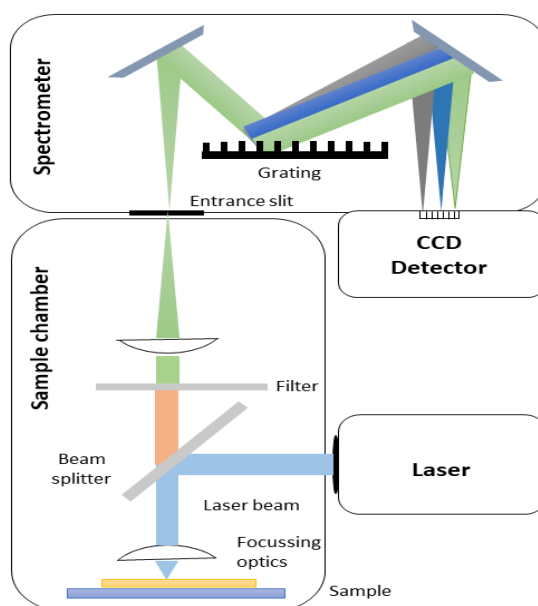


**Fig. 2.9. Representation of components and working of PL spectrometer**

In this whole work, the emission properties of the sample were analyzed through Photoluminescence (PL) spectra by employing a 325nm laser in LabRAM HR-UV-Open Micro-Raman Spectroscopy, HORIBA Scientific, France.

## 2.5. X-ray Photoelectron Spectroscopy (XPS)

The XPS is used to determine the chemical composition of the samples along with the oxidation states of an element and the binding energies of the respective electrons. The kinetic energy of the photoelectrons is analysed corresponding to the X-ray radiations applied in the experiments. XPS is also a non-destructive method for characterization. The area of the samples to be tested is some millimetre square and the depth is around 10 nm.

The samples are kept in an ultra-high vacuum chamber to prevent the collision between the gas phase molecules and the photoelectrons under the pressure in range of  $10^{-10}$  to  $10^{-7}$  mbar. Magnesium  $K_{\alpha}$  (1253.6 eV) and Aluminium  $K_{\alpha}$  beams are the common X-ray radiation used in XPS. Monochromators or sometimes synchrotrons are used to obtain a single wavelength. An electric field is applied to detect the kinetic energy of the ejected photoelectrons. Among all the ejected electrons only a few with optimum energy reach the detector and are counted.

In XPS the used X-ray beam usually ejects the electrons from the sample when incident on a particular area. Once the electrons are ejected, they create holes at that place. Again, these holes are filled with the electrons from the higher energy levels and create X-ray fluorescence radiation or sometimes radiationless Auger electrons are also ejected. The energy on the ejected electron can be understood by the given equation applying the conservation of energy;

$$E_r = E_{kin} + E_b + \Phi \quad \dots 2.9.$$

where,

$E_r$  = Energy of the incident X-ray ( $h\nu$ ),

$E_{kin}$  = Kinetic Energy of ejected electron

$E_b$  = Binding Energy of the Photoelectron

$\Phi$  = work function of the spectrometer (causes the energy loss)

The energy of the incident X-ray is divided into mainly three components of the photoelectrons. XPS helps to investigate the electrons in terms of their binding energy corresponding to their orbitals. The information about the oxidation state, the chemical behaviours and the effective charge are obtained from the binding energy of the core electrons. The results are expressed by plotting the intensity (counts) versus either the binding energy or kinetic energy of the photoelectrons. The area under the plot provides information about the composition of the sample.

For the understanding of the chemical compositions of the samples prepared in the work, XPS with 5000 versa probe III, PHI was used.



***Fig. 2.10. X-ray Photoelectron Spectrometer used for this research work***



## 2.6. Hall measurement

The principle behind the Hall effect can be considered as the extension of the Lorentz Force, the forces which pass through the magnetic fields acting on the charge carriers i.e., electrons and the holes when exposed to the magnetic and electric fields. This effect was named after the American scientist Edwin H. Hall in 1879. This method is used in various applications like magnetic field sensing, Tong Tester, linear or angular transducer, proximity sensors etc. For thin film, many different parameters can be measured such as resistivity, mobility, types of semiconductors and more.

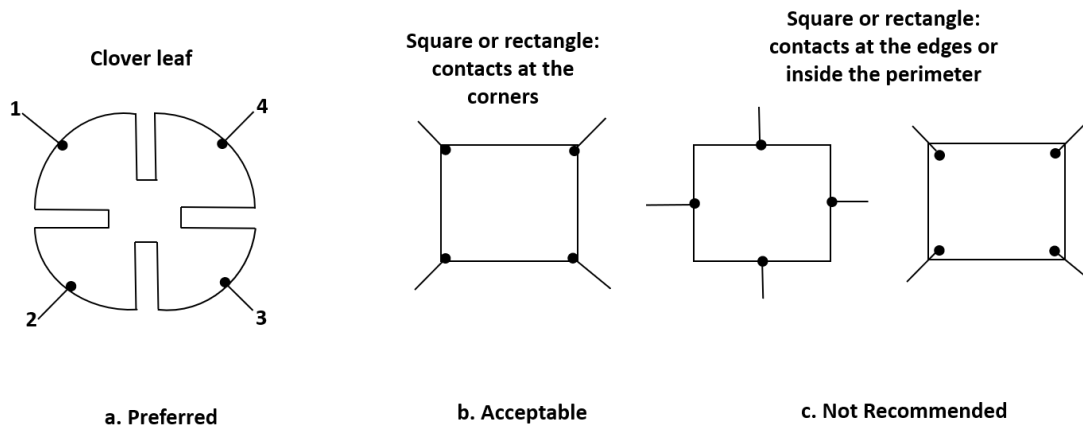


**Fig. 2.11. Different types of contacts for samples in the Hall measurement**

In our work, we are interested in calculating the carrier mobility and the types of semiconductors. For calculation, we require to know Hall voltage  $V_H$  and it can be calculated using the following equation

$$V_H = \frac{IB}{qnd} \quad \dots 2.10.$$

where,

$I$  = current flowing through the sample

$B$  = Magnetic Field Strength

$q$  = charge

$n$  = number of charge carriers per unit volume

$d$  = sample thickness

For the calculation of the charge carrier concentration ( $n$  for electrons and  $p$  for holes), we use the following mathematical expression,

$$n \text{ or } p = \frac{1}{qR_H} \quad \dots 2.11.$$

where  $R_H$  = Hall Coefficient

and the Hall mobility for hole and electron is given by

$$\mu_p = \sigma R_H \text{ (for holes)} \quad \dots 2.12.$$

$$\mu_n = \sigma R_H \text{ (for electrons)} \quad \dots 2.13.$$

where  $\mu$  is the conductivity.

The thin film is kept in a four-probe holder and kept in between the electro-magnet of 1.5 Tesla for the measurement.

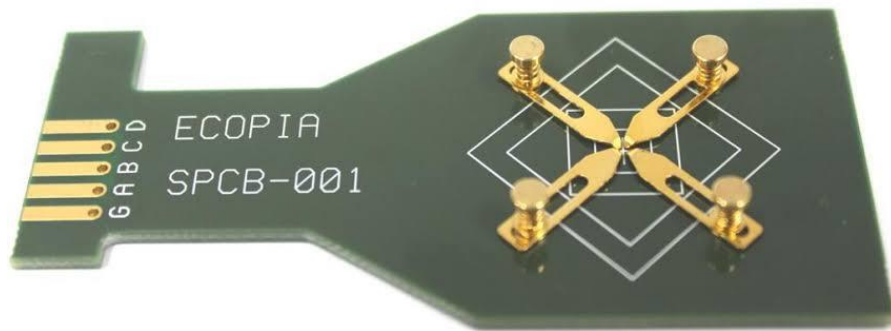


*Fig. 2.12. Four probe clips for holding the thin film samples*

## CHAPTER 3

### SYNTHESIS AND CHARACTERIZATION OF ZnO NANO PARTICLES (np), ZnO THIN FILM AND ZnO NANORODS (nr) AS ELECTRON TRANSPORT LAYER

#### INTRODUCTION

The role of the electron transport layer (ETL) is important in the performance of the PSCs. It is a major component of the PSCs which helps in extracting the photo-generated electrons and suppressing the carrier recombination by blocking the holes. The energy band gap, carrier mobility, and morphology are the few properties of any ETL to enhance the PCE of the PSCs (Lakhdar & Hima, 2020). The transportation of charge also depends upon the trap states in the ETLs so the improvement in the interface between the perovskite layer and the ETL also optimizes the efficiency of the PSCs. Before ZnO, inorganic TiO<sub>2</sub> was mostly used as an ETL in PSCs (L. Lin *et al.*, 2020). Although, the rate of charge transfer between the Perovskite layer and the TiO<sub>2</sub> layer was fast whereas the electron mobility was low and the recombination rate was high. The search for a similar type of semiconductor with improved properties for ETL was fulfilled by ZnO (Spalla *et al.*, 2019). The ZnO was found to be an ideal candidate for ETL as its mobility was higher than that of TiO<sub>2</sub> (Mohamad Noh *et al.*, 2018).

ZnO is a wide band gap (3.37 eV) semiconductor of the II-VI group with large exciton binding energy (60meV) (Tsarev & Troshin, 2020). Due to its various good properties, it can be used in different fields like optoelectronics, water-splitting device, sensors, solar cells, UV emission devices, non-volatile memory, pH sensors, biosensors etc. (Ko *et al.*, 2018; Kumar *et al.*, 2020; Luo *et al.*, 2018; Mahmud *et al.*, 2017; Ouyang *et al.*, 2019). The interest in ZnO has increased because of its various easy synthesis methods (Taheri-Ledari *et al.*, 2020). ZnO can be synthesized by spray pyrolysis, chemical vapour deposition, RF sputtering, and the Sol-gel technique (hydrothermal). In this work, sol-gel (hydrothermal) technique is employed for ZnO nanoparticles (np) and nanorods (nr) (Sharma *et al.*, 2018; Son *et al.*, 2014).

### 3. Experimental

#### 3.1. Materials

Zinc Acetate dihydrate (ZAD) [ $\text{Zn}(\text{CH}_3\text{COO})_2 \cdot 2\text{H}_2\text{O}$ , 98% purity], Zinc nitrate hexahydrate (ZNH) [ $(\text{Zn NO}_3)_2 \cdot 6\text{H}_2\text{O}$ , 98% purity], Sulphuric acid [ $\text{H}_2\text{SO}_4$ , Emparta ACS grade, 98% purity], Acetone [ $\text{C}_3\text{H}_6\text{O}$ , Emplura grade, 98% purity], Hydrogen peroxide [ $\text{H}_2\text{O}_2$  Emparta grade, 30% purity], 2-propanol [ $\text{C}_3\text{H}_8\text{O}$ , Emplura grade, 99% purity], Sodium Hydroxide pellets [ $\text{NaOH}$ ], Hexamethylenetetramine (HMT) [ $(\text{C}_6\text{H}_{12}\text{N}_4)$ , 99% purity] were purchased from Merck Chemicals; Monoethanolamine (MEA) [ $(\text{C}_2\text{H}_7\text{NO})$ , 98% purity], 2-methoxyethanol (2ME) [ $(\text{C}_3\text{H}_8\text{O}_2)$ , 99% purity] and Tetramethylammonium hydroxide (TMAH or TMAOH), Ammonium chloride [ $(\text{NH}_4\text{Cl})$ , 98+% purity] were obtained from Alfa Aesar, Diethanolamine [ $\text{C}_4\text{H}_{11}\text{NO}_2$ , 98%], Dimethyl Sulfoxide (DMSO) [ $(\text{C}_2\text{H}_6\text{OS})$ , 99.9% purity], N,N-Dimethyl formamide (DMF) [ $(\text{C}_3\text{H}_7\text{NO})$ , 99.8% purity], Fluorine doped Tin oxide (FTO) substrates were obtained from Sigma Aldrich. All the chemicals were not purified further before use.

#### 3.2. Methods adopted for synthesizing ZnO nr and ZnO np

The FTO Substrate were cleaned in ultrasonication using Acetone, 2-propanol and DI (Deionized) water each for 15 minutes and dried in a hot air oven for 4 h at  $90^\circ\text{C}$  in the normal environment. In the first step, the ZAD (0.3M) was dissolved in 2ME followed by stirring at  $60^\circ\text{C}$  and after 5mins MEA was also added maintaining the ratio of 1.1. The solution was transparent and kept for ageing for 24 h. The FTO substrates were coated with the obtained solution in the spin coating unit with 3000 rpm for 30 sec and dried at  $300^\circ\text{C}$  for 10 min on the hotplate. Each substrate was coated ten times and then kept in the furnace for annealing for 1 h at  $500^\circ\text{C}$ . After that, the final ZnO thin film is prepared.

Now, in the second step, HMT and ZNH were mixed to prepare an equimolar solution. In this solution, the previously prepared thin films were submerged in an inverted condition for 5 h at  $90^\circ\text{C}$ . The ZnO nr start growing on the seed layer. These

grown nanorods are taken out of the solution and washed with DI water for eliminating any kind of impurities. The synthesis procedure is also depicted in fig. 3.1.

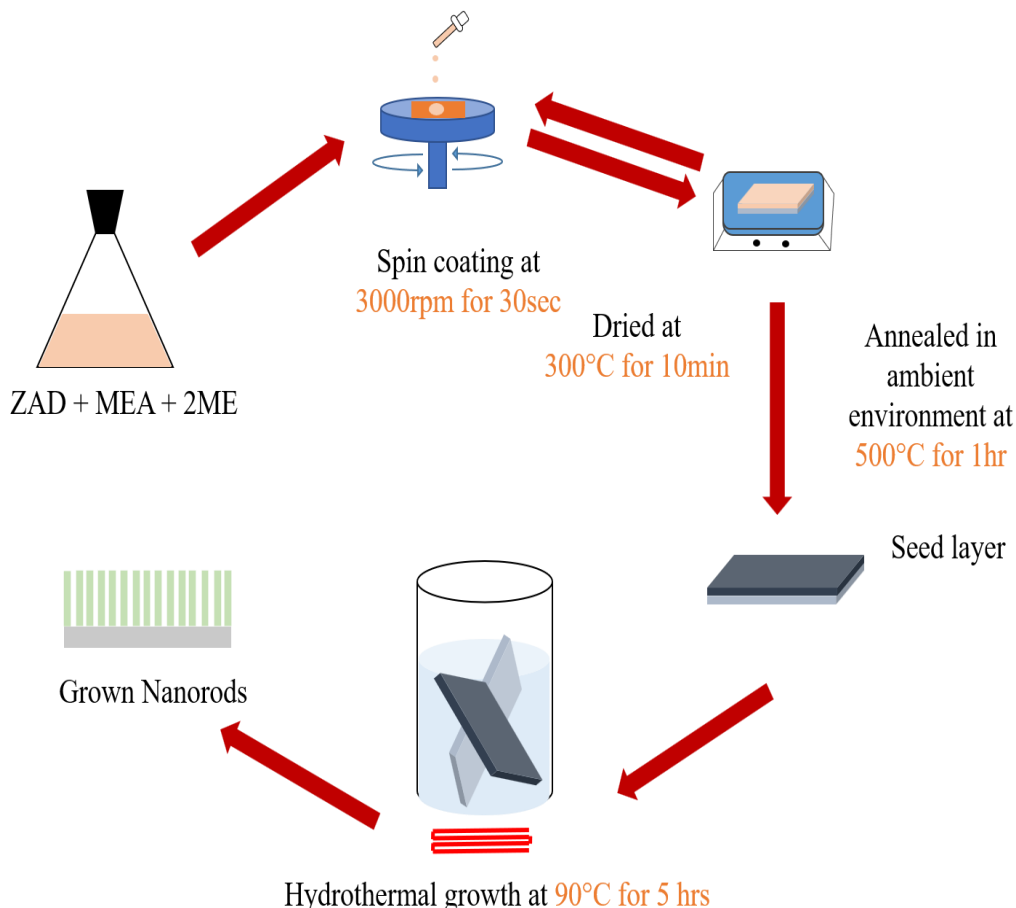


**Fig. 3.1. Flowchart for preparing ZnO thin film and the ZnO nanorods**

The ZnO np were prepared separately for preparing a thin film by dispersing on the top layers of perovskites. 3 mmol of ZAD was dissolved in 30 ml of DMSO and 10 ml of ethanol dissolved 5mmol of TMAH and this solution was added in the first solution dropwise at the rate of 8ml per min. The reaction proceeded for 1 h at room temperature. The ZnO np were obtained by precipitation by adding an excess of acetone and again dissolved in ethanol for redispersion. This solution is used for preparing ZnO np layer over the substrate as ETL in the PSCs. The ZnO np layer was spin-coated with 1500 rpm for 60 secs and followed by baking at 60<sup>0</sup>C for 30 min.

### 3.3. Results and discussions

#### 3.3.1. Structural properties

The structural properties of the ZnO nr and ZnO np thin films were analysed from the XRD patterns. The crystalline nature is confirmed by the XRD graph.

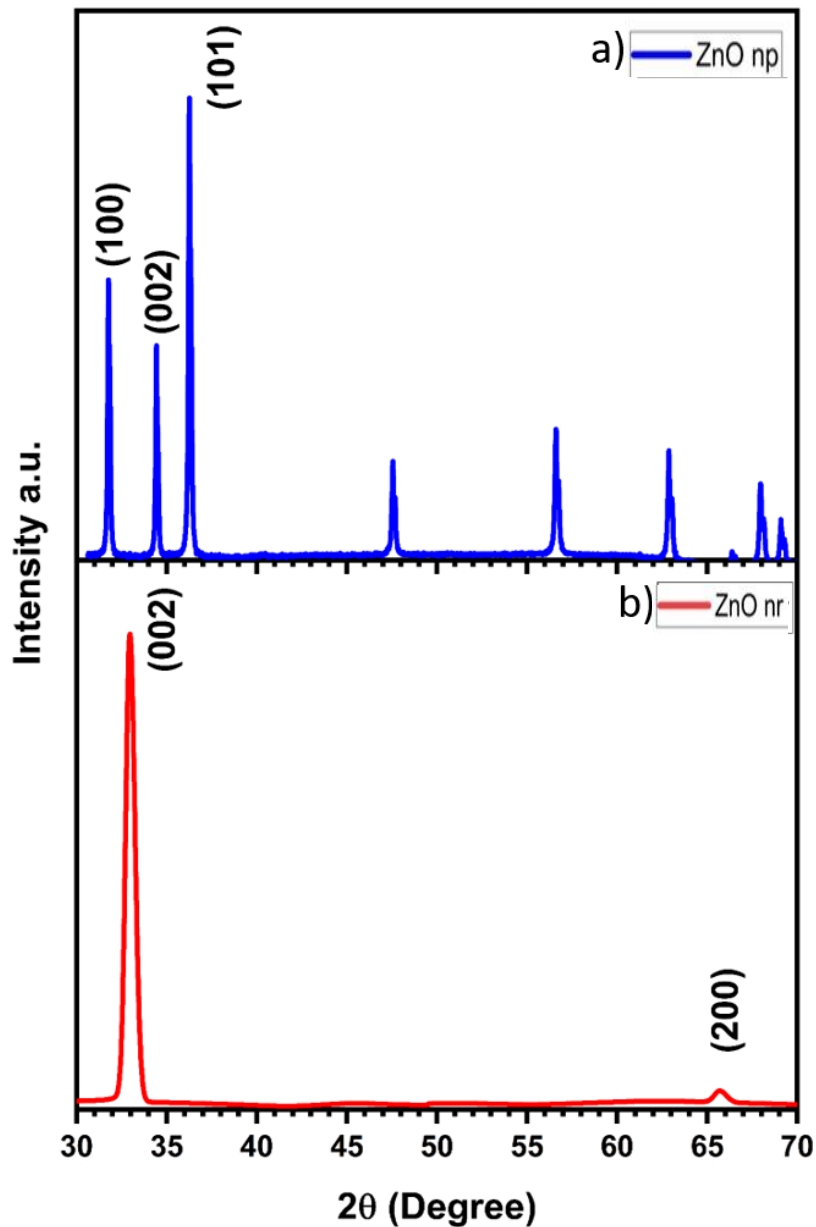


*Fig. 3.2. XRD graphs of a) ZnO np and b) ZnO nr*

Fig. 3.2. depicts the XRD patterns of the ZnO nr and ZnO np. The hexagonal wurtzite structure of the ZnO nr was confirmed by the obtained diffraction peaks which

match with the JCPDS card no 36-1451. The strong (002) peak at nearly  $34^\circ$  suggests the good crystallinity and purity of the nanorods. The reflection from (002) plane is higher than other peaks which indicates that the growth of the crystal has occurred along the c-axis that agrees with the previous reports (Sharma *et al.*, 2018). For nanoparticles the (100), (002) and (101) are the signature peaks. These peaks are in agreement with the ICDD card no. 00-005-0664. For calculating the average crystalline size (D), Debye Scherrer equation (equation 2.7) was used. The average crystalline size of ZnO np was observed in the range of 86-112nm and for the ZnO nr the average size of the diameter ranges from 155-186 nm. The height of the ZnO nr were in the range of 2.7-2.9  $\mu\text{m}$ .

### 3.3.2. Optical Properties

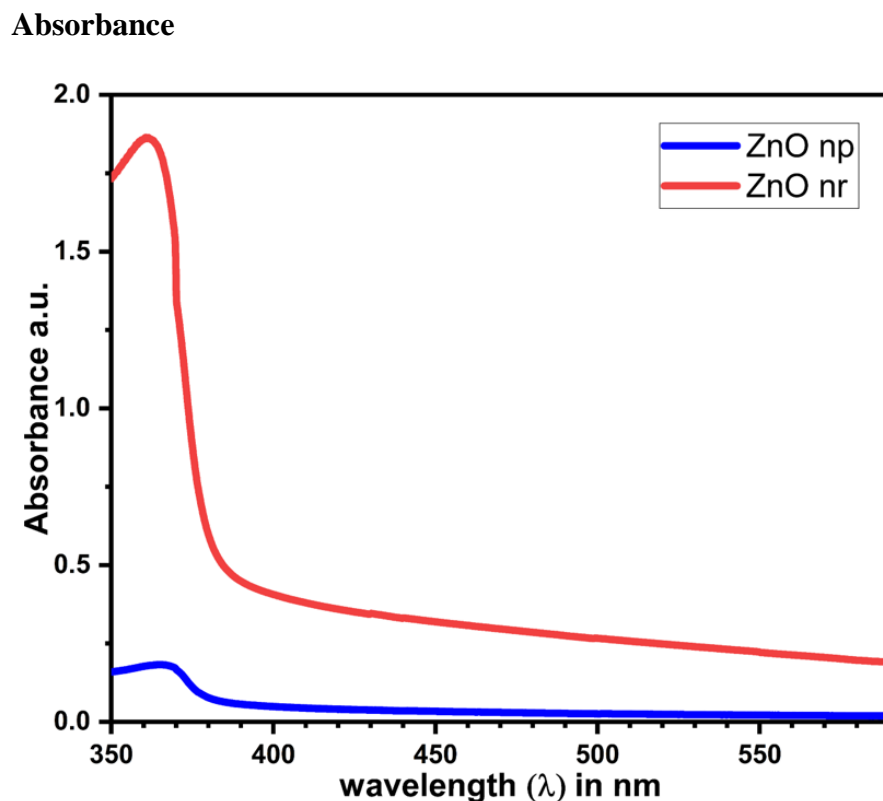


*Fig. 3.3. Absorbance of ZnO np and ZnO nr*

The absorption in the visible region helps to understand the many optical properties of the sample. It provides broad information about the band structure and the energy band gap of the sample. Here fig. 3.3. represents the absorption of the ZnO

nr and ZnO np. The tunability of the band gap of ZnO offers good application in different fields. In our work, the band gap for ZnO nr and ZnO np is found to be 3.27 eV and 3.28 eV respectively. The band gap was obtained from Tauc's plot which are shown the fig. 3.5. and fig. 3.6.

### Transmittance

The transparency of the ZnO as ETL is also an important property to be used in the PSCs. The transmittance of ZnO np is more than 80% and that of ZnO nr is more than 60%. The thickness of the ZnO nr is quite more than that of the ZnO np due to which the transparency is decreased. The transmittance is shown in fig. 3.4.

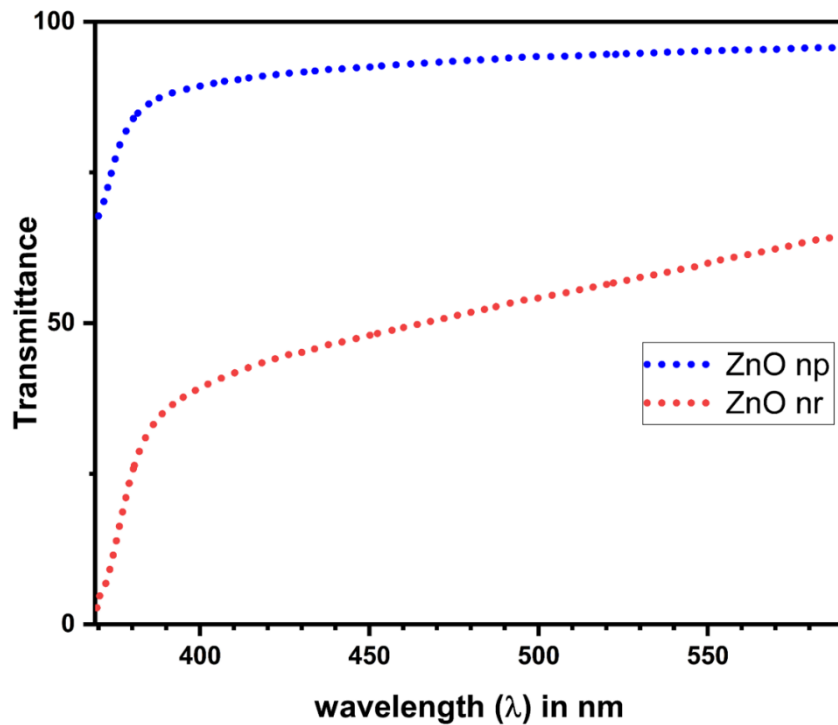


*Fig. 3.4. Transmittance of ZnO np and ZnO nr*



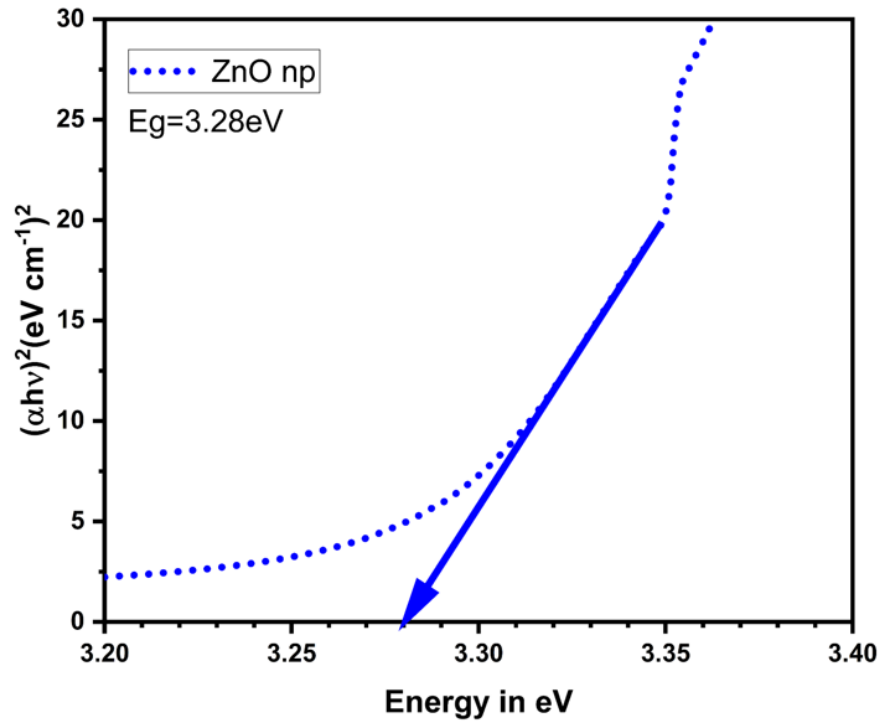


Fig. 3.5. Band gap of ZnO np

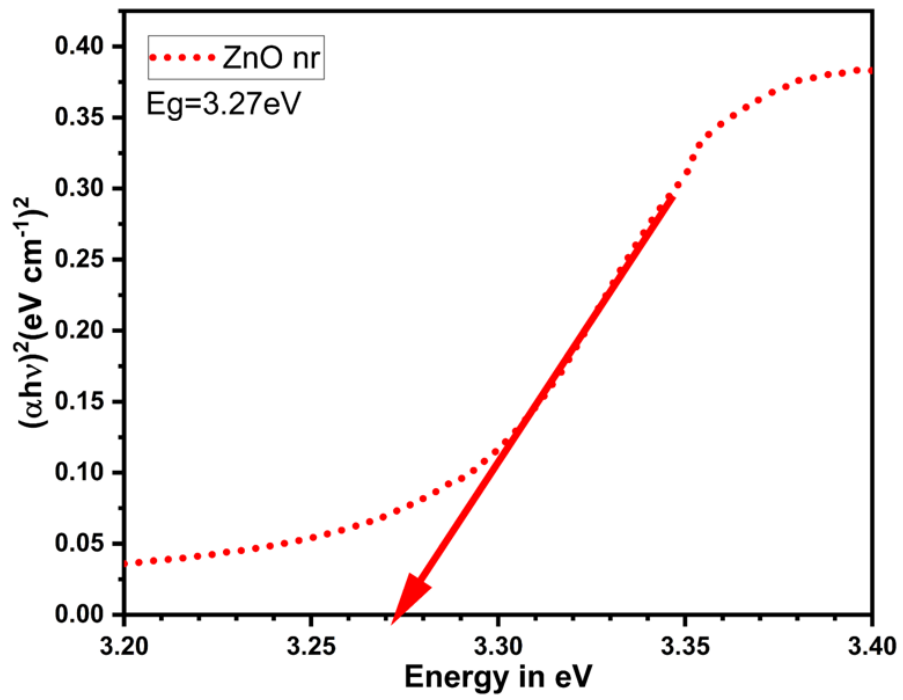
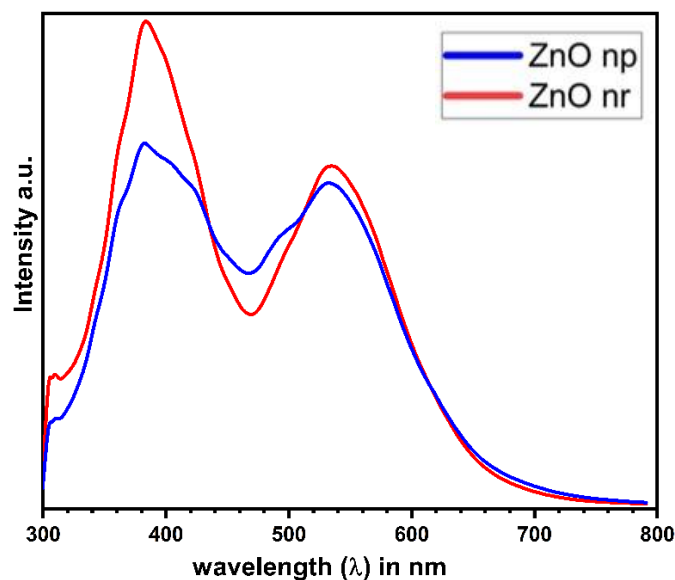


Fig. 3.6. Band gap of ZnO nr

### Photoluminescence (PL)

The room temperature photoluminescence is taken with 325 nm excitation wavelength in the range of 300–800 nm. PL spectroscopy helps in the study of the different forms of structural defects present in the sample. The common defects occurring in the semiconductors are the zinc and oxygen interstitials and vacancies in the ZnO nanostructures (Kumar *et al.*, 2020; Qiu *et al.*, 2017). These defects cause various radiative recombination transition of electrons from conduction band in one case or from trapping levels. The recombination process of the electron-hole pairs and their transfer also can be understood with the PL (Bhujel *et al.*, 2020). The ZnO nr and ZnO np has UV emission (near band emission) at 385 nm and 383 nm and deep-level emission (DLE) at 533 nm and 532 nm respectively. The excitonic recombination causes the UV emission and the combination of photogenerated holes along with the vacancies and defects causes the DLE. The peaks at the UV region are attributed to surface states or band tail states in ZnO (Sharma *et al.*, 2018). The peaks in the 450-650 region (DLE) could be present due to the native defects (i.e. optical centres associated with impurities) (Dong *et al.*, 2015; Fang *et al.*, 2013). The peaks at 533 nm can be caused due to surface defects and oxygen vacancies. The enhanced recombination leads to higher intensities of the ZnO nr than that of ZnO np (Qiao *et al.*, 2016).



*Fig.3.7. PL graph of ZnO nr and ZnO np*

### 3.3.3. Morphological Properties

FESEM images of fig. 3.8 (a, b, c and d) show the surface morphology and the cross-section view of the sample. The ZnO np and ZnO nr both are distributed uniformly. The average crystallite size of ZnO np and the average diameter of ZnO nr were found to be 90 nm and 160 nm respectively. There may be little difference in the measurement of size from XRD data and the data from FESEM images because XRD gives the average size but in FESEM the individual size can also be calculated. The ImageJ software and Smart SEM software were employed to calculate the size. The cross-section of the nr shows that the average height of the nr is around 2.8  $\mu\text{m}$ .

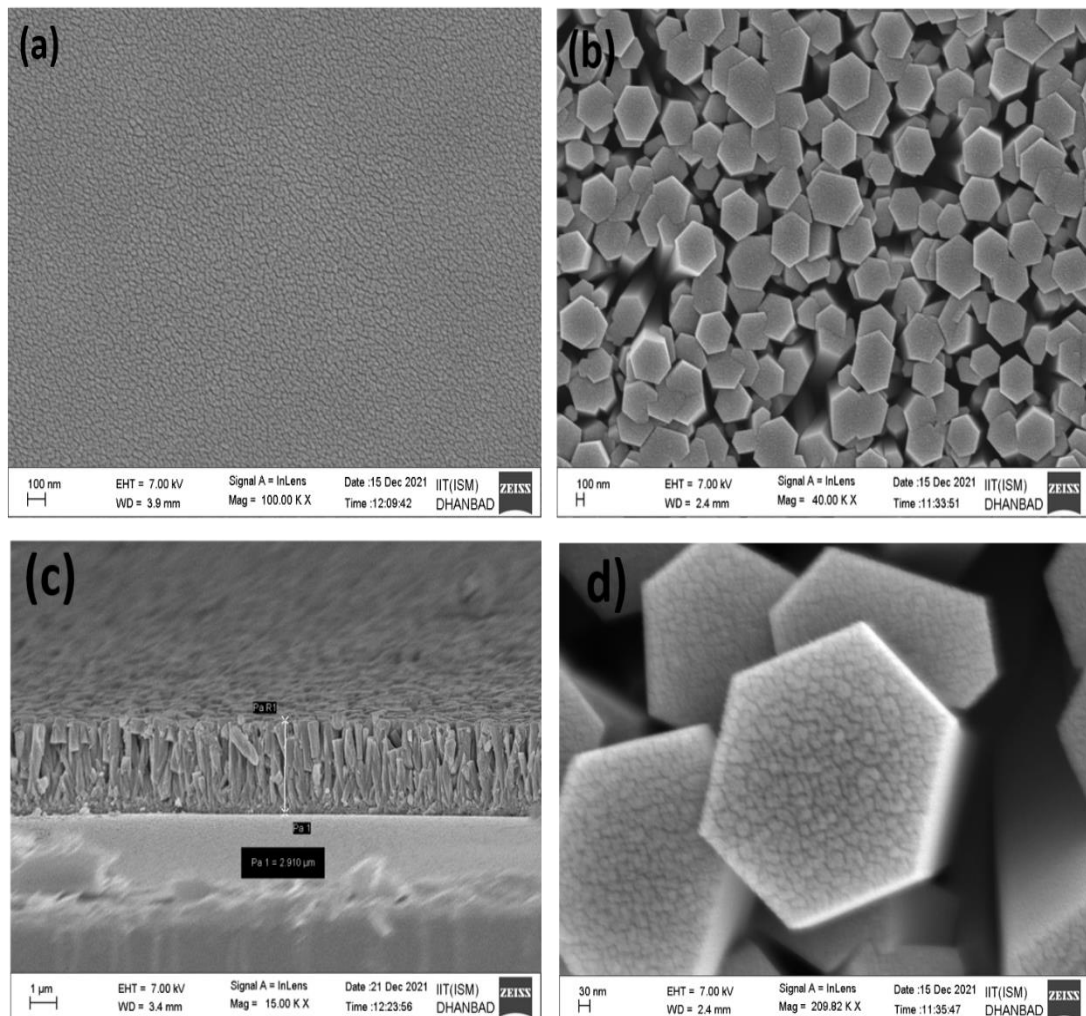


**Fig. 3.8. a) FESEM image of ZnO np b) FESEM image of ZnO nr c) Cross-section Image of ZnO nr d) Near view of ZnO nr**

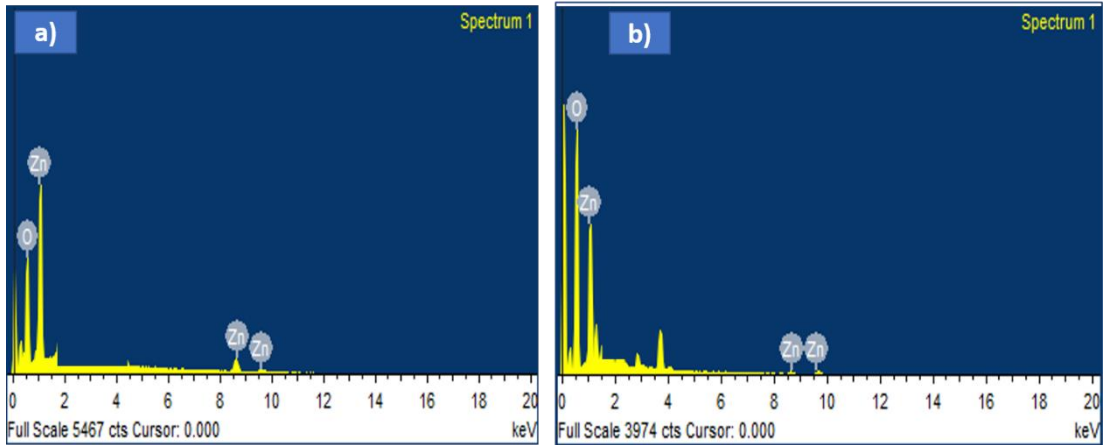


*Fig. 3.9. a) EDX of ZnO np b) EDX of ZnO nr*

### 3.3.4. Electrical Properties

The current-voltage (I-V) characteristic graph for ZnO np and the ZnO nr are shown in fig. 3.10. under the light illumination at room temperature. The measurement was taken in the range of -0.4 to +0.4 V. The enhancement in photocurrent in ZnO nr can be assumed because of its thickness and uniformity of the surface. The carrier concentration is calculated from hall measurement and found to be  $1.118 \times 10^{19}$  and  $1.208 \times 10^{19} \text{ cm}^{-3}$  for ZnO np and ZnO nr respectively.

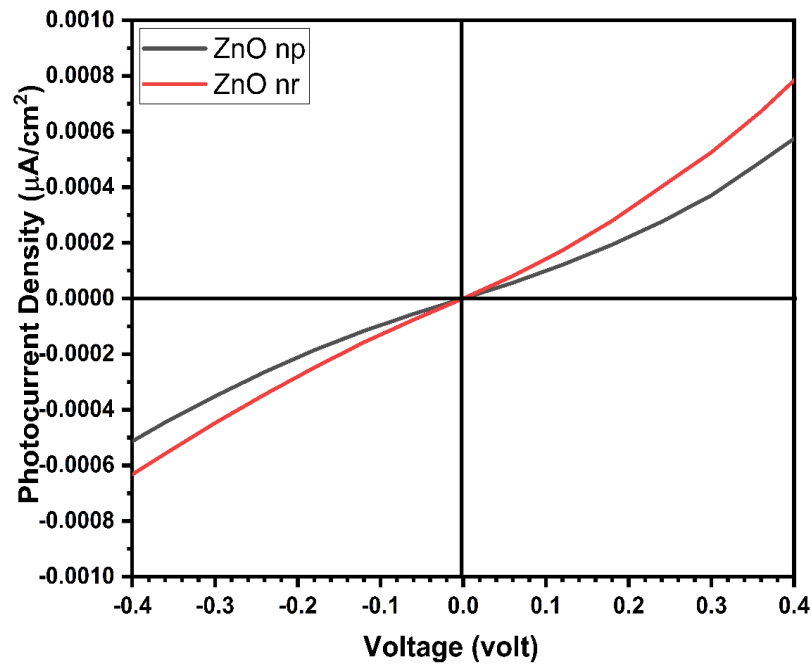


*Fig. 3.10. J-V graph of ZnO nr and ZnO np*

### 3.4. Conclusion

ZnO nr and ZnO np were synthesized successfully. The structural properties revealed the high crystallinity of the substances. The morphology was studied with the FESEM and the composition was confirmed by the EDX graph. The optical band gap was in accordance with the reported data. ZnO np had better transmittance than the ZnO nr. The electrical property showed that the J-value for ZnO nr is greater than that of the ZnO np. The ZnO nr had greater carrier concentrations ( $1.208 \times 10^{19} \text{ cm}^{-3}$ ) than that of ZnO np ( $1.118 \times 10^{19} \text{ cm}^{-3}$ ). ZnO nr may be well efficient to be used as ETL in PSCs where ever possible. There is a limitation of the applicability of ZnO nr to be used in PSCs, that it can only be used in the n-i-p configuration of the PSCs. It is not easy to grow ZnO nr above the perovskite layer. So, in the p-i-n configuration of PSCs, ZnO np is dispersed as a thin layer of ETL.

## CHAPTER 4

# SYNTHESIS AND CHARACTERIZATION OF NiO AND Cu:NiO THIN FILMS AS HOLE TRANSPORT LAYER FOR PEROVSKITE SOLAR CELLS

## INTRODUCTION

The NiO thin films are now very common HTL in PSCs. It is a p-type semiconductor and is very useful in collecting holes in PSCs. NiO has become a good and promising Transparent Conducting Oxide (TCO) (Manders *et al.*, 2013). Previously, PEDOT:PSS an organic HTL was being used extensively but it had some limitations like its electron-blocking nature was very poor, hygroscopic and acidic in nature which caused significant degradation in the output of PSCs. For good cell efficiency, the electrons have to be blocked properly otherwise there will be high recombination at the interface. HTL must have good Ohmic contact with the electrodes and it must be stable for a longer duration with good transparency. Most of these properties are possessed by NiO and thus have been used as HTL in this work. Many possibilities for improving the PCE of the PSCs can be seen with the introduction of NiO thin film as an HTL in PSCs. Doping with Copper also affects the performance of the cell as doping plays a vital role in improving the carrier mobility leading to increased efficiency of the PSCs (Benramache *et al.*, 2020; Li *et al.*, 2017a; X. Yang *et al.*, 2018).

NiO possesses a cubic structure and belongs to the space group Fm3M. NaCl also has a similar structure. Its wide band gap nature (3.6-4.0eV) also facilitates use in more different applications. The NiO thin films can be synthesized from different types of routes. Direct deposition on the spin coating, pulsed laser deposition (PLD) (Franta *et al.*, 2005), spray pyrolysis (Aftab *et al.*, 2021), atomic layer deposition (ALD) (Hsu *et al.*, 2015), sputtering (Sato *et al.*, 2016a), combustion method (Li *et al.*, 2017a), a sol-gel-spin coating method (Sahoo & Thangavel, 2018), electrochemical deposition (L. Zhao *et al.*, 2011), chemical precipitation method (Aliahmad *et al.*, 2014) are the common existing synthesis methods for preparing the NiO thin films. In our work, we have employed the sol-gel-spin coating method for depositing the NiO thin films as it

is user-friendly and very cost-effective. There are various applications of NiO thin films and nanoparticles as well. It is used in optoelectronic devices (Mohammed *et al.*, 2021), HTL in PSCs (Bashir *et al.*, 2019), hybrid nano lubricants as oil compressors (Akkaya & Akman, 2021), plasmonic photocatalysts for polar H<sub>2</sub> evolution (Z. Lin *et al.*, 2018), antifungal response (Aftab *et al.*, 2022), photocatalytic performance (Varunkumar *et al.*, 2018) etc.

The HTL is considered very good if its  $E_g > 3\text{eV}$  and is chemically stable possessing good conductivity. In comparison, NiO has overcome the problems faced by the use of PEDOT:PSS. For the first time, NiO as HTL was applied by Steirer *et al* replacing the PEDOT:PSS (Steirer *et al.*, 2010). They tailored the work function of NiO by O<sub>2</sub> plasma treatment but they failed to understand the real effect clearly. Uniformity was obtained by the thicker films with lower open-circuit voltage (Voc), lower short-circuit current density (Jsc), and higher series resistance. There was non-uniformity in the thinner films with incomplete coverage leading to inconsistent performance (Dawood, 2015). The application of NiO as HTL in BHJ polymer cells was done by Hsu *et al* for the first time. It was prepared by ALD, so the film was defect-free and uniform. The coverage was complete and had precise thickness control while deposition. They optimized thickness at 4nm and obtained a PCE of 3.38% (Hsu *et al.*, 2015). You *et al.* showed that the solution-processed NiO as HTL improved air stability. The maximum PCS obtained was  $14.6\pm 1.5\%$ . glass/ITO/NiO<sub>x</sub>/CH<sub>3</sub>NH<sub>3</sub>PbI<sub>3</sub>/PCBM/Al was the structure of the solar cell device (You & Noh, 2021). Kim applied polyethylene glycol (PEG)- assisted sol-gel method for NiO thin film preparation. It improved the smoothness of the morphology obtaining the uniform surface of the thin film significantly changed the properties of the interface between the layers. The inclusion of PEDOT:PSS along with the NiO layer as a hybrid HTL layer, helped in good extraction of charge and suppressed the recombination of the charges. They improve the PCE of the cell from 5.68% to 6.91%. The doping of different elements in NiO also has shown good improvement in the PCE of solar cell devices (J. K. Kim, 2019). Jung *et al.*, prepared Cu:NiO via the low-temperature combustion method in methylammonium lead halide perovskite and improve the PCE from 15.52% to 17.8% with the temperatures at 150<sup>0</sup> C and 500<sup>0</sup> C (conventional

method) respectively. The grain size was increased by the Cu doping in NiO thin film and influenced the surface morphology resulting in a decrease in transmittance. The optical band gap was lowered in Cu:NiO (3.69eV) compared to the undoped NiO thin film (3.73eV) (Jung *et al.*, 2015). Doping also affected the conductivity at the different annealing temperatures. So, the research on the application of NiO thin film as HTL has been going on in various parts of the world rigorously.

## **4. Experimental**

### **4.1. Materials**

Nickel (II) Acetate hydrate (NiAc) [ $\text{Ni}(\text{CH}_3\text{COO})_2 \cdot x\text{H}_2\text{O}$ , 99% purity], 2-methoxyethanol (2ME) [ $(\text{C}_3\text{H}_8\text{O}_2)$ , 99% purity], Monoethanolamine (MEA) [ $(\text{C}_2\text{H}_7\text{NO})$ ] were purchased from Alfa-Aeser. Copper (II) acetate monohydrate (CuAc) [ $(\text{CH}_3\text{COO})_2\text{Cu} \cdot \text{H}_2\text{O}$ , 98% purity], Hydrochloric Acid (HCl), 37% purity], Acetone, 2-propanol (IPA), and Ethanol were purchased from Merk Chemical. FTO-coated glass substrates were used for thin-film coating. DI water was derived from the millipore water system. All the chemicals were used in experiments as purchased without any further purifications.

### **4.2. Methodology**

#### **Solution Preparation**

10 ml of 2-methoxy ethanol was taken as a solvent for each solution with a concentration of 0.1M. NiAc was added accordingly, and the amount of MEA has maintained the ratio of 1.1 with NiAc. For copper doping, 2%, 4% and 6% of CuAc was added to the solution. Stirring the solution for 2 hours at 60°C on the magnetic stirrer it was kept for one day of ageing (Sahoo *et al.*, 2019). The undoped and 2%, 4% and 6% Cu doped NiO thin films are named NiO, 2Cu:NiO, 4Cu:NiO and 6Cu:NiO respectively.

#### **Thin Film Coating**

FTO-coated glass substrates were ultrasonically cleaned with acetone, DI water, ethanol, DI water, IPA, and DI water in sequence for 20 minutes each and dried



in a hot air oven for 2 hours. The thin film was coated using a spin coating unit. The spinning speed was 3000 rpm and the control time was 30 seconds at room temperature. The substrates were dried on the hot plate at 300 °C for 10 minutes. Each thin film was coated with 10 layers of samples and annealed by keeping it in a muffle furnace at 500°C for 1 hour.

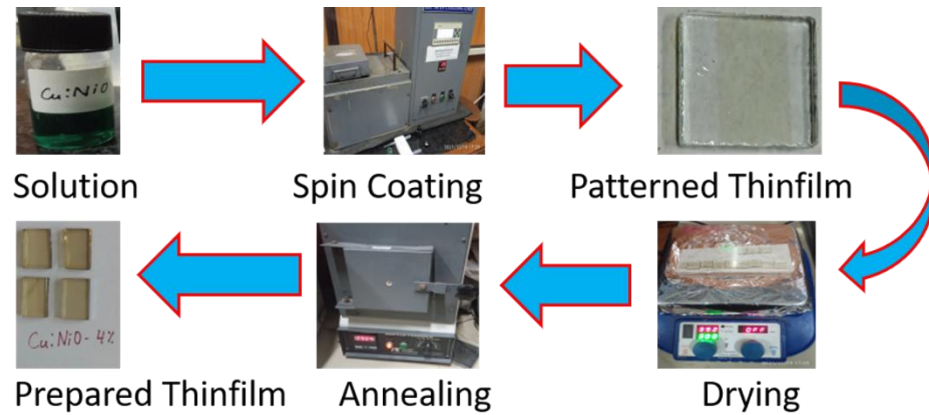


*Fig. 4.1. Different stages of NiO thin film preparation*

### 4.3. Results and Discussions

#### 4.3.1. Structural Properties

The  $2\theta$  peaks at  $37.87^\circ$ ,  $43.62^\circ$  and  $61.62^\circ$  corresponding to (111), (200) and (220) hkl planes respectively are obtained from the GIXRD pattern shown in the fig. 4.2. which is matched with the ICDD card No. 00-004-0835 and confirmed the face-centred cubic structure of the NiO thin film belonging to the Fm-3m (225) space group. The doping of Cu has not disturbed the phase structure as there is no diffraction peaks indicating the Cu. The NiO has a good crystallinity as there is a sharp peak at  $37.8^\circ$ .

Debye-Scherrer's equation (2.7) was employed to calculate the crystalline size of undoped and doped NiO thin films (Cullity, 1978b). Although there were some differences in the lattice parameters, the calculation has been performed by assuming the lattice distortion as constant.

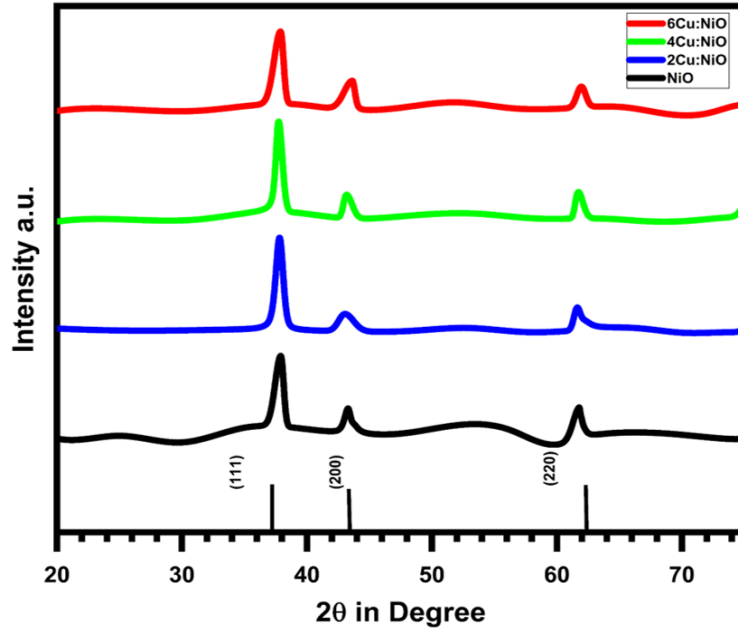


**Fig. 4.2. XRD graph of NiO and Cu doped NiO thin film**

**Table 4.1. The crystal size, lattice strain, lattice parameter, dislocation density and interplannare spacing of undoped and Cu doped NiO from GIXRD**

Samples	$2\theta$ ( $^{\circ}$ )	Grain Size (nm)	$\epsilon$ (lattice strain) $\times 10^{-3}$	a (lattice parameter) in $\text{\AA}$	$\delta$ (dislocation density) $(\text{nm})^{-2}$	d (interplanar spacing) in $\text{\AA}$
NiO	37.88	11.07	3.2670	4.110	8.149	2.372
2Cu:NiO	37.77	12.60	2.8712	4.121	6.294	2.379
4Cu:NiO	37.68	14.63	2.4724	4.131	4.667	2.385
6Cu:NiO	37.87	9.97	36.278	4.111	5.768	2.374

The respective values of different parameters for the  $2\theta$  value of  $37.88^{\circ}$  corresponding to the (111) hkl plane, are tabulated in table 4.1. We observed that the samples are polycrystalline in nature from the analysis. In this work, the crystalline size increases with the Cu doping of 2% and 4% but for the 6% doping again the size

decreases. The decrease in crystallite size may be due to the induced strains and dislocation density thus, resulting in the formation of defect levels as well (Najaa & Eshghi, 2015a). The increase in the amount of Cu doping in NiO thin film can be considered the fact that the interaction of adjacent Cu-Cu ions (L. Zhao *et al.*, 2011). Contrary to our result, Sahoo *et al* have shown that the crystalline size had increased for all Cu-doped samples (Sahoo *et al.*, 2021). The 6Cu:NiO has the lowest strain corresponding to its highest crystalline size compared to all other thin films (Das *et al.*, 2018). Ethiraj *et al.*, also reported a decrease in crystalline size with the increases in Cu doping concentration (Ethiraj *et al.*, 2020). Due to Cu doping, there is a shift in the  $2\theta$  value to the higher angle side of all the samples. The reason behind this can be considered to be the difference in the ionic radius of Ni ions (0.78 Å) and Cu ions (0.82 Å). In NiO, Cu substitutes the site of Ni and expands the lattice, hence also increasing the lattice constant (Emamdoust & Farjami Shayesteh, 2018; He *et al.*, 2017).

#### **4.3.2. Morphological Properties**

FESEM images are used for the morphological study of the Undoped and Cu:NiO samples. The top view of the samples is given below in the fig. 4.3. a) undoped NiO, b) 2Cu:NiO, 3) 4Cu:NiO, 4) 6Cu:NiO respectively. The surface was uniform without any cracks on the substrate. The grains are spherical in shape with particle sizes ranging from 8-15 nm which is matching with the results obtained from XRD data. The average particle size was calculated using ImageJ software. The cross-section view showed the average thickness of the thin films in the range of 570-653 nm.

The EDX was taken along with the FESEM for the confirmation of the elemental composition of the samples. The EDX graphs (fig. 4.4. a, b, c and d) confirmed the presence of Ni, O and Cu in the respective samples. The presence of Sn is also seen in the graph because the sample was coated on the FTO substrate.

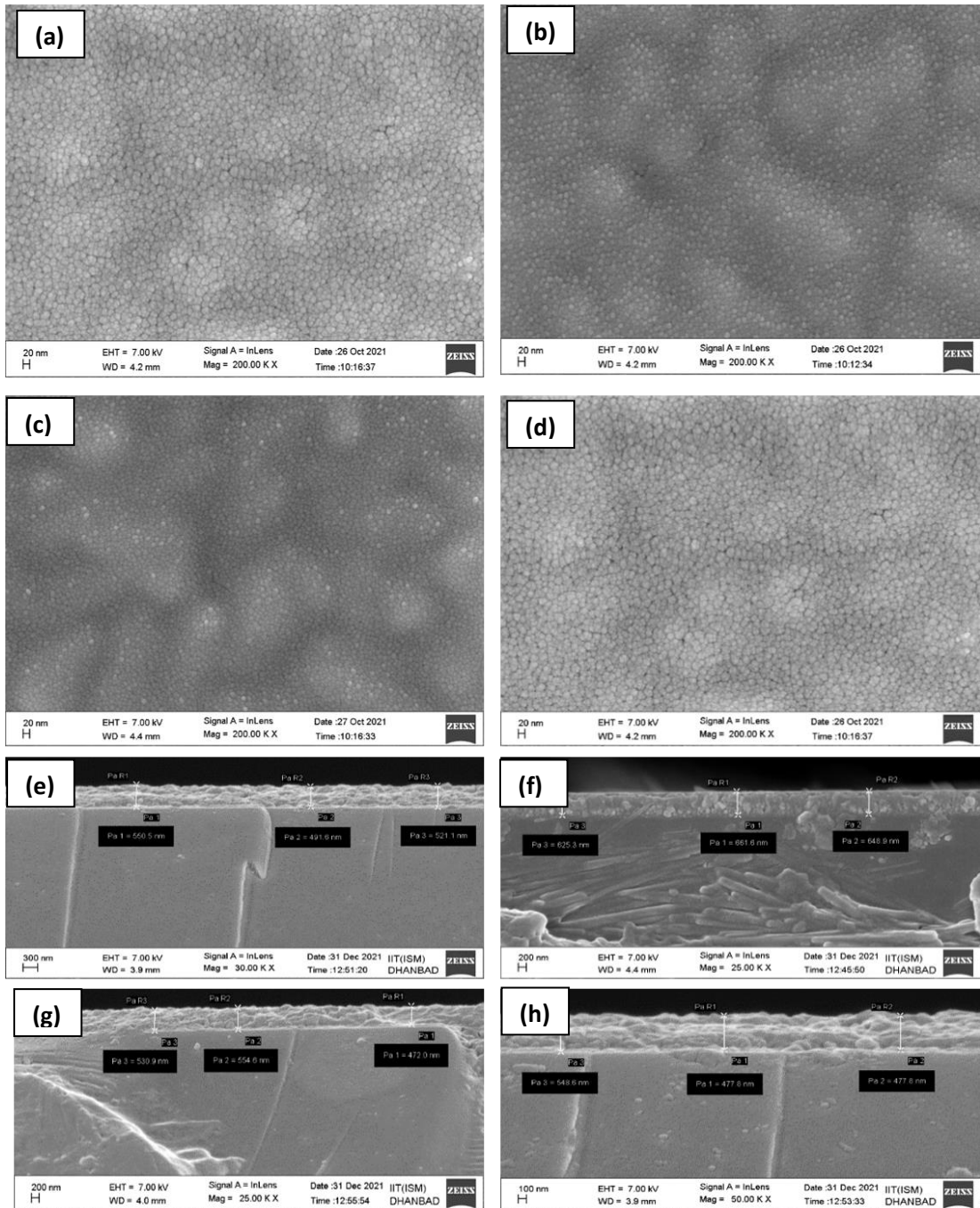


**Fig. 4.3. FESEM and Cross section images of the a) & e) NiO, b) & f) 2Cu:NiO, c) & g) 4Cu:NiO and d) & h) 6Cu:NiO respectively**

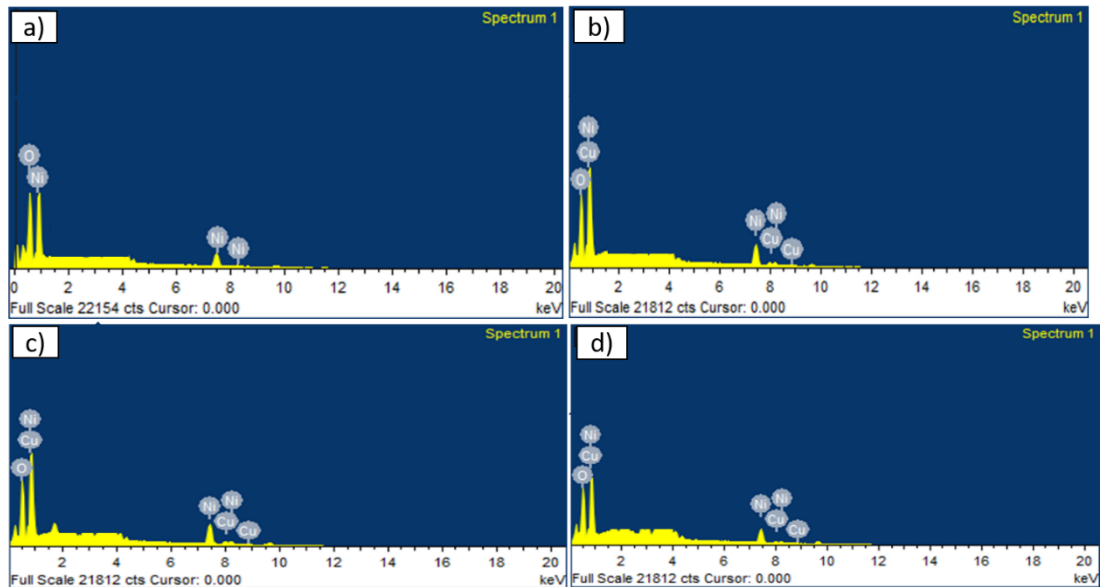


*Fig. 4.4. EDX of a) NiO, b) 2Cu:NiO, c) 4Cu:NiO and d) 6Cu:NiO*

### 4.3.3. Optical Properties

#### Absorbance

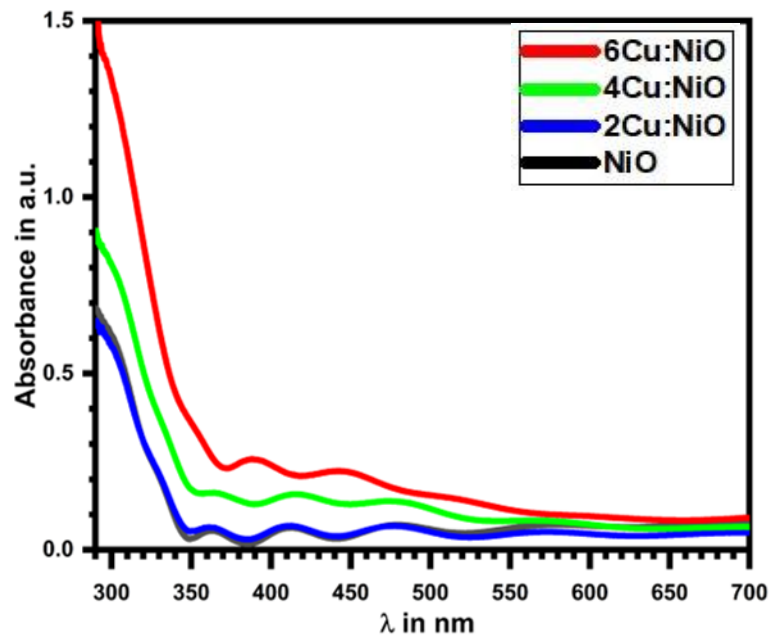


*Fig. 4.5. Absorbance of NiO and Cu doped NiO*

The absorbance for all the samples were taken in visible range for the optical studies are shown in fig. 4.5. All the samples showed the strong absorption in UV region. The doping concentration of Cu increased the absorption which suggest that there is an increase in quality in the crystallinity of the samples (Dawood, 2015). The red shift in the band gap suggests that there is an increase in grain size (Zhang & Zhao, 2019) (Mironova-Ulmane *et al.*, 2019). As a result, it leads to the variation in the band gap (ÇAYIR TAŞDEMİRCİ, 2020). Ashok Reddy *et al* reported the reduction in band gap (Ashok Kumar Reddy *et al.*, 2013).

### Transmittance

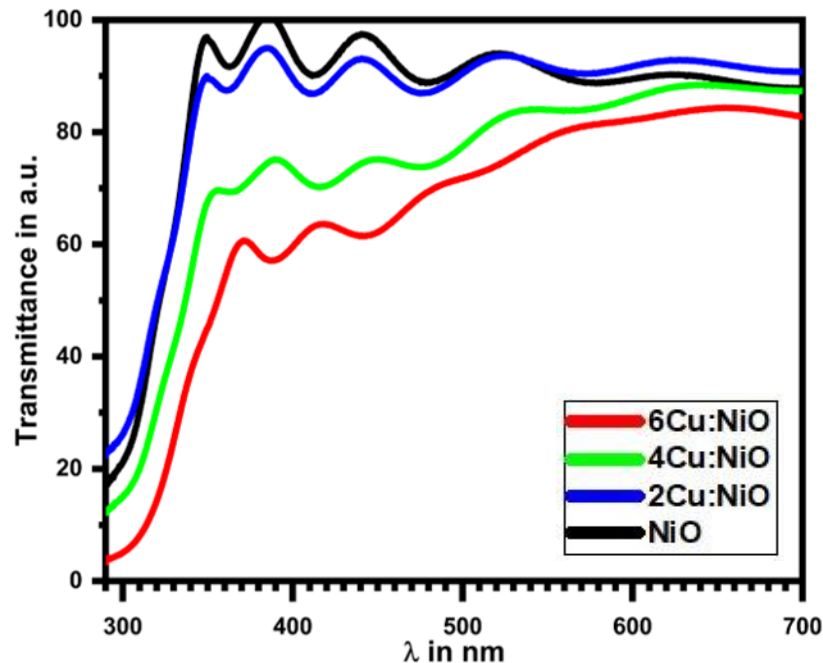


**Fig. 4.6. Transmittance of NiO and Cu doped NiO**

Transmittance plays a very significant role in choosing the HTL for PSCs. Fig. 4.6. shows the transmittance of the undoped and Cu doped NiO samples. The undoped NiO thin film showed the maximum transparency of more than 90%. The transmittance decreased with the increase in doping concentration as the minimum was 60% for 6Cu:NiO. The variation in transmittance can be attributed to the change in crystalline size (Najafi *et al.*, 2018). For the thin film semiconductor, the free charge carrier is most responsible for the light absorption at the long wavelength (Najaa &

Eshghi, 2015b). The irregularity in the transmission curve suggests that the thickness of the samples is not uniform (Manders *et al.*, 2013).

The optical band gap was calculated using Tauc's plot method (Tauc *et al.*, 1966) using equation no 2.7. The energy vs  $(\alpha h\nu)^2$  graph was plotted. We obtained the bandgap values by linear extrapolation of the curve on the energy axis (fig. 4.7). The band gap value is maximum for the undoped NiO thin film and starts decreasing with the doping concentrations. Minimum intrinsic defect in undoped NiO provided the larger bandgap. Band tails formed by Cu impurities and defect levels near the valence band edge are also responsible for the decrease in band gap (Najaa & Eshghi, 2015b). The respective band gaps of the samples are given in table 4.2.

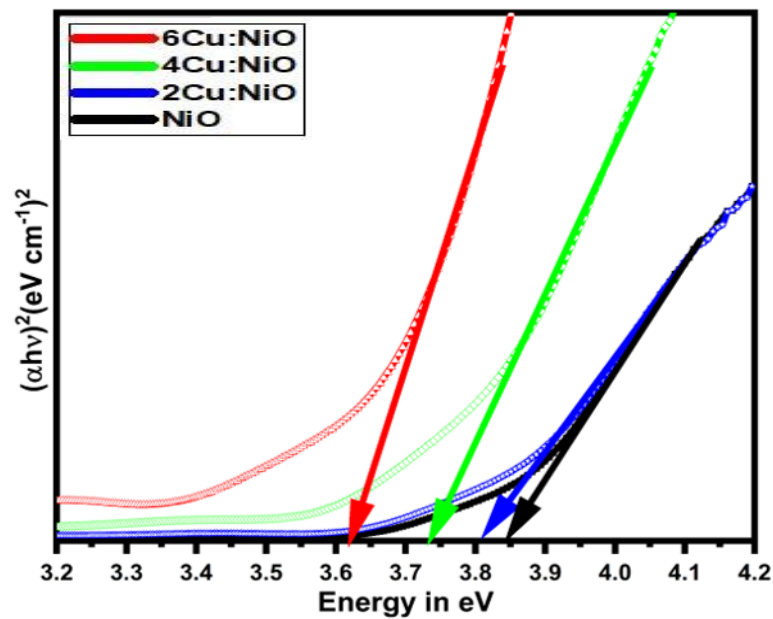


**Fig. 4.7. Band gap of NiO and Cu doped NiO from Tauc's plot**

**Table 4.2. for band edge, bandgap, thickness of undoped and Cu doped NiO**

Samples	Band Edge in nm	Band Gap in eV	Average Thickness nm
NiO	347	3.85	522
2Cu:NiO	348	3.80	520
4Cu:NiO	353	3.74	518
6Cu:NiO	370	3.62	513

### **Photoluminescence**

The room temperature PL spectra of the undoped NiO and Cu:NiO thin films is represented in fig. 4.8. The 325 nm laser was used as the excitation wavelength. Mainly the PL emission is understood in two categories as near band edge (NBE) UV emission and deep level (DL) in the visible region which is related to defects. The exciton-exciton scattering leads to the direct recombination of excitons and causes UV emission. The electron occupying the vacancy of oxygen and the photo-generated hole causes radiative recombination and originates the visible emission (Kumari *et al.*, 2009). The strong band-band PL emission peak at 390 nm indicates higher crystallinity and larger particle size (Y. A. K. Reddy *et al.*, 2013). The recombination rate of photon-induced E-H pair increases with higher band-band PL intensity. The peaks at 511 nm and 708 nm correspond to the slight change in stoichiometry, the interstitial oxygen trapping within the lattice or cation vacancy of NiO thin film leading to the defects. The charge transfer between Ni<sup>2+</sup> and Ni<sup>3+</sup> can also generate vacancies in NiO thin films (Liang *et al.*, 2014). The two shoulder peaks in the green emission region can be attributed to the presence of said defects in the NiO lattice (Y. A. K. Reddy *et al.*, 2013). The peak 390 lies in the blue emission region which confirms the Cu doping in NiO. Increasing the doping concentration, the PL intensity is decreasing which can be due to the increment in the particle size (B. R. Reddy *et al.*, 2014).



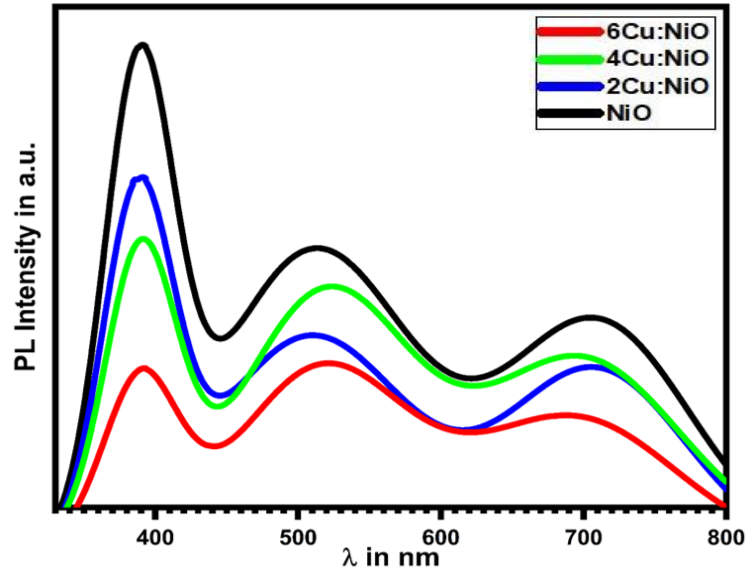


**Fig. 4.8. PL graph of NiO and Cu doped NiO thin films**

#### **4.3.4. Electrical Properties**

Photo Current Density (J) of the Cu doped and undoped samples were taken under Dark conditions, Visible, Ultraviolet and Infrared light within the voltage range of -0.4 to +0.4 V. The different samples showed various J-V properties. As the doping concentration increased, the J also increased corresponding to the applied voltage V. Again, among the various illuminations, the maximum J-V value was observed by the samples which were under the IR illumination. In all the cases the J at dark was low followed by the visible light and J increased under UV light and reached a maximum under the IR. So, Cu-doping increases the electrical conductivity and with this, the different types of illumination also influence the conductivity of the samples (Sahoo *et al.*, 2021). The conductivity is influenced by the movement of hole which can be understood by visualization of the conversion of two  $\text{Ni}^{+2}$  ions into  $\text{Ni}^{+3}$  to each Ni vacancy site. During the conversion of  $\text{Ni}^{+3}$  it is not stable and changes to another site from one  $\text{Ni}^{+2}$  site. Suitable methods of appropriate doping for substitutional doping help to achieve optimum conductivity (Bashir *et al.*, 2019). The carrier concentration was calculated from the Hall measurement and found to be  $1.246 \times 10^{20}$ ,  $3.341 \times 10^{20}$ ,  $6.112 \times 10^{20}$  and  $4.231 \times 10^{20} \text{ cm}^{-3}$  for NiO, 2Cu:NiO, 4Cu:NiO and 6Cu:NiO respectively.

**Table 4.3. The maximum J-values of Undoped and Cu-doped NiO under different illumination**

Samples	Dark Condition	Visible Light	U-V Light	IR light
	Maximum J (mA-cm <sup>-2</sup> )			
NiO	0.6x10 <sup>-3</sup>	0.7 x10 <sup>-3</sup>	1.3 x10 <sup>-3</sup>	1.4 x10 <sup>-3</sup>
2Cu:NiO	0.5 x10 <sup>-3</sup>	1.2 x10 <sup>-3</sup>	1.0 x10 <sup>-3</sup>	1.4 x10 <sup>-3</sup>
4Cu:NiO	0.5 x10 <sup>-3</sup>	0.6 x10 <sup>-3</sup>	1.7 x10 <sup>-3</sup>	2.6 x10 <sup>-3</sup>
6Cu:NiO	2.2 x10 <sup>-3</sup>	2.3 x10 <sup>-3</sup>	2.6 x10 <sup>-3</sup>	2.8 x10 <sup>-3</sup>

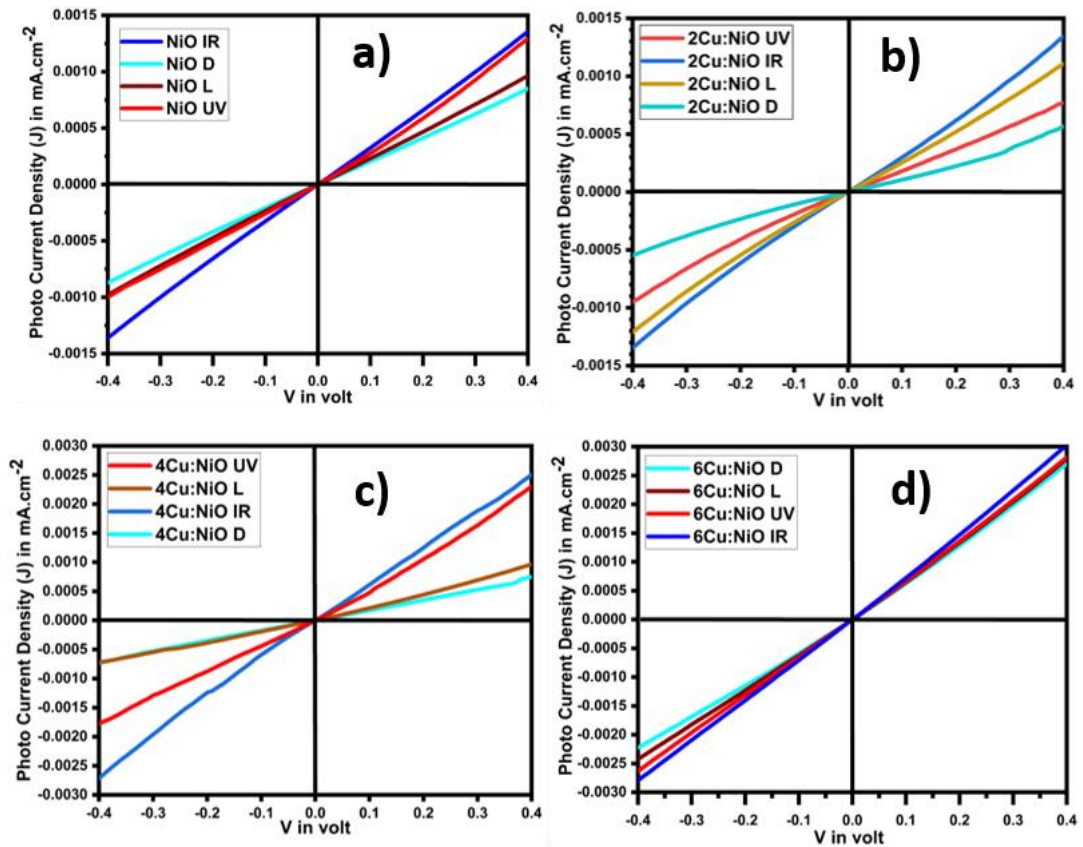


**Fig. 4.9. J-V characteristics of a) NiO, b) 2Cu:NiO, c) 4Cu:NiO and d) 6Cu:NiO under the dark, light, UV and IR illumination**

#### 4.3.5. XPS measurement

XPS measurement was carried out for the analysis of the oxidation states of the samples. It also confirms the chemical composition of the samples. The high-resolution Ni 2p XPS spectra of undoped and Cu-doped NiO thin films are presented in fig. 4.10. (c & d). The Ni<sup>+2</sup> standard Ni-O octahedral bonding in cubic NiO is confirmed by the peak situated at 852.70 eV (Sato *et al.*, 2016b). The Ni<sup>+3</sup> ion or nickel hydroxides are induced by Ni<sup>+2</sup> vacancy depicted at the 854.4 eV peaks. The broad peak located at 860 eV represents the shake-up process in the NiO structure (S. H. Wang *et al.*, 2019). Among the four consequent peaks at 852 eV, 854 eV, 860 eV, and 870 eV respectively, the presence of the first two peaks Ni<sup>+2</sup> and Ni<sup>+3</sup> corresponds to Ni 2p<sub>3/2</sub> (B. Zhao *et al.*, 2009). The peaks at 860 eV and 878 eV confirm the co-existence of Ni<sup>+2</sup> and Ni<sup>+3</sup>. Ni 2p<sub>1/2</sub> is represented by the peak at 860 eV (Sahoo *et al.*, 2021).

Fig. 4.10. (a & b) represents the O 1s XPS spectra. There are two distinct peaks located at 528 eV and 530 eV which indicates the lattice oxygen (O- Ni<sup>+2</sup>) and metal deficient induced dangling oxygen (O- Ni<sup>+3</sup>) (M. Feng *et al.*, 2020b).

Fig. 4.10. (e & f) show XPS spectra of Cu 2p which confirms the incorporation of Cu<sup>2+</sup> successfully into the NiO lattice. two shake-up satellite peaks at 940 eV and 961 eV and two main peaks at 932 eV and 952 eV are present. The evidence of the replacement of Ni<sup>+2</sup> in NiO lattice in its divalent state is given by the peaks located at 932 eV and 952 eV, which corresponds to Cu 2p<sub>3/2</sub> and Cu 2p<sub>1/2</sub> respectively (Li *et al.*, 2017b; Martin *et al.*, 2013).

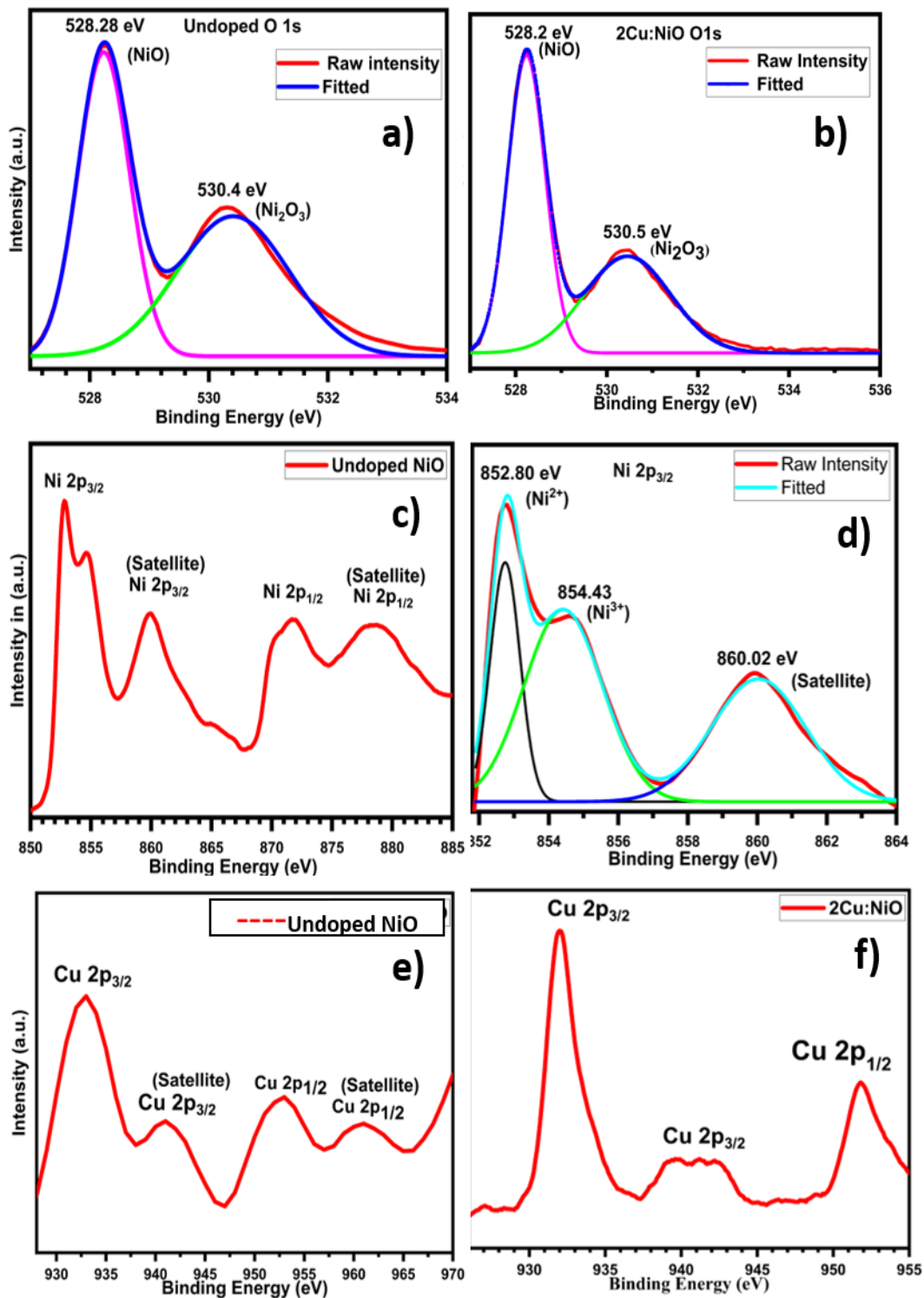


*Fig. 4.10. O 1s states of a) Undoped and b) Cu:NiO, Ni 2p XPS Spectra of c) undoped NiO and d) Cu doped NiO Ni 2p<sub>3/2</sub> XPS spectra e) undoped NiO and f) Cu doped NiO*

#### **4.4. Conclusion**

Thin films of NiO and Cu doped NiO with different molar percentages were synthesized successfully by simple and low-cost spin coating method. The band gap was affected by Cu doping and was found to decrease with the increasing doping concentration. The doping concentration also influenced the electrical property of the NiO thin films as the J-value increased with the increase in the Cu doping concentration. The structural property was also affected by the doping and there was change in size of the crystal with the change in doping concentration. The observed optical and electrical properties of the NiO and Cu doped NiO thin films in this work suggests that the NiO thin film can be employed as HTL in PSCs as a good candidate. The Cu-doping may have a good effect in increasing the PCE of the PSCs.

## CHAPTER 5

### SYNTHESIS AND CHARACTERIZATION OF PEROVSKITE LAYERS, COMPLETE DEVICE FABRICATION OF PSCS

#### INTRODUCTION

The limitation in an increase in the efficiency of Si-based solar cells was overcome by the Pb-based solar cells. The toxicity of lead did not permit for the largescale commercialization and the need for the replacement of the Pb is seen to be urgent. The Pb was almost replaced by Sn with a higher efficiency of up to 33.41% even though stability remains the problem (Fatema & Arefin, 2022). For stable perovskite, the alternative to Sn-based a very unstable perovskite, researchers started concentrating on the stable double perovskite. Shifting from single perovskite to double perovskite effort has been made to retain the 3D structure of perovskite as intact, combination of monovalent and trivalent cation was applied in ordered B-site within  $ABX_3$  replacing the  $Pb^{2+}$  forming the double perovskite with the formula  $A_2B^3+B^+X_6$ .  $Cu^+$ ,  $Ag^+$ ,  $Bi^{3+}$ ,  $Ab^{3+}$  and  $In^{3+}$  are some of the combinations of +1 and +3 ions having suitable electronic configurations. They are stable in ambient conditions. The theoretical and experimental possibility of the synthesis of double perovskites had also been done by Volonakis and others (Volonakis *et al.*, 2016). Fu synthesized  $Cs_2AgBiCl_6$  and showed good stability in ambient conditions. The bandgap was found between 2.3-2.5 eV. He suggested that tuning the band gap will facilitate more photovoltaic applications (Fu, 2019). Filip *et al.*, (2016) studied the electronic properties of  $Cs_2AgBiBr_6$  experimentally and theoretically (Filip *et al.*, 2016). Gruel *et al.*, (2017) did extraordinary work by synthesizing the DP by solution method and preparing a thin film by spin coating on the pre-heated substrate followed by the annealing. The observed PCE was 2% (Greul *et al.*, 2017). The DP materials are in the infancy stage of research. These materials seem to be promising for future alternatives to solar cell candidates. The DPs also possess some defects. The stability of the cell is quite good in comparison to Sn-based cells, and more studies had been done to improve the stability (Wu *et al.*, 2018). The performance of the cell was also affected by hysteresis. Pantaler *et al.*, (2018) employed multi-step method for synthesis of the

Perovskite layer making it very compact over the mesoporous TiO<sub>2</sub> Oxide (Pantaler *et al.*, n.d., 2018). Previously used HTL spiro-OMeTAD was replaced by PTTA and obtained a PCE of 1.26% without hysteresis (Fu, 2019). Gao *et al.*, (2018) applied an inverted planar structure, with improved smooth morphology using anti-solvent dropping and annealing got a PEC of 2.23% (Gao *et al.*, 2018). The work on Cs<sub>2</sub>AgBiBr<sub>6</sub> has been already mentioned earlier. The comparative study has been represented in table 5.1.

In this work, we have synthesized Cs<sub>2</sub>AgBiBr<sub>6</sub> as double perovskites from the solution method. The ETL (ZnO np) is the same for all the devices but the HTL, NiO is doped with Cu with varied molar concentrations for observing the doping effect on the PEC of the prepared PSC device.

## **5. Experimental**

### **5.1. Materials**

BiBr<sub>3</sub> ( $\geq 98\%$ ), DMSO anhydrous (99.9%), AgBr (99.999%), CsBr (99.999%), H<sub>3</sub>PO<sub>2</sub>, FTO (2.3mm,  $\sim 7\text{ohm/sq.cm}$ ) substrate, were purchased from Sigma Aldrich and Filter paper, ethanol, Zinc dust, HCl were purchased from Hi-media. These chemicals were used as purchased without any further purification.

### **5.2. Methodology**

#### **Synthesis of Cs<sub>2</sub>AgBiBr<sub>6</sub>**

At first 268 mg of BiBr<sub>3</sub>, 254 mg of CsBr and 112.8 mg of AgBr were dissolved in dimethyl sulfoxide (1 mL, DMSO, anhydrous). It took a few minutes to dissolve completely and once the solution got ready, both substrates and the precursor solution were preheated to 75 °C prior to the spin coating. 100  $\mu\text{L}$  of the solution was spin-coated above the HTL layer at 2000 rpm for 30 s. The sample was then kept for annealing at the optimum temperature of 285 °C for 5 min under normal condition. In this way the formation of desired perovskite took place.



*Fig. 5.1.  $Cs_2AgBiBr_6$  Solution*

### **5.3. Results and discussions**

#### **5.3.1. Structural properties**

Fig. 5.2. show the XRD pattern of the A)  $Cs_2AgBiBr_6$ . The planes corresponding to diffraction peaks are indexed as (111), (200), (220), (222), (400), (422) and (440) which confirms the cubic crystalline structure of  $Cs_2AgBiBr_6$  when matched with the ICDD card no. 01-084-8698. No other peaks are present in the graph indicates that the purity of the sample. It belongs to the  $Fm-3m$  (225) space group.



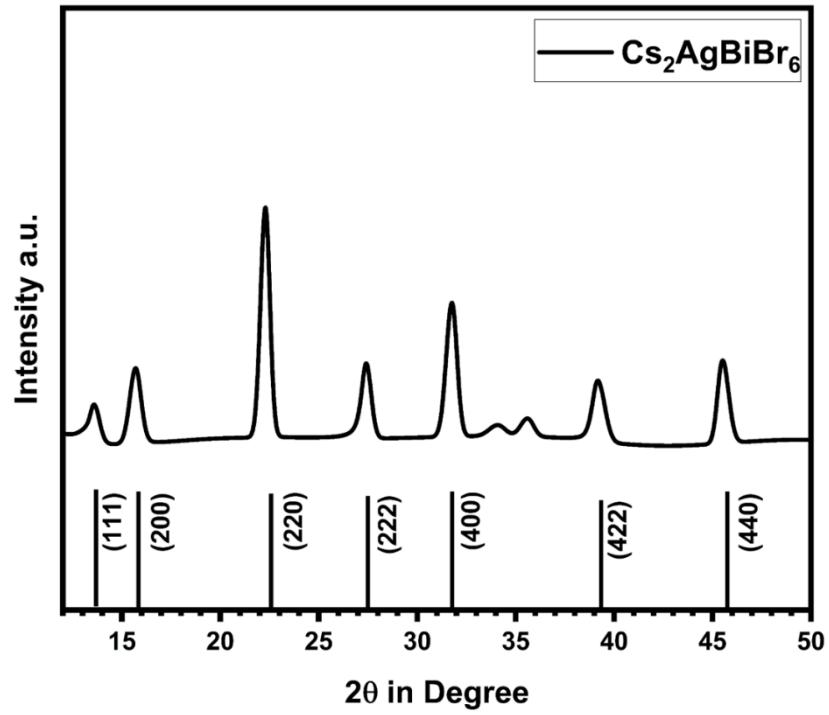


*Fig. 5.2. XRD graph of  $\text{Cs}_2\text{AgBiBr}_6$*

### 5.3.2. Optical properties

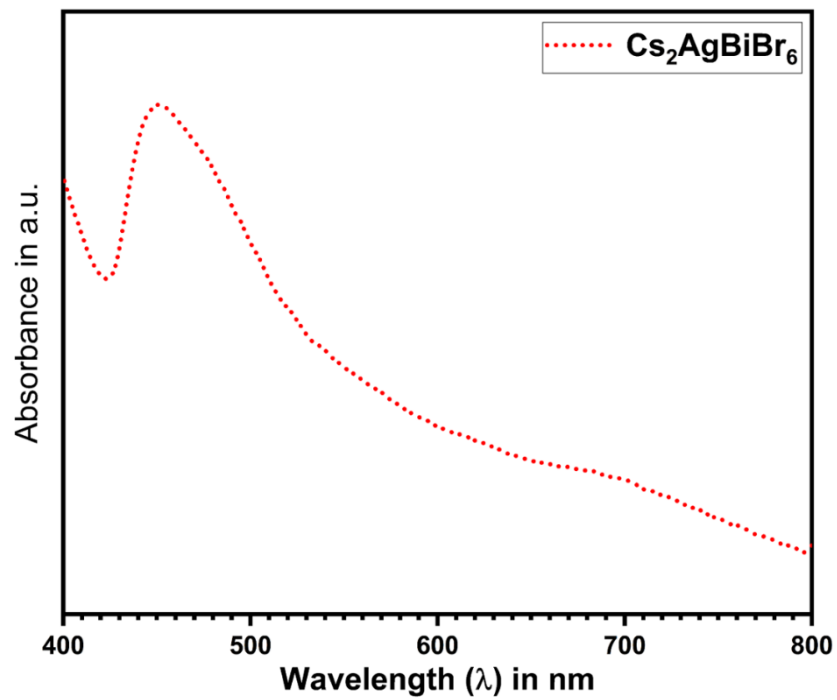


*Fig. 5.3. Absorbance of  $\text{Cs}_2\text{AgBiBr}_6$*

Optical properties are a very essential part in the study of solar cell materials. The absorbance of  $\text{Cs}_2\text{AgBiBr}_6$  is presented in fig. 5.3. The optical band gaps were calculated using Tauc's plot method (fig. 5.4.) and found to be 2.18 eV for  $\text{Cs}_2\text{BiAgBr}_6$ . This result matches with some of the reported values (Volonakis *et al.*, 2017). Although there are many discrepancies in the band gap values, it has been suggested that the different methods employed for the synthesis of double perovskite might have led to the various values of the band gap (Filip *et al.*, 2016). Band gap tuning is also a very good way to device optimization and increasing device efficiency.

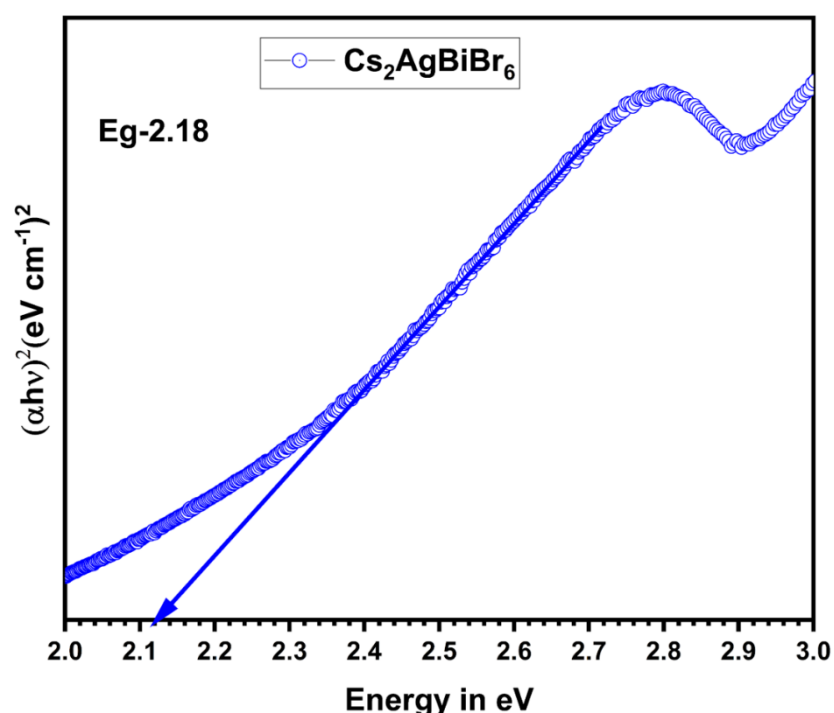


*Fig. 5.4. Tauc's Plot showing the band gap of  $\text{Cs}_2\text{AgBiBr}_6$*

### 5.3.3. Morphological Properties

#### FESEM and EDX

The surface morphology is studied with the help of FESEM images. Fig. 5.5. shows the surface image of  $\text{Cs}_2\text{AgBiBr}_6$ . The crystalline structure is formed uniformly without any cracks. The elemental composition was also studied with the help of the EDX graph. The presence of Cs, Ag, Bi and Br are clearly shown in the graph (fig. 5.6).

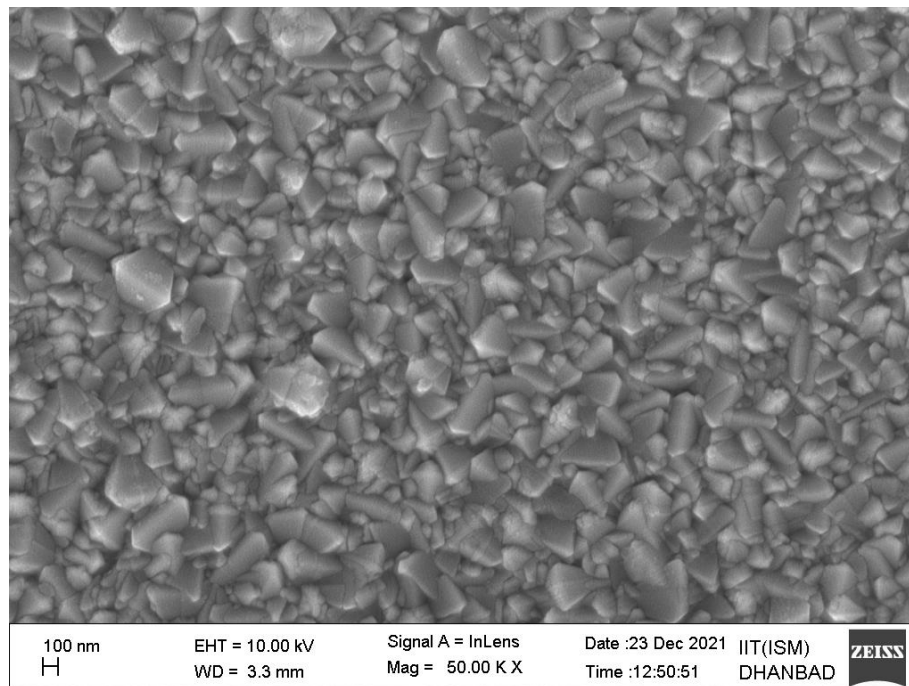


**Fig. 5.5 FESEM image of  $Cs_2AgBiBr_6$**

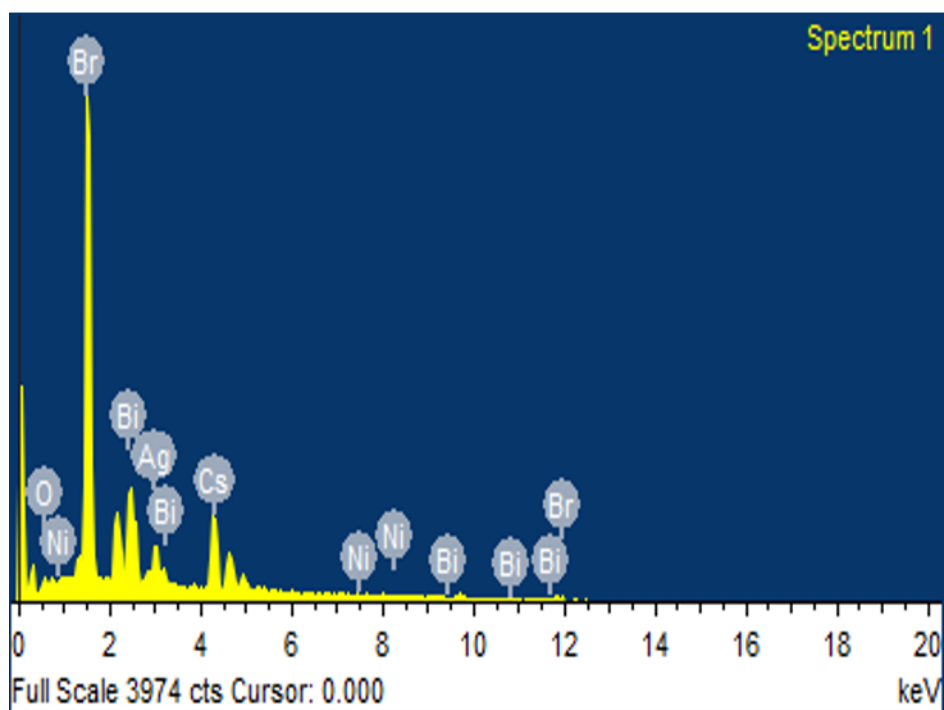


**Fig. 5.6. EDX graph of  $Cs_2AgBiBr_6$**

#### 5.4. Device Fabrication

The FTO substrates were patterned by applying Zinc dust and HCl (3 M) for 5 minutes on masked FTO and then washed ultrasonically in DI water, Acetone DI water and IPA for 15 minutes each. The cleaned glass substrates were dried at 90<sup>0</sup> C for 2 h. For preparing PSCs, four substrates were coated with NiO, 2Cu:NiO, 4Cu:NiO and 6Cu:NiO for the purpose of HTL.

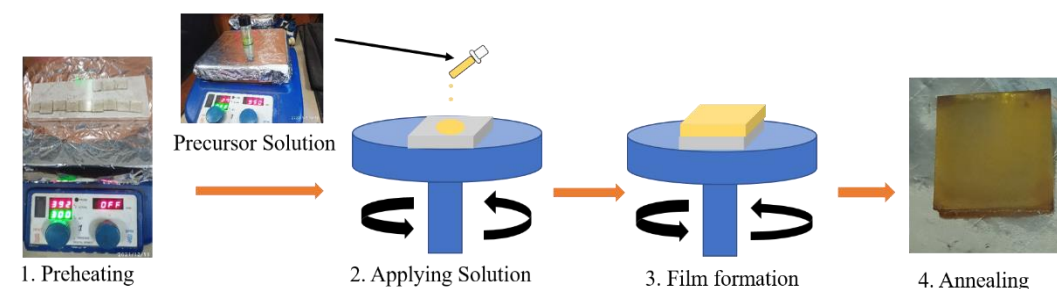


*Fig. 5.7. Synthesis of Perovskite layer*

These NiO and Cu:NiO coated substrates were coated with Cs<sub>2</sub>AgBiBr<sub>6</sub>. Then DP was coated above those HTL. After that, all the sets of devices were coated with the ZnO np above the Perovskite layer and dried. At last, the silver paste was applied above the ZnO layer in a patterned way for making the Ohmic contact as an electrode. There were four devices prepared in p-i-n structure, namely

- a) **FTO/NiO/Cs<sub>2</sub>AgBiBr<sub>6</sub>/ZnO np/Ag**
- b) **FTO/2Cu:NiO/Cs<sub>2</sub>AgBiBr<sub>6</sub>/ZnO np/Ag**
- c) **FTO/4Cu:NiO/Cs<sub>2</sub>AgBiBr<sub>6</sub>/ZnO np/Ag**
- d) **FTO/6Cu:NiO/Cs<sub>2</sub>AgBiBr<sub>6</sub>/ZnO np/Ag**

The graphical abstract of the designed devices has been shown in fig. 5.8. Fig. 5.9. shows the patterned FTO substrates prepared by using masking tape. Fig. 5.10. shows the solar simulator used in our work and fig. 5.11. is the complete PSC device from the top view. The brown line on the top is the Ag layer for ohmic contact.

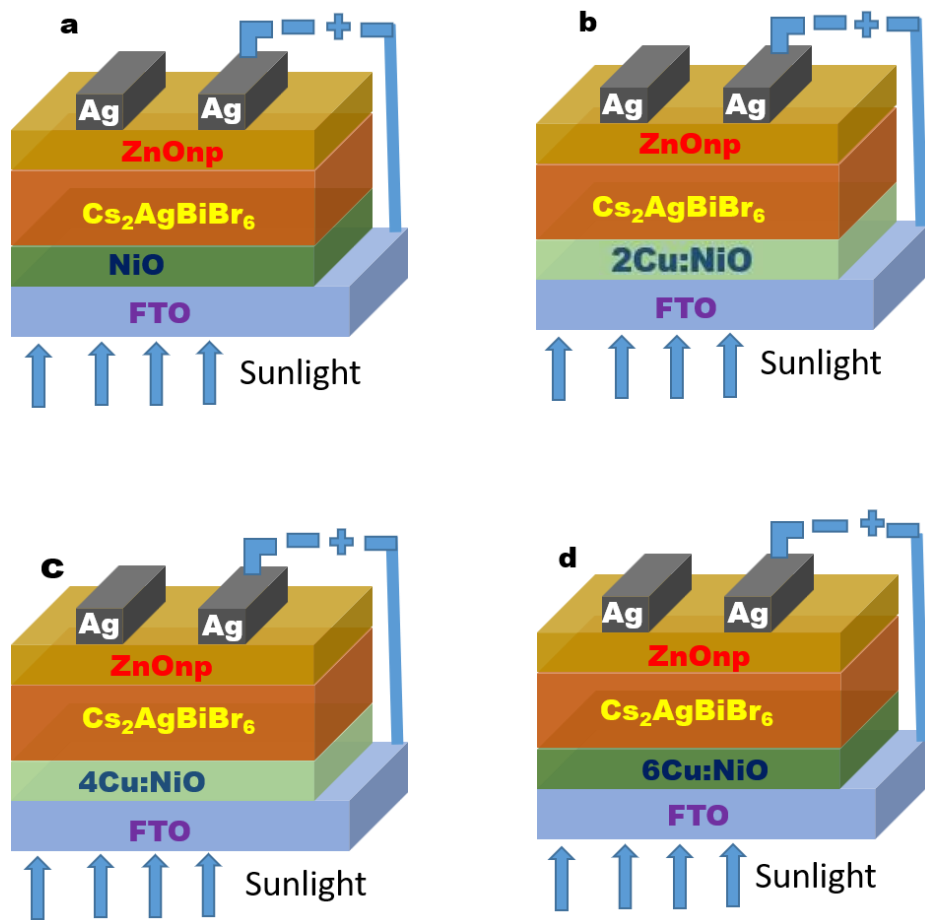


*Fig. 5.8. PSC p-i-n device architecture a) NiO/Cs<sub>2</sub>AgBiBr<sub>6</sub>/ZnO, b) 2Cu:NiO/Cs<sub>2</sub>AgBiBr<sub>6</sub>/ZnO, c) 4Cu:NiO/Cs<sub>2</sub>AgBiBr<sub>6</sub>/ZnO and d) 6Cu:NiO/Cs<sub>2</sub>AgBiBr<sub>6</sub>/ZnO*



*Fig. 5.9. Patterned FTO glass (ZnO dust and HCl)*

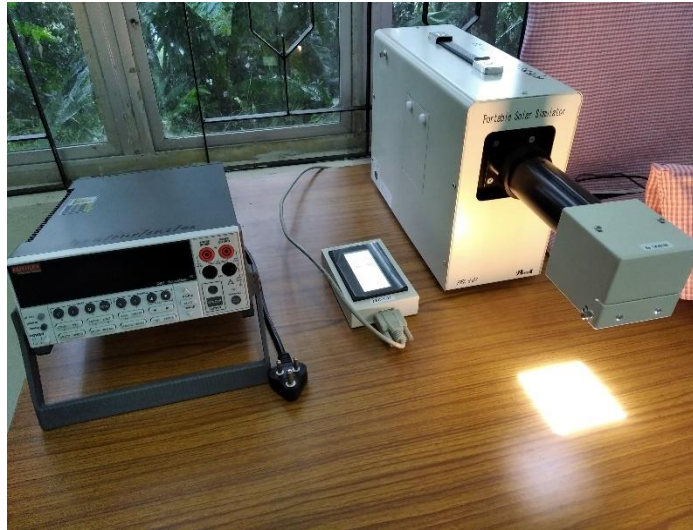


*Fig. 5.10. Solar Simulator*



*Fig. 5.11. Prepared PSCs*

## 5.5. Electrical properties and PCE calculation

The prepared devices were measured in an ambient condition using a portable Solar Simulator from Peccell Technology, model PEC -L01 with class AAA (uniformity  $\leq \pm 2\%$ ). It was calibrated with the NREL-standard Silicon-based reference cell to provide simulated AM 1.5 sunlight with an irradiance of  $100 \text{ mW cm}^{-2}$  (1 sun). Keithley 2401 source meter was used to measure the current-voltage characteristics of the prepared devices.

Four probe was connected with a golden 3M pin to connect with the electrodes of the devices. The graphs obtained from the measurement were analysed using the Peccell IV curve analyser Software attached along with the solar simulator. The results obtained from the graph is tabulated in the table 5.1.

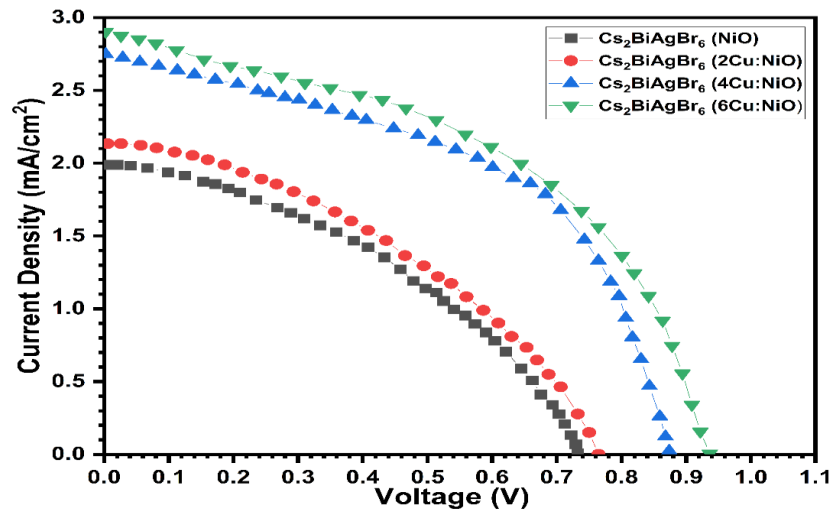


*Fig. 5.12. J-V characteristics of PSCs*

For the measurement of PCE, the important components to be taken care of are  $I_{sc}$ ,  $V_{oc}$ ,  $I_m$ ,  $V_m$  and FF.  $I_{sc}$  is short-circuit current also known as photocurrent, measured when the solar cell is not connected to any other circuit,  $V_{oc}$  is open circuit voltage, measured when the solar cell is not connected to any external circuit.  $I_m$  and  $V_m$  is the maximum current and the maximum voltage produced by the solar cell when the circuit is closed. The maximum power is given by

$$P_{max} = V_m I_m \quad \dots 5.1.$$

The FF fill factor is the ratio of power generated to the power of the incident photon. The value of FF varies from 0-1. A value nearer to 1 is considered to be good. The expression for FF is given below.

$$FF = \frac{V_m * I_m}{V_{oc} * I_{sc}} \quad \dots 5.2.$$

The Power Conversion Efficiency of the PSCs can be calculated using the below equation.

$$PCE = \frac{P_{generated}}{P_{photon}} = \frac{V_{oc} * FF}{P_{photon}} \quad \dots 5.3.$$

**Table 5.1. Voc, Isc, FF and PEC of the prepared PSC devices**

		Voc	Isc	FF	PEC (%)
a)	<b>FTO/NiO/Cs<sub>2</sub>AgBiBr<sub>6</sub>/ZnO np/Ag</b>	0.73	2.0	0.38	0.56
b)	<b>FTO/2Cu:NiO/Cs<sub>2</sub>AgBiBr<sub>6</sub>/ZnO np/Ag</b>	0.76	2.13	0.38	0.62
c)	<b>FTO/4Cu:NiO/Cs<sub>2</sub>AgBiBr<sub>6</sub>/ZnO np/Ag</b>	0.87	2.74	0.49	1.18
d)	<b>FTO/6Cu:NiO/Cs<sub>2</sub>AgBiBr<sub>6</sub>/ZnO np/Ag</b>	0.93	2.9	0.46	1.24

## 5.6. Conclusion.

Lead-free double perovskite Cs<sub>2</sub>AgBiBr<sub>6</sub> were synthesized in ambient condition successfully and its structure was confirmed by the XRD data. The uniformity of the perovskite layer was analysed with the help of FESEM images and its elemental composition was confirmed by EDX graph. Four PSCs based on Pb-free based double perovskites, p-i-n configured were fabricated with NiO and Cu doped NiO as HTL with ZnO np is common ETL for all the PSC devices. The highest efficiency was achieved by the FTO/6Cu:NiO/Cs<sub>2</sub>AgBiBr<sub>6</sub>/ZnO np/Ag PSC of 1.24%. The successful fabrication of Pb-free PSCs makes DPs a promising candidate for solar cells.



## CHAPTER 6

### SUMMARY AND CONCLUSION

The motive of this work is to synthesize and characterize the lead-free perovskite for photovoltaic application. The demand for renewable sources of energy is very high. So, the alternative to conventional sources of energy is in the pathway of research. Si-based solar cells reached the highest limit, so more efficiency cannot be achieved further. The efficiency of Si-based solar cells is exceeded by the Pb-based Perovskite Solar Cells. The toxicity of the Pb forbid the commercialization of Pb-based Solar Cells. Pb was replaced mainly by Sn and achieved a comparable high efficiency, but the stability of Sn created the problem. The Sn-based PSCs were very unstable. So, the stable, highly efficient and low-cost PSC is in demand.

The research is going on many types of perovskite materials. Although all the pristine perovskite materials are not applicable in the photovoltaic application, their band gap is tuned by doping with other elements to be used in photovoltaic applications. Many reports have shown that band gap tailoring has also increased the efficiency of the PSCs. The efficiency of the PSCs is influenced by many factors like charge transportation, interface mismatch, the thickness of the layer, synthesis route, drying and annealing temperature, environmental conditions, HTL, ETL, precursor materials and more.

It is difficult to predict exactly at the initial stage of research the effects of the above factors on the efficiency of the PSC. All the factors act at the same time and the exact effect cannot be understood at the very first stage. For understanding the effects of various factors on the efficiency of the PSCs, different types of properties are studied under different conditions.

In this work, simple FTO/HTL/Perovskite/ETL/Ag architecture following the p-i-n structure of the PSC was employed. For ETL, ZnO np were used for all the devices. The HTL is different for all four devices. NiO thin film had been employed as HTL with 2, 4 and 6 molar percentages of Cu doping. The improvement in efficiency due to various HTL and ETL have been reported widely. Even the doping into the ETL and HTL materials has also influenced the efficiency. In this work also,

the efficiency was affected by the Cu doping concentration into the NiO HTL. Doping of Cu into NiO influenced the carrier concentration resulting in a change in the efficiency of the PSCs.

In chapter 1, the introduction to the perovskite material, its historical advancement and its very fast improvement in PCE has been elaborated. The trend in the change of perovskite material from Pb, Sn to the inorganic double perovskite has been briefed.

In chapter 2, the details of the instruments used for characterization are given. The pictorial presentation helps to understand the components and workings of the instrument. Although it is very vast to go into in-depth knowledge of each of the instrument and characterization techniques, the basics of all the techniques required for this work have been tried to accommodate in a very short.

In Chapter 3, the synthesis and characterization of ZnO np and ZnO nr are given. There are many routes for the synthesis of ZnO np. In this work, a solution-based method using TMAH has been used. ZnO nr are grown hydrothermally on the ZnO thin film. The use of ZnO np and ZnO nr have affected the efficiency of the PSCs when used as the ETL. The purpose of the synthesis of ZnO nr and ZnO np is to employ them into the PSC as ETL. The ZnO np was easily dispersed above the perovskite layer as ETL in p-i-n structure but the ZnO nr could not be grown above the perovskite layer due to which ZnO nr were not employed as ETL in our work. The optical, structural, morphological and electrical properties of the ZnO were studied in this chapter.

In Chapter 4, NiO Thin film was synthesized with 2, 4 and 6 molar % of Cu doping. The effect of doping on various properties has been studied by applying different characterization methods. The use of NiO as HTL has a positive influence on the efficiency of the PSC.

In Chapter 5, the synthesis of Pb-free double perovskite  $\text{Cs}_2\text{AgBiBr}_6$  was done. A confirmational report on its optical, morphological, and structural properties has been given in this chapter. The complete device fabrication with p-i-n structure with a

different doping concentration of Cu into NiO as HTL and fixed ZnO as ETL has been studied. The overall PCE is also calculated in this chapter.

### **Major Outcomes of the research**

- 1) The sol-gel-spin-coating method is useful in the synthesis of ZnO np, ZnO nr and NiO and perovskite thin films. This method is low-cost and very facile though the exact thickness control is difficult.
- 2) The structural property was studied with GIXRD, for all the synthesized material. It confirmed the crystal structure of the ZnO, NiO and perovskite. The Cu doping into NiO has shifted the 2 theta peaks and had an effect on the crystal size also. With the increase in doping concentration, the size had increased to 4% but decreased with 6% doping.
- 3) The optical property was studied with UV-vis spectroscopy and PL spectroscopy. The absorbance and the transmittance were affected by the Cu doping into NiO. The effect of the increase in crystal size was observed in the red shift of the band gap. Transmittance was decreased with the Cu doping in NiO thin film and there was a decrease in the band gap also. So, the doping of Cu into NiO can tune the band gap. The defect states were also studied with PL. The PL intensity decreased with the increase in Cu doping concentration which was due to the increment in the particle size.
- 4) The electrical properties were studied under different illumination for ZnO and NiO-based thin films and a solar simulator was used for the study of current-voltage characteristics for PCE calculation of the prepared device. The sample was kept under dark, UV, Visible and IR lamps. The highest doping concentration under IR showed the maximum I-V behaviour. So, Cu doping has a good effect on electrical conductivity. The Hall measurement also showed an increase in carrier concentration with the increase in doping concentration.
- 5) The FESEM images were studied to understand the surface morphology of the prepared thin films. Using ImageJ software, the particle sizes were also

calculated which can be compared with the crystal size calculated from the XRD. Most of all the films had smooth and uniform surface morphology. Although it is difficult to obtain high quality films from the spin coating device, the film was optimum.

- 6) The XPS and EDX graphs were mainly used for the confirmation of the elemental composition of the prepared thin films. A little study from the XPS graph is done for the Cu doping into the NiO thin films and confirmed the Cu doping as well.
- 7) At the end the complete device was characterized with I-V measurement and found increased PCE with the increased in Cu doping concentration. So, the highest PCE of 1.24% was observed with the 6Cu:NiO device.

### **Future works**

This work only shows the possibility of device fabrication with the materials used. Now further improvement to increase the PCE of the Pb-free PSC can be extended in future works by the following methods.

- ◆ Different parameters can be changed.
- ◆ The synthesis methods can be improved.
- ◆ The effect of doping on ETL also can be studied.
- ◆ The HTL and ETL materials can also be replaced.
- ◆ The band gap of the Perovskite can be tuned by doping.

## REFERENCES

- Aftab, M., Butt, M. Z., Ali, D., Aftab, Z. H., Tanveer, M. U., & Fayyaz, B. (2022). Investigation of antifungal response of NiO and copper-doped NiO thin films against *Aspergillus niger* and *Macrophomina phaseolina* fungi. *Environmental Science and Pollution Research*, 29 (3), 3840–3852. <https://doi.org/10.1007/s11356-021-15945-5>
- Aftab, M., Butt, M. Z., Ali, D., Bashir, F., & Khan, T. M. (2021). Optical and electrical properties of NiO and Cu-doped NiO thin films synthesized by spray pyrolysis. *Optical Materials*, 119. <https://doi.org/10.1016/j.optmat.2021.111369>
- Akhtaruzzaman, MD., Hasan, A. K. M., RAIFUKU, I. R., Ishikawa, Y., Sarkar, D. K., Sobayel, K., Karim, M., Ul-Hamid, A., Abdullah, H., Uraoka, Y., Amin, N., & Sopian, K. (2020). Air-Stable Perovskite Photovoltaic Cells with Low Temperature Deposited NiO<sub>x</sub> as Efficient Hole-Transporting Material. *Optical Materials Express*, 10 (8), 1801–1816. <https://doi.org/10.1364/ome.391321>
- Akkaya, M., & Akman, E. (2021). The Synthesis Copper-doped Nickel Oxide and Application of Hybrid Nano-lubricants as a Compressor Oil. *Gazi Journal of Engineering Sciences*, 7 (2), 134–142. <https://doi.org/10.30855/gmbd.2021.02.06>
- Aliahmad, M., Rahdar, A., & Azizi, Y. (2014). Synthesis of Cu Doped NiO Nanoparticles by Chemical Method. In *JNS* (Vol. 4).
- Arumugam, G. M., Karunakaran, S. K., Liu, C., Zhang, C., Guo, F., Wu, S., & Mai, Y. (2021). Inorganic hole transport layers in inverted perovskite solar cells: A review. *Nano Select*, 2 (6), 1081–1116. <https://doi.org/10.1002/nano.202000200>
- Ashok Kumar Reddy, Y., Sivasankar Reddy, A., & Sreedhara Reddy, P. (2013). Substrate temperature dependent properties of Cu doped NiO films deposited by dc reactive magnetron sputtering. *Journal of Materials Science and Technology*, 29 (7), 647–651. <https://doi.org/10.1016/j.jmst.2013.03.005>
- Bai, F., Hu, Y., Hu, Y., Qiu, T., Miao, X., & Zhang, S. (2018). Lead-free, air-stable ultrathin Cs<sub>3</sub>Bi<sub>2</sub>I<sub>9</sub> perovskite nanosheets for solar cells. *Solar Energy Materials and Solar Cells*, 184, 15–21. <https://doi.org/10.1016/j.solmat.2018.04.032>
- Bashir, A., Haur, L. J., Shukla, S., Gupta, D., Baikie, T., Chakraborty, S., Patidar, R., Bruno, A., Mhaisalkar, S., & Akhter, Z. (2019). Cu-doped nickel oxide interface layer with nanoscale thickness for efficient and highly stable printable carbon-based perovskite solar cell. *Solar Energy*, 182, 225–236. <https://doi.org/10.1016/j.solener.2019.02.056>
- Bellis, M. (2019). *History and Definition of a Solar Cell*. [thoughtco.com/history-of-solar-cells-1992435](http://thoughtco.com/history-of-solar-cells-1992435)
- Benramache, S., Benhaoua, B., & Guezzoun, H. (2020). Study the Effect of Cu Doping on Optical and Structural Properties of NiO Thin Films. *Annals of West University of Timisoara - Physics*, 62 (1), 15–22. <https://doi.org/10.2478/awutp-2020-0002>

- Bhujel, K., Ningthoujam, S. S., Singh, L. R., & Rai, S. (2020). Effect of solution aging on properties of spin coated zinc oxide thin films. *Materials Today: Proceedings*, *xxxx*, 2–5. <https://doi.org/10.1016/j.matpr.2020.07.099>
- Bunaciu, A. A., Udriștioiu, E. gabriela, & Aboul-Enein, H. Y. (2015). X-Ray Diffraction: Instrumentation and Applications. In *Critical Reviews in Analytical Chemistry* (Vol. 45, Issue 4, pp. 289–299). Taylor and Francis Ltd. <https://doi.org/10.1080/10408347.2014.949616>
- Burschka, J., Pellet, N., Moon, S. J., Humphry-Baker, R., Gao, P., Nazeeruddin, M. K., & Grätzel, M. (2013). Sequential deposition as a route to high-performance perovskite-sensitized solar cells. *Nature*, *499* (7458), 316–319. <https://doi.org/10.1038/nature12340>
- ÇAYIR TAŞDEMİRÇİ, T. (2020). Synthesis of copper-doped nickel oxide thin films: Structural and optical studies. *Chemical Physics Letters*, *738*. <https://doi.org/10.1016/j.cplett.2019.136884>
- Chatterjee, S., & Pal, A. J. (2016). Introducing Cu<sub>2</sub>O thin films as a hole-transport layer in efficient planar perovskite solar cell structures. *Journal of Physical Chemistry C*, *120* (3), 1428–1437. <https://doi.org/10.1021/acs.jpcc.5b11540>
- Chen, L.-C., & Tseng, Z.-L. (2017). ZnO-Based Electron Transporting Layer for Perovskite Solar Cells. *Nanostructured Solar Cells*, February. <https://doi.org/10.5772/65056>
- Chen, Q., de Marco, N., Yang, Y., Song, T. bin, Chen, C. C., Zhao, H., Hong, Z., Zhou, H., & Yang, Y. (2015). Under the spotlight: The organic-inorganic hybrid halide perovskite for optoelectronic applications. In *Nano Today* (Vol. 10, Issue 3, pp. 355–396). Elsevier B.V. <https://doi.org/10.1016/j.nantod.2015.04.009>
- Chung, I., Lee, B., He, J., Chang, R. P. H., & Kanatzidis, M. G. (2012a). All-solid-state dye-sensitized solar cells with high efficiency. *Nature*, *485* (7399), 486–489. <https://doi.org/10.1038/nature11067>
- Cullity, B. D. (Bernard D. (1978a). *Elements of x-ray diffraction*. Addison-Wesley Publishing Company, Inc.
- Das, M. R., Mukherjee, A., & Mitra, P. (2018). Influence of Cu incorporation on ionic conductivity and dielectric relaxation mechanism in NiO thin films synthesized by CBD. *Journal of Materials Science: Materials in Electronics*, *29* (2), 1216–1231. <https://doi.org/10.1007/s10854-017-8024-x>
- Dawood, M. O. (2015). Effect of Cu-Doping on Urbach Energy and Dispersion Parameters of Cu:NiO Film Deposited by CSP. *International Letters of Chemistry, Physics and Astronomy*, *48*, 138–145. <https://doi.org/10.18052/www.scipress.com/ilcpa.48.138>
- Docampo, P., Ball, J. M., Darwich, M., Eperon, G. E., & Snaith, H. J. (2013). Efficient organometal trihalide perovskite planar-heterojunction solar cells on flexible polymer substrates. *Nature Communications*, *4*. <https://doi.org/10.1038/ncomms3761>

- Dong, J., Shi, J., Li, D., Luo, Y., & Meng, Q. (2015). Controlling the conduction band offset for highly efficient ZnO nanorods based perovskite solar cell. *Applied Physics Letters*, *107* (7), 1–6. <https://doi.org/10.1063/1.4929435>
- Emamdoust, A., & Farjami Shayesteh, S. (2018). Surface and electrochemical properties of flower-like Cu-NiO compounds. *Journal of Alloys and Compounds*, *738*, 432–439. <https://doi.org/10.1016/j.jallcom.2017.12.144>
- Etgar, L., Gao, P., Xue, Z., Peng, Q., Chandiran, A. K., Liu, B., Nazeeruddin, M. K., & Grätzel, M. (2012). Mesoscopic CH<sub>3</sub>NH<sub>3</sub>PbI<sub>3</sub>/TiO<sub>2</sub> heterojunction solar cells. *Journal of the American Chemical Society*, *134* (42), 17396–17399. <https://doi.org/10.1021/ja307789s>
- Ethiraj, A. S., Uttam, P., K, V., Chong, K. F., & Ali, G. A. M. (2020). Photocatalytic performance of a novel semiconductor nanocatalyst: Copper doped nickel oxide for phenol degradation. *Materials Chemistry and Physics*, *242*. <https://doi.org/10.1016/j.matchemphys.2019.122520>
- Fang, D., Li, C., Wang, N., Li, P., & Yao, P. (2013). Structural and optical properties of Mg-doped ZnO thin films prepared by a modified Pechini method. *Crystal Research and Technology*, *48* (5), 265–272. <https://doi.org/10.1002/crat.201200437>
- Fatema, K., & Arefin, M. S. (2022). Enhancing the efficiency of Pb-based and Sn-based perovskite solar cell by applying different ETL and HTL using SCAPS-ID. *Optical Materials*, *125*, 112036. <https://doi.org/10.1016/J.OPTMAT.2022.112036>
- Fatet, J. (2005). Recreating Edmond Becquerel's electrochemical actinometer. *Archives Des Sciences*, *58* (2), 149–158.
- Feng, H. J., Deng, W., Yang, K., Huang, J., & Zeng, X. C. (2017a). Double Perovskite Cs<sub>2</sub>BBiX<sub>6</sub> (B = Ag, Cu; X = Br, Cl)/TiO<sub>2</sub> Heterojunction: An Efficient Pb-Free Perovskite Interface for Charge Extraction. *Journal of Physical Chemistry C*, *121* (8), 4471–4480. <https://doi.org/10.1021/acs.jpcc.7b00138>
- Feng, M., Wang, M., Zhou, H., Li, W., Wang, S., Zang, Z., & Chen, S. (2020). High-Efficiency and Stable Inverted Planar Perovskite Solar Cells with Pulsed Laser Deposited Cu-Doped NiO<sub>x</sub> Hole-Transport Layers. *ACS Applied Materials and Interfaces*, *12* (45), 50684–50691. <https://doi.org/10.1021/acsami.0c15923>
- Filip, M. R., Hillman, S., Haghghirad, A. A., Snaith, H. J., & Giustino, F. (2016). Band Gaps of the Lead-Free Halide Double Perovskites Cs<sub>2</sub>BiAgCl<sub>6</sub> and Cs<sub>2</sub>BiAgBr<sub>6</sub> from Theory and Experiment. *Journal of Physical Chemistry Letters*, *7* (13), 2579–2585. <https://doi.org/10.1021/acs.jpcclett.6b01041>
- Franta, D., Negulescu, B., Thomas, L., Dahoo, P. R., Guyot, M., Ohlídal, I., Mistrík, J., & Yamaguchi, T. (2005). Optical properties of NiO thin films prepared by pulsed laser deposition technique. *Applied Surface Science*, *244* (1–4), 426–430. <https://doi.org/10.1016/j.apsusc.2004.09.150>

- Fu, H. (2019). Review of lead-free halide perovskites as light-absorbers for photovoltaic applications: From materials to solar cells. *Solar Energy Materials and Solar Cells*, *193*, 107–132. <https://doi.org/10.1016/j.solmat.2018.12.038>
- Gao, W., Ran, C., Xi, J., Jiao, B., Zhang, W., Wu, M., Hou, X., & Wu, Z. (2018). High-Quality Cs<sub>2</sub>AgBiBr<sub>6</sub> Double Perovskite Film for Lead-Free Inverted Planar Heterojunction Solar Cells with 2.2 % Efficiency. *Chem Phys Chem*, *19* (14), 1696–1700. <https://doi.org/10.1002/cphc.201800346>
- Gollu, S. R., Sharma, R., Srinivas, G., Kundu, S., & Gupta, D. (2015). Incorporation of SiO<sub>2</sub> dielectric nanoparticles for performance enhancement in P<sub>3</sub>HT:PCBM inverted organic solar cells. *Organic Electronics*, *24*, 43–50. <https://doi.org/10.1016/j.orgel.2015.05.017>
- Grätzel, M. (2014). *The light and shade of perovskite solar cells*. [www.nature.com/naturematerials](http://www.nature.com/naturematerials)
- Green, M. A., Ho-Baillie, A., & Snaith, H. J. (2014). The emergence of perovskite solar cells. In *Nature Photonics* (Vol. 8, Issue 7, pp. 506–514). Nature Publishing Group. <https://doi.org/10.1038/nphoton.2014.134>
- Greul, E., Petrus, M. L., Binek, A., Docampo, P., & Bein, T. (2017). Highly stable, phase pure Cs<sub>2</sub>AgBiBr<sub>6</sub> double perovskite thin films for optoelectronic applications. *Journal of Materials Chemistry A*, *5* (37), 19972–19981. <https://doi.org/10.1039/c7ta06816f>
- Guo, X., Luo, G., Liu, J., Liao, C., Wang, G., & Li, S. (2018). A 16.5% efficient perovskite solar cells with inorganic NiO film as hole transport material. *IEEE Journal of Photovoltaics*, *8* (4), 1039–1043. <https://doi.org/10.1109/JPHOTOV.2018.2825228>
- Hao, F., Stoumpos, C. C., Chang, R. P. H., & Kanatzidis, M. G. (2014). Anomalous band gap behavior in mixed Sn and Pb perovskites enables broadening of absorption spectrum in solar cells. *Journal of the American Chemical Society*, *136* (22), 8094–8099. <https://doi.org/10.1021/ja5033259>
- He, Q., Yao, K., Wang, X., Xia, X., Leng, S., & Li, F. (2017). Room-Temperature and Solution-Processable Cu-Doped Nickel Oxide Nanoparticles for Efficient Hole-Transport Layers of Flexible Large-Area Perovskite Solar Cells. *ACS Applied Materials and Interfaces*, *9* (48), 41887–41897. <https://doi.org/10.1021/acsami.7b13621>
- Hodes, G., & Cahen, D. (2014). Perovskite cells roll forward. In *Nature Photonics* (Vol. 8, Issue 2, pp. 87–88). <https://doi.org/10.1038/nphoton.2014.5>
- Hou, Y., Chen, W., Baran, D., Stubhan, T., Luechinger, N. A., Hartmeier, B., Richter, M., Min, J., Chen, S., Quiroz, C. O. R., Li, N., Zhang, H., Heumueller, T., Matt, G. J., Osvet, A., Forberich, K., Zhang, Z. G., Li, Y., Winter, B., Brabec, C. J. (2016). Overcoming the Interface Losses in Planar Heterojunction Perovskite-Based Solar Cells. *Advanced Materials*, *28* (25), 5112–5120. <https://doi.org/10.1002/adma.201504168>



- Hsu, C. C., Su, H. W., Hou, C. H., Shyue, J. J., & Tsai, F. Y. (2015). Atomic layer deposition of NiO hole-transporting layers for polymer solar cells. *Nanotechnology*, *26* (38), 385201. <https://doi.org/10.1088/0957-4484/26/38/385201>
- Huang, T. C., & Predecki, P. K. (1997). Copyright © JCPDS-International Centre for Diffraction Data 1997 Copyright (C) JCPDS-International Centre for Diffraction Data. In *Advances in X-ray Analysis* (Vol. 40). [www.dxcicdd.com](http://www.dxcicdd.com)
- Huang, Y. T., Kavanagh, S. R., Scanlon, D. O., Walsh, A., & Hoye, R. L. Z. (2021). Perovskite-inspired materials for photovoltaics and beyond—from design to devices. In *Nanotechnology* (Vol. 32, Issue 13). IOP Publishing Ltd. <https://doi.org/10.1088/1361-6528/abcf6d>
- Huang, Y., Wen, W., Mukherjee, S., Ade, H., Kramer, E. J., & Bazan, G. C. (2014). High-molecular-weight insulating polymers can improve the performance of molecular solar cells. *Advanced Materials*, *26* (24), 4168–4172. <https://doi.org/10.1002/adma.201400497>
- Igbari, F., Wang, R., Wang, Z. K., Ma, X. J., Wang, Q., Wang, K. L., Zhang, Y., Liao, L. S., & Yang, Y. (2019). Composition Stoichiometry of Cs<sub>2</sub>AgBiBr<sub>6</sub> Films for Highly Efficient Lead-Free Perovskite Solar Cells. *Nano Letters*, *19* (3), 2066–2073. <https://doi.org/10.1021/acs.nanolett.9b00238>
- Im, J. H., Lee, C. R., Lee, J. W., Park, S. W., & Park, N. G. (2011). 6.5% efficient perovskite quantum-dot-sensitized solar cell. *Nanoscale*, *3* (10), 4088–4093. <https://doi.org/10.1039/c1nr10867k>
- Jeon, N. J., Noh, J. H., Yang, W. S., Kim, Y. C., Ryu, S., Seo, J., & Seok, S. il. (2015). Compositional engineering of perovskite materials for high-performance solar cells. *Nature*, *517* (7535), 476–480. <https://doi.org/10.1038/nature14133>
- Joshi, I., Truong, V. K., Elbourne, A., Chapman, J., & Cozzolino, D. (2019). Influence of the scanning temperature on the classification of whisky samples analysed by UV-VIS spectroscopy. *Applied Sciences (Switzerland)*, *9* (16). <https://doi.org/10.3390/app9163254>
- Jung, J. W., Chueh, C. C., & Jen, A. K. Y. (2015). A Low-Temperature, Solution-Processable, Cu-Doped Nickel Oxide Hole-Transporting Layer via the Combustion Method for High-Performance Thin-Film Perovskite Solar Cells. *Advanced Materials*, *27* (47), 7874–7880. <https://doi.org/10.1002/adma.201503298>
- Kim, H. S., Im, S. H., & Park, N. G. (2014). Organolead halide perovskite: New horizons in solar cell research. *Journal of Physical Chemistry C*, *118* (11), 5615–5625. <https://doi.org/10.1021/jp409025w>
- Kim, H. S., Lee, C. R., Im, J. H., Lee, K. B., Moehl, T., Marchioro, A., Moon, S. J., Humphry-Baker, R., Yum, J. H., Moser, J. E., Grätzel, M., & Park, N. G. (2012). Lead iodide perovskite sensitized all-solid-state submicron thin film mesoscopic solar cell with efficiency exceeding 9%. *Scientific Reports*, *2*, 1–7. <https://doi.org/10.1038/srep00591>

- Kim, J. K. (2019). PEG-assisted sol-gel synthesis of compact nickel oxide hole-selective layer with modified interfacial properties for organic solar cells. *Polymers*, *11* (1), 1–8. <https://doi.org/10.3390/polym11010120>
- Ko, Y., Kim, Y., Kong, S. Y., Kunnan, S. C., & Jun, Y. (2018). Improved performance of sol-gel ZnO-based perovskite solar cells via TiCl<sub>4</sub> interfacial modification. *Solar Energy Materials and Solar Cells*, *183* (March), 157–163. <https://doi.org/10.1016/j.solmat.2018.04.021>
- Kojima, A., Teshima, K., Shirai, Y., & Miyasaka, T. (2009). Organometal halide perovskites as visible-light sensitizers for photovoltaic cells. *Journal of the American Chemical Society*, *131* (17), 6050–6051. <https://doi.org/10.1021/ja809598r>
- Koster, A. J., Ziese, U., Verkleij, A. J., Janssen, A. H., & de Jong, K. P. (2000). Three-dimensional transmission electron microscopy: a novel imaging and characterization technique with nanometer scale resolution for materials science. *Journal of Physical Chemistry B*, *104* (40), 9368–9370. <https://doi.org/10.1021/jp0015628>
- Kumar, A., Balasubramaniam, K. R., Kangsabanik, J., Vikram, & Alam, A. (2016). Crystal structure, stability, and optoelectronic properties of the organic-inorganic wide-band-gap perovskite CH<sub>3</sub>NH<sub>3</sub>BaI<sub>3</sub>: Candidate for transparent conductor applications. *Physical Review B*, *94* (18). <https://doi.org/10.1103/PhysRevB.94.180105>
- Kumar, A., Sahu, S., Patel, M., & Tiwari, S. (2020). *Preparation, Fabrication and Characterization of Sol-Gel ZnO Thin Films for Organic Solar Cells*. *33* (1), 24–30.
- Kumari, L., Li, W. Z., Vannoy, C. H., Leblanc, R. M., & Wang, D. Z. (2009). Vertically aligned and interconnected nickel oxide nanowalls fabricated by hydrothermal route. *Crystal Research and Technology*, *44* (5), 495–499. <https://doi.org/10.1002/crat.200800583>
- Lakhdar, N., & Hima, A. (2020). Electron transport material effect on performance of perovskite solar cells based on CH<sub>3</sub>NH<sub>3</sub>GeI<sub>3</sub>. *Optical Materials*, *99* (November), 109517. <https://doi.org/10.1016/j.optmat.2019.109517>
- Lamba, R. S., Basera, P., Bhattacharya, S., & Sapra, S. (2019). Band Gap Engineering in Cs<sub>2</sub> (NaxAg1-x)BiCl<sub>6</sub> Double Perovskite Nanocrystals. *Journal of Physical Chemistry Letters*, *10* (17), 5173–5181. <https://doi.org/10.1021/acs.jpcclett.9b02168>
- Li, Y. H., Lu, X., Wang, R., Ma, Y. Y., Duhm, S., & Fung, M. K. (2017a). Cu-Doped nickel oxide prepared using a low-temperature combustion method as a hole-injection layer for high-performance OLEDs. *Journal of Materials Chemistry C*, *5* (45), 11751–11757. <https://doi.org/10.1039/c7tc03884d>
- Liang, L., Sun, Y., Lei, F., Gao, S., & Xie, Y. (2014). Free-floating ultrathin tin monoxide sheets for solar-driven photoelectrochemical water splitting. *Journal of Materials Chemistry A*, *2* (27), 10647–10653. <https://doi.org/10.1039/c4ta01659a>
- Lin, L., Jones, T. W., Yang, T. C. J., Duffy, N. W., Li, J., Zhao, L., Chi, B., Wang, X., & Wilson, G. J. (2020). Inorganic Electron Transport Materials in Perovskite Solar Cells.

- Lin, Z., Du, C., Yan, B., Wang, C., & Yang, G. (2018). Two-dimensional amorphous NiO as a plasmonic photocatalyst for solar H<sub>2</sub> evolution. *Nature Communications*, 9 (1). <https://doi.org/10.1038/s41467-018-06456-y>
- Liu, J., Aydin, E., Yin, J., de Bastiani, M., Isikgor, F. H., Rehman, A. U., Yengel, E., Ugur, E., Harrison, G. T., Wang, M., Gao, Y., Khan, J. I., Babics, M., Allen, T. G., Subbiah, A. S., Zhu, K., Zheng, X., Yan, W., Xu, F., ... de Wolf, S. (2021). 28.2%-efficient, outdoor-stable perovskite/silicon tandem solar cell. *Joule*, 5 (12), 3169–3186. <https://doi.org/10.1016/j.joule.2021.11.003>
- Liu, M., Johnston, M. B., & Snaith, H. J. (2013). Efficient planar heterojunction perovskite solar cells by vapour deposition. *Nature*, 501 (7467), 395–398. <https://doi.org/10.1038/nature12509>
- Liu, M.-H., Zhou, Z.-J., Zhang, P.-P., Tian, Q.-W., Zhou, W.-H., Kou, D.-X., & Wu, S.-X. (2016). p-type Li, Cu-codoped NiOx hole-transporting layer for efficient planar perovskite solar cells. *Optics Express*, 24 (22), A1349. <https://doi.org/10.1364/oe.24.0a1349>
- Liu, Y., Nag, A., Manna, L., & Xia, Z. (2021). Lead-Free Double Perovskite Cs<sub>2</sub>AgInCl<sub>6</sub>. In *Angewandte Chemie - International Edition* (Vol. 60, Issue 21, pp. 11592–11603). John Wiley and Sons Inc. <https://doi.org/10.1002/anie.202011833>
- Luo, J., Wang, Y., & Zhang, Q. (2018). Progress in perovskite solar cells based on ZnO nanostructures. *Solar Energy*, 163 (October 2017), 289–306. <https://doi.org/10.1016/j.solener.2018.01.035>
- Ma, H., Imran, M., Dang, Z., & Hu, Z. (2018). Growth of Metal Halide Perovskite, from Nanocrystal to Micron-Scale Crystal: A Review. *Crystals*, 8 (5), 182. <https://doi.org/10.3390/cryst8050182>
- Mahmud, M. A., Elumalai, N. K., Upama, M. B., Wang, D., Chan, K. H., Wright, M., Xu, C., Haque, F., & Uddin, A. (2017). Low temperature processed ZnO thin film as electron transport layer for efficient perovskite solar cells. *Solar Energy Materials and Solar Cells*, 159, 251–264. <https://doi.org/10.1016/j.solmat.2016.09.014>
- Manders, J. R., Tsang, S.-W., Hartel, M. J., Lai, T.-H., Chen, S., Amb, C. M., Reynolds, J. R., & So, F. (2013). *Solution-Processed Nickel Oxide Hole Transport Layers in High Efficiency Polymer Photovoltaic Cells*. [www.MaterialsViews.com](http://www.MaterialsViews.com)
- Mäntele, W., & Deniz, E. (2017). UV–VIS absorption spectroscopy: Lambert-Beer reloaded. In *Spectrochimica Acta - Part A: Molecular and Biomolecular Spectroscopy* (Vol. 173, pp. 965–968). Elsevier B.V. <https://doi.org/10.1016/j.saa.2016.09.037>
- Marra, W. C., Eisenberger, P., & Cho, A. Y. (1979). X-ray total-external-reflection-Bragg diffraction: A structural study of the GaAs-Al interface. *Journal of Applied Physics*, 50 (11), 6927–6933. <https://doi.org/10.1063/1.325845>

- Martin, L., Martinez, H., Poinot, D., Pecquenard, B., & le Cras, F. (2013). Comprehensive X-ray photoelectron spectroscopy study of the conversion reaction mechanism of CuO in lithiated thin film electrodes. *Journal of Physical Chemistry C*, *117* (9), 4421–4430. <https://doi.org/10.1021/jp3119633>
- McClure, E. T., Ball, M. R., Windl, W., & Woodward, P. M. (2016). Cs<sub>2</sub>AgBiX<sub>6</sub> (X = Br, Cl): New Visible Light Absorbing, Lead-Free Halide Perovskite Semiconductors. *Chemistry of Materials*, *28* (5), 1348–1354. <https://doi.org/10.1021/acs.chemmater.5b04231>
- Mironova-Ulmane, N., Kuzmin, A., Sildos, I., Puust, L., & Grabis, J. (2019). Magnon and Phonon Excitations in Nanosized NiO. *Latvian Journal of Physics and Technical Sciences*, *56* (2), 61–72. <https://doi.org/10.2478/lpts-2019-0014>
- Mohamad Noh, M. F., Teh, C. H., Daik, R., Lim, E. L., Yap, C. C., Ibrahim, M. A., Ahmad Ludin, N., Mohd Yusoff, A. R. bin, Jang, J., & Mat Teridi, M. A. (2018). The architecture of the electron transport layer for a perovskite solar cell. *Journal of Materials Chemistry C*, *6* (4), 682–712. <https://doi.org/10.1039/c7tc04649a>
- Mohammed, B. K., Mohammed, M. K. A., & Ahmed, D. S. (2021). The effect of copper doping on the structural, optical, and electrical properties of nickel oxide thin films for optoelectronic applications. *Journal of Sol-Gel Science and Technology*, *99* (1). <https://doi.org/10.1007/s10971-021-05537-7>
- Nair, S., Patel, S. B., & Gohel, J. v. (2020). Recent trends in efficiency-stability improvement in perovskite solar cells. *Materials Today Energy*, *17*, 100449. <https://doi.org/10.1016/j.mtener.2020.100449>
- Najafi, M., & Eshghi, H. (2015). The effect of Cu-doping on physical properties of nanostructured NiO thin films prepared by spray pyrolysis technique. In *Scientia Iranica F* (Vol. 22, Issue 3). [www.scientiairanica.com](http://www.scientiairanica.com)
- Najafi, M., di Giacomo, F., Zhang, D., Shanmugam, S., Senes, A., Verhees, W., Hadipour, A., Galagan, Y., Aernouts, T., Veenstra, S., & Andriessen, R. (2018). Highly Efficient and Stable Flexible Perovskite Solar Cells with Metal Oxides Nanoparticle Charge Extraction Layers. *Small*, *14* (12), 1–10. <https://doi.org/10.1002/sml.201702775>
- Ning, W., Wang, F., Wu, B., Lu, J., Yan, Z., Liu, X., Tao, Y., Liu, J. M., Huang, W., Fahlman, M., Hultman, L., Sum, T. C., & Gao, F. (2018). Long Electron–Hole Diffusion Length in High-Quality Lead-Free Double Perovskite Films. *Advanced Materials*, *30* (20). <https://doi.org/10.1002/adma.201706246>
- Niu, G., Li, W., Li, J., & Wang, L. (2016). Progress of interface engineering in perovskite solar cells. *Science China Materials*, *59* (9), 728–742. <https://doi.org/10.1007/s40843-016-5094-6>
- Noel, N. K., Stranks, S. D., Abate, A., Wehrenfennig, C., Guarnera, S., Haghighirad, A. A., Sadhanala, A., Eperon, G. E., Pathak, S. K., Johnston, M. B., Petrozza, A., Herz, L. M., & Snaith, H. J. (2014). Lead-free organic-inorganic tin halide perovskites for

- photovoltaic applications. *Energy and Environmental Science*, 7 (9), 3061–3068. <https://doi.org/10.1039/c4ee01076k>
- Noh, J. H., Im, S. H., Heo, J. H., Mandal, T. N., & Seok, S. il. (2013). Chemical management for colorful, efficient, and stable inorganic-organic hybrid nanostructured solar cells. *Nano Letters*, 13 (4), 1764–1769. <https://doi.org/10.1021/nl400349b>
- Nuraje, N., Asmatulu, R., & Kudaibergenov, S. (2012). Metal Oxide-based Functional Materials for Solar Energy Conversion: A Review. In *Current Inorganic Chemistry* (Vol. 2).
- Ouyang, D., Huang, Z., & Choy, W. C. H. (2019). Solution-Processed Metal Oxide Nanocrystals as Carrier Transport Layers in Organic and Perovskite Solar Cells. *Advanced Functional Materials*, 29 (1), 1–18. <https://doi.org/10.1002/adfm.201804660>
- Pandey, A., Dalal, S., Dutta, S., & Dixit, A. (2021). Structural characterization of polycrystalline thin films by X-ray diffraction techniques. In *Journal of Materials Science: Materials in Electronics* (Vol. 32, Issue 2, pp. 1341–1368). Springer. <https://doi.org/10.1007/s10854-020-04998-w>
- Pantaler, M., Cho, K. T., Queloz, V., Benito, I. G., Fettikeyhauer, C., Anusca, I., Nazeeruddin, M. K., Lupascu, D. C., & Grancini, G. (n.d.). *Hysteresis-Free Lead-Free Double Perovskite Solar Cells by Interface Engineering*. <http://pubs.acs.org>
- Pantaler, M., Fettikeyhauer, C., Nguyen, H. L., Anusca, I., & Lupascu, D. C. (2018). Deposition routes of Cs<sub>2</sub>AgBiBr<sub>6</sub> double perovskites for photovoltaic applications. *MRS Advances*, 3 (32), 1819–1823. <https://doi.org/10.1557/adv.2018.151>
- Qiao, B., Zhao, S., Xu, Z., & Xu, X. (2016). Synthesis of ZnO quantum dots and their agglomeration mechanisms along with emission spectra based on ageing time and temperature. *Chinese Physics B*, 25 (9). <https://doi.org/10.1088/1674-1056/25/9/098102>
- Qiu, Z., Yuan, S., Gong, H., Zhang, H., Qiu, X., Luo, T., Cao, B., & Du, H. (2017). The Influence of Physical Properties of ZnO Films on the Efficiency of Planar ZnO/Perovskite/P3HT Solar Cell. *Journal of the American Ceramic Society*, 100 (1), 176–184. <https://doi.org/10.1111/jace.14491>
- Reddy, B. R., Harish, G. S., Reddy, C. S., & Reddy, P. S. (2014). Synthesis and characterization of Cu doped NiO nanoparticles. In *www.ijmer.com* (Vol. 4). [www.ijmer.com](http://www.ijmer.com)
- Reddy, Y. A. K., Reddy, A. M., Reddy, A. S., & Reddy, P. S. (2013). Structural and electrical properties of pure and Cu doped NiO films deposited at various oxygen partial pressures. *AIP Conference Proceedings*, 1512, 640–641. <https://doi.org/10.1063/1.4791200>
- Renaud, G. (1998). Oxide surfaces and metal/oxide interfaces studied by grazing incidence X-ray scattering. In *Surface Science Reports* (Vol. 32).

- Renaud, G., Lazzari, R., & Leroy, F. (2009). Probing surface and interface morphology with Grazing Incidence Small Angle X-Ray Scattering. In *Surface Science Reports* (Vol. 64, Issue 8, pp. 255–380). Elsevier. <https://doi.org/10.1016/j.surfrep.2009.07.002>
- Saadaldin, N., Alsloum, M. N., & Hussain, N. (2015). Preparing of Copper Oxides Thin Films by Chemical Bath Deposition (CBD) for Using in Environmental Application. *Energy Procedia*, 74, 1459–1465. <https://doi.org/10.1016/j.egypro.2015.07.794>
- Sahoo, P., Sharma, A., Padhan, S., & Thangavel, R. (2021). Cu doped NiO thin film photocathodes for enhanced PEC performance. *Superlattices and Microstructures*, 159. <https://doi.org/10.1016/j.spmi.2021.107050>
- Sahoo, P., Sharma, A., & Thangavel, R. (2019). Influence of Cu incorporation on physical properties of nickel oxide thin films synthesized by sol-gel method. *AIP Conference Proceedings*, 2115. <https://doi.org/10.1063/1.5113460>
- Sahoo, P., & Thangavel, R. (2018). Effect of annealing temperature on physical properties of solution processed nickel oxide thin films. *AIP Conference Proceedings*, 1961, 0–5. <https://doi.org/10.1063/1.5035243>
- Saliba, M., Matsui, T., Seo, J. Y., Domanski, K., Correa-Baena, J. P., Nazeeruddin, M. K., Zakeeruddin, S. M., Tress, W., Abate, A., Hagfeldt, A., & Grätzel, M. (2016). Cesium-containing triple cation perovskite solar cells: Improved stability, reproducibility and high efficiency. *Energy and Environmental Science*, 9 (6), 1989–1997. <https://doi.org/10.1039/c5ee03874j>
- Sato, K., Kim, S., Komuro, S., & Zhao, X. (2016a). Characteristics of Cu-doped amorphous NiO thin films formed by RF magnetron sputtering. *Japanese Journal of Applied Physics*, 55 (6). <https://doi.org/10.7567/JJAP.55.06GJ10>
- Sharma, A., Chakraborty, M., Thangavel, R., & Udayabhanu, G. (2018). Hydrothermal growth of undoped and boron doped ZnO nanorods as a photoelectrode for solar water splitting applications. *Journal of Sol-Gel Science and Technology*, 85 (1), 1–11. <https://doi.org/10.1007/s10971-017-4536-3>
- Simeone, D., Baldinozzi, G., Gosset, D., le Caer, S., & Bérrar, J. F. (2013). Grazing incidence X-ray diffraction for the study of polycrystalline layers. *Thin Solid Films*, 530, 9–13. <https://doi.org/10.1016/j.tsf.2012.07.068>
- Snaith, H. J. (2013). Perovskites: The emergence of a new era for low-cost, high-efficiency solar cells. In *Journal of Physical Chemistry Letters* (Vol. 4, Issue 21, pp. 3623–3630). <https://doi.org/10.1021/jz4020162>
- Son, D. Y., Im, J. H., Kim, H. S., & Park, N. G. (2014). 11% efficient perovskite solar cell based on ZnO nanorods: An effective charge collection system. *Journal of Physical Chemistry C*, 118 (30), 16567–16573. <https://doi.org/10.1021/jp412407j>
- Spalla, M., Planes, E., Perrin, L., Matheron, M., Berson, S., & Flandin, L. (2019). Alternative Electron Transport Layer Based on Al-Doped ZnO and SnO<sub>2</sub> for

- Perovskite Solar Cells: Impact on Microstructure and Stability. *ACS Applied Energy Materials*, 2 (10), 7183–7195. <https://doi.org/10.1021/acsaem.9b01160>
- Steirer, K. X., Chesin, J. P., Widjonarko, N. E., Berry, J. J., Miedaner, A., Ginley, D. S., & Olson, D. C. (2010). Solution deposited NiO thin-films as hole transport layers in organic photovoltaics. *Organic Electronics*, 11 (8), 1414–1418. <https://doi.org/10.1016/j.orgel.2010.05.008>
- Subbiah, A. S., Halder, A., Ghosh, S., Mahuli, N., Hodes, G., & Sarkar, S. K. (2014). Inorganic hole conducting layers for perovskite-based solar cells. *Journal of Physical Chemistry Letters*, 5 (10), 1748–1753. <https://doi.org/10.1021/jz500645n>
- Taheri-Ledari, R., Valadi, K., & Maleki, A. (2020). High-performance -free perovskite solar cell: An efficient composition of ZnO nr, RGO, and CuInS<sub>2</sub> QDs, as electron-transporting layer matrix. *Progress in Photovoltaics: Research and Applications*, 28 (9), 956–970. <https://doi.org/10.1002/pip.3306>
- Tauc, J., Grigorovici, R., & Vancu, A. (1966). J. TAUC *et al.* Optical Properties and Electronic Structure of Ge Optical Properties and Electronic Structure of Amorphous Germanium. In *phys. stat. sol* (Vol. 15).
- Tavakoli, M. M., Tavakoli, R., Nourbakhsh, Z., Waleed, A., Virk, U. S., & Fan, Z. (2016). High Efficiency and Stable Perovskite Solar Cell Using ZnO/rGO QDs as an Electron Transfer Layer. *Advanced Materials Interfaces*, 3 (11), 1–10. <https://doi.org/10.1002/admi.201500790>
- Thomas, H. E. (2010). *Structure determination of thin polymer films using GIXRD and AFM*.
- Tsarev, S., & Troshin, P. A. (2020). Surface modification of ZnO electron transport layer with thermally evaporated WO<sub>3</sub> for stable perovskite solar cells. *Synthetic Metals*, 269 (August), 116547. <https://doi.org/10.1016/j.synthmet.2020.116547>
- Varunkumar, K., Ethiraj, A. S., & Kechiantz, A. (2018). Optical absorption and thermal stability study of Cu doped NiO nanoparticles. *AIP Conference Proceedings*, 1953. <https://doi.org/10.1063/1.5032509>
- Volonakis, G., Filip, M. R., Haghghirad, A. A., Sakai, N., Wenger, B., Snaith, H. J., & Giustino, F. (2016). Lead-Free Halide Double Perovskites via Heterovalent Substitution of Noble Metals. *Journal of Physical Chemistry Letters*, 7 (7), 1254–1259. <https://doi.org/10.1021/acs.jpcclett.6b00376>
- Volonakis, G., Haghghirad, A. A., Snaith, H. J., & Giustino, F. (2017). Route to Stable Lead-Free Double Perovskites with the Electronic Structure of CH<sub>3</sub>NH<sub>3</sub>PbI<sub>3</sub>: A Case for Mixed-Cation [Cs/CH<sub>3</sub>NH<sub>3</sub>/CH (NH<sub>2</sub>)<sub>2</sub>]<sub>2</sub>InBiBr<sub>6</sub>. *Journal of Physical Chemistry Letters*, 8 (16), 3917–3924. <https://doi.org/10.1021/acs.jpcclett.7b01584>
- Wang, B., Li, N., Yang, L., Dall'agnese, C., Jena, A. K., Sasaki, S. I., Miyasaka, T., Tamiaki, H., & Wang, X. F. (2021). Chlorophyll Derivative-Sensitized TiO<sub>2</sub> Electron Transport Layer for Record Efficiency of Cs<sub>2</sub>AgBiBr<sub>6</sub> Double Perovskite Solar Cells.

*Journal of the American Chemical Society*, 143 (5), 2207–2211.  
<https://doi.org/10.1021/jacs.0c12786>

- Wang, M., Zeng, P., Bai, S., Gu, J., Li, F., Yang, Z., & Liu, M. (2018). High-Quality Sequential-Vapor-Deposited Cs<sub>2</sub>AgBiBr<sub>6</sub> Thin Films for Lead-Free Perovskite Solar Cells. *Solar RRL*, 2 (12). <https://doi.org/10.1002/solr.201800217>
- Wang, S. H., Jian, S. R., Chen, G. J., Cheng, H. Z., & Juang, J. Y. (2019). Annealing-driven microstructural evolution and its effects on the surface and nanomechanical properties of Cu-doped NiO thin films. *Coatings*, 9 (2). <https://doi.org/10.3390/COATINGS9020107>
- Wang, S., Yousefi Amin, A. A., Wu, L., Cao, M., Zhang, Q., & Ameri, T. (2021). Perovskite Nanocrystals: Synthesis, Stability, and Optoelectronic Applications. *Small Structures*, 2 (3), 2000124. <https://doi.org/10.1002/ssr.202000124>
- Wu, C., Zhang, Q., Liu, Y., Luo, W., Guo, X., Huang, Z., Ting, H., Sun, W., Zhong, X., Wei, S., Wang, S., Chen, Z., & Xiao, L. (2018). The Dawn of Lead-Free Perovskite Solar Cell: Highly Stable Double Perovskite Cs<sub>2</sub>AgBiBr<sub>6</sub> Film. *Advanced Science*, 5 (3). <https://doi.org/10.1002/advs.201700759>
- Yang, W. S., Noh, J. H., Jeon, N. J., Kim, Y. C., Ryu, S., Seo, J., & Seok, S. il. (2015a). High-performance photovoltaic perovskite layers fabricated through intramolecular exchange. *Science*, 348 (6240), 1234–1237. <https://doi.org/10.1126/science.aaa9272>
- Yang, X., Chen, Y., Liu, P., Xiang, H., Wang, W., Ran, R., Zhou, W., & Shao, Z. (2020). Simultaneous Power Conversion Efficiency and Stability Enhancement of Cs<sub>2</sub>AgBiBr<sub>6</sub> Lead-Free Inorganic Perovskite Solar Cell through Adopting a Multifunctional Dye Interlayer. *Advanced Functional Materials*, 30 (23). <https://doi.org/10.1002/adfm.202001557>
- Yang, X., Liu, W., Pan, G., & Sun, Y. (2018). Modulation of oxygen in NiO:Cu films toward a physical insight of NiO:Cu/c-Si heterojunction solar cells. *Journal of Materials Science*, 53 (16), 11684–11693. <https://doi.org/10.1007/s10853-018-2430-1>
- Yin, X., Chen, P., Que, M., Xing, Y., Que, W., Niu, C., & Shao, J. (2016). Highly Efficient Flexible Perovskite Solar Cells Using Solution-Derived NiO<sub>x</sub> Hole Contacts. *ACS Nano*, 10 (3), 3630–3636. <https://doi.org/10.1021/acsnano.5b08135>
- Yin, X., Guo, Y., Xie, H., Que, W., & Kong, L. B. (2019). Nickel Oxide as Efficient Hole Transport Materials for Perovskite Solar Cells. *Solar RRL*, 3 (5), 1–27. <https://doi.org/10.1002/solr.201900001>
- Yoon, S., & Kang, D. W. (2018). Solution-processed nickel oxide hole transport layer for highly efficient perovskite-based photovoltaics. *Ceramics International*, 44 (8), 9347–9352. <https://doi.org/10.1016/j.ceramint.2018.02.147>
- You, I., & Noh, Y. Y. (2021). Toward high-performance p-type, tin-based perovskite thin film transistors. In *Applied Physics Letters* (Vol. 118, Issue 25). American Institute of Physics Inc. <https://doi.org/10.1063/5.0051382>



- Zhang, Y. D., & Zhao, L. (2019). Enhanced electroluminescence performance of all-inorganic quantum dot light-emitting diodes: A promising candidate for hole transport layer of Cu-doped NiO nanocrystals. *Journal of Materials Research*, *34* (16), 2757–2764. <https://doi.org/10.1557/jmr.2019.130>
- Zhao, B., Ke, X. K., Bao, J. H., Wang, C. L., Dong, L., Chen, Y. W., & Chen, H. L. (2009). Synthesis of flower-like NiO and effects of morphology on its catalytic properties. *Journal of Physical Chemistry C*, *113* (32), 14440–14447. <https://doi.org/10.1021/jp904186k>
- Zhao, L., Su, G., Liu, W., Cao, L., Wang, J., Dong, Z., & Song, M. (2011). Optical and electrochemical properties of Cu-doped NiO films prepared by electrochemical deposition. *Applied Surface Science*, *257* (9), 3974–3979. <https://doi.org/10.1016/j.apsusc.2010.11.160>
- Zhou, F., Zhu, H., & Li, C. (2019). A pretreatment method based on wavelet transform for quantitative analysis of UV–vis spectroscopy. *Optik*, *182*, 786–792. <https://doi.org/10.1016/j.ijleo.2019.01.115>
- Zhou, H., Chen, Q., Li, G., Luo, S., Song, T. B., Duan, H. S., Hong, Z., You, J., Liu, Y., & Yang, Y. (2014). Interface engineering of highly efficient perovskite solar cells. *Science*, *345* (6196), 542–546. <https://doi.org/10.1126/science.1254050>
- Zhou, Y., Zhou, Z., Chen, M., Zong, Y., Huang, J., Pang, S., & Padture, N. P. (2016). Doping and alloying for improved perovskite solar cells. In *Journal of Materials Chemistry A* (Vol. 4, Issue 45, pp. 17623–17635). Royal Society of Chemistry. <https://doi.org/10.1039/C6TA08699C>

## BIODATA

**Name** : Kamal Bhujel  
**Father's Name** : Krishna Bhujel  
**Mother's Name** : Doma Bhujel  
**Date of Birth** : 16.11.1990  
**Address** : Dilaram Tea Estate, P.O. Tung, Kurseong, Dist. Darjeeling,  
West Bengal; India

### **Educational Qualifications:**

X 2007 First Division

XII 2009 First Division

B. Sc. 2015 Second Division

M. Sc. (Physics) 2017 First Division

### **Research Experience:**

Worked as Research Fellow in the DST- SERB research project '**Synthesis and characterization of lead-free perovskite films for photovoltaic applications**' under Principal Investigator Dr. N. Surajkumar Singh at Physical Sciences Research Centre, Dept. of Physics, Pachhunga University College.

Registered Ph.D. researcher in Dept. of Physics, Mizoram University under the supervision of Prof. S. Rai and co-supervision of Dr. N. Suraj Kumar Singh since 2018.

## LIST OF PUBLICATIONS

1. K. Bhujel, S. S. Ningthoujam, L. R. Singh, and S. Rai, "Effect of solution aging on properties of spin coated zinc oxide thin films," *Mater Today Proc*, vol. 46, 2019, doi:10.1016/j.matpr.2020.07.099
2. K. Bhujel, S. Rai, and N. S. Singh, "Review on NiO thin film as hole transport layer in perovskite solar cell," *Nanosystems: Physics, Chemistry, Mathematics*, vol. 12, no. 6. ITMO University, pp. 703–710, Dec. 01, 2021. doi: 10.17586/2220-8054-2021-12-6-703-710.
3. Atheek, P., Puviarasu, P., Basha, S. M., & Bhujel, K. (2022). Micro Raman analysis on the impact of light ion irradiation of hydride vapor-phase epitaxy grown gallium nitride epilayers. *Thin Solid Films*, 761. <https://doi.org/10.1016/j.tsf.2022.139526>

## **PARTICULARS OF THE CANDIDATE**

NAME OF THE CANDIDATE : KAMAL BHUJEL  
DEGREE : PH.D.  
DEPARTMENT : PHYSICS  
TITLE OF THESIS : SYNTHESIS AND CHARACTERIZATION  
OF LEAD FREE PEROVSKITE FILMS FOR  
PHOTOVOLTAIC APPLICATIONS  
DATE OF ADMISSION : 10<sup>TH</sup> AUGUST 2018

### APPROVAL OF RESEARCH PROPOSAL:

1. DRC : 28<sup>TH</sup> MARCH 2019
2. BOS : 15<sup>TH</sup> APRIL 2019
3. SCHOOL BOARD : 8<sup>TH</sup> MAY 2019

MZU REGISTRATION NO. : 1807390

PH. D. REGISTRATION NO. & DATE : MZU/Ph.D./1246 OF 10.08.2018

HEAD

DEPARTMENT OF PHYSICS

**ABSTRACT**  
**SYNTHESIS AND CHARACTERIZATION OF LEAD-FREE**  
**PEROVSKITE FILMS FOR PHOTOVOLTAIC APPLICATIONS**

**AN ABSTRACT SUBMITTED IN PARTIAL FULFILLMENT OF**  
**THE REQUIREMENTS FOR THE DEGREE OF DOCTOR OF**  
**PHILOSOPHY**

**KAMAL BHUJEL**

**MZU REGN NO. 1807390**

**PH.D REGN NO. MZU/PH.D./1246 OF 10.08.2018**



**DEPARTMENT OF PHYSICS**  
**SCHOOL OF PHYSICAL SCIENCES**  
**NOVEMBER, 2022**

**SYNTHESIS AND CHARACTERIZATION OF LEAD-FREE  
PEROVSKITE FILMS FOR PHOTOVOLTAIC APPLICATIONS**

**By**

**Kamal Bhujel**

**Department of Physics**

**Supervisor**

**Prof. Suman Rai**

**Joint Supervisor**

**Dr. N. Surajkumar Singh**

**Submitted**

**In partial fulfillment of the requirement of the Degree of Doctor of  
Philosophy in Physics of Mizoram University, Aizawl.**

# **SYNTHESIS AND CHARACTERIZATION OF LEAD-FREE PEROVSKITE FILMS FOR PHOTOVOLTAIC APPLICATIONS**

## **THESIS ABSTRACT**

The motive of this work is to synthesize and characterize the lead-free perovskite for photovoltaic application. The demand for renewable sources of energy is very high. So, the alternative to conventional sources of energy is in the pathway of research. Si-based solar cells reached the highest limit, so more efficiency cannot be achieved further. The efficiency of Si-based solar cells is exceeded by the Pb-based Perovskite Solar cells. The toxicity of the Pb forbid the commercialization of Pb-based Solar Cells. Pb was replaced mainly by Sn and achieved a comparable high efficiency, but the stability of Sn created the problem. The Sn-based PSCs were very unstable. So, the stable, highly efficient and low-cost PSC is in demand.

The research is going into the many types of perovskite materials. Although all the pristine perovskite materials are not applicable in the photovoltaic application, their band gap is tuned by doping with other elements to be used in photovoltaic applications. Many reports have shown that band gap tailoring has also increased the efficiency of the PSCs. The efficiency of the PSCs is influenced by many factors like charge transportation, interface mismatch, the thickness of the layer, synthesis route, drying and annealing temperature, environmental conditions, HTL, ETL, precursor materials and more.

It is difficult to predict exactly at the initial stage of research the effects of the above factors on the efficiency of the PSC. All the factors act at the same time and the exact effect cannot be understood at the very first stage. For understanding the effects of various factors on the efficiency of the PSCs, different types of properties are studied under different conditions.

In this work, simple FTO/HTL/Perovskite/ETL/Ag architecture following the p-i-n structure of the PSC was employed. For ETL, ZnO np were used for all the devices. The HTL is different for all four devices. NiO thin film had been employed as HTL with 2, 4 and 6 molar % of Cu doping. The improvement in efficiency due to various HTL and ETL have been reported widely. Even the doping into the ETL and HTL materials has also influenced the efficiency. In this work also, the efficiency was affected by the Cu doping concentration into the NiO HTL. Doping of Cu into NiO influenced the carrier concentration resulting in a change in the efficiency of the PSCs.

In chapter 1, the introduction to the perovskite material, its historical advancement and its very fast improvement in PCE has been elaborated. The trend in the change of perovskite material from Pb, Sn to the inorganic double perovskite has been briefed.

In chapter 2, the details of the instruments used for characterization are given. The pictorial presentation helps to understand the components and working of the instrument. Although it is very vast to go into in-depth knowledge of each of the instrument and characterization techniques, the basics of all the techniques required for this work have been tried to accommodate in a very short.

In Chapter 3, the synthesis and characterization of ZnO np and ZnO nr are given. There are many routes for the synthesis of ZnO np. In this work, a solution-based method using TMAH has been used. ZnO nr are grown hydrothermally on the ZnO thin film. The use of ZnO np and ZnO nr have affected the efficiency of the PSCs when used as the ETL. The purpose of the synthesis of ZnO nr and ZnO np is to employ them into the PSC as ETL. The ZnO np was easily dispersed above the perovskite layer as ETL in p-i-n structure but the ZnO nr could not be grown above the perovskite layer due to which ZnO nr were not employed as ETL in our work. The optical, structural, morphological and electrical properties of the ZnO were studied in this chapter.

In Chapter 4, NiO Thin film was synthesized with 2, 4 and 6 molar % of Cu doping. The effect of doping on various properties has been studied by applying different characterization methods. The use of NiO as HTL has a positive influence on the efficiency of the PSC.

In Chapter 5, the synthesis of Pb-free double perovskite  $\text{Cs}_2\text{AgBiBr}_6$  was done. A confirmational report on its optical, morphological, and structural properties has been given in this chapter. The complete device fabrication with p-i-n structure with a different doping concentration of Cu into NiO as HTL and fixed ZnO as ETL has been studied. The overall PCE is also calculated in this chapter.

Chapter 6 summarizes all the findings conclusively with the extended works for the future.



The overall findings from this work are summarized below.

The sol-gel-spin-coating method is useful in the synthesis of ZnO np, ZnO nr and NiO and perovskite thin films. This method is low-cost and very facile but the exact thickness control is difficult.

The structural property was studied with GIXRD, for all the synthesized material. It confirmed the crystal structure of the ZnO, NiO and perovskite. The Cu doping into NiO has shifted the 2 theta peaks and had an effect on the crystal size also. With the increase in doping concentration, the size had increased to 4% but decreased with 6% doping.

The optical property was studied with UV-vis spectroscopy and PL spectroscopy. The absorbance and the transmittance were affected by the Cu doping into NiO. The effect on the increase in crystal size was observed in the red shift of the band gap. Transmittance was decreased with the Cu doping in NiO thin film and there was decrease in the band gap also. So, the doping of Cu into NiO can tune the band gap. The defect states were also studied with PL. The PL intensity decreased with the increase in Cu doping concentration which was due to the increment in the particle size.

The electrical properties were studied under different illumination for ZnO and NiO-based thin films and a solar simulator was used for the study of Current-voltage characteristics for PCE calculation of the prepared device. The sample was kept under dark, UV, Visible and IR lamps. The highest doping concentration under IR showed the maximum I-V behaviour. So, Cu doping has a good effect on electrical conductivity. The Hall measurement also showed an increase in carrier concentration with the increase in doping concentration.

The FESEM images were studied to understand the surface morphology of the prepared thin films. Using ImageJ software, the particle sizes were also calculated which can be compared with the crystal size calculated from the XRD. Most of all the films had smooth and uniform film. Although it is difficult to obtain high quality films from the spin coating device, the film was optimum.

The XPS and EDX graphs were mainly used for the confirmation of the elemental composition of the prepared thin films. A little study from the XPS graph is done for the Cu doping into the NiO thin films and confirmed the Cu doping as well.

In the end, the completed device was characterized with I-V measurement and found increased PCE with the increase in Cu doping concentration. So, the highest efficiency of 1.24 % was observed with the 6Cu:NiO device.

This work only shows the possibility of device fabrication with the materials used. Now further improvement to increase the PCE of the Pb-free PSC can be extended in future works by the following methods.

Different parameters can be changed, the synthesis methods can be improved, the effect of doping on ETL also can be studied the HTL and ETL materials can also be replaced, and the band gap of the Perovskite can be tuned by doping.